NASA TECHNICAL NOTE

N73-18000

NASA TN D-7108

NASA TN D-7108

CASE FILE COPY

HEATING AND FLOW-FIELD STUDIES ON A STRAIGHT-WING HYPERSONIC REENTRY VEHICLE AT ANGLES OF ATTACK FROM 20° TO 80° WITH SIMULATION OF REAL-GAS TRENDS

by James L. Hunt and Robert A. Jones

Langley Research Center
Hampton, Va. 23365

NATIONAL AERONAUTICS AND SPACE ADMINISTRATION • WASHINGTON, D. C. • MARCH 1973

1. Report No. NASA TN D-7108	2. Government Accession No.	3. Recipient's Catalog No.

4. Title and Subtitle

HEATING AND FLOW-FIELD STUDIES ON A STRAIGHT-WING HYPERSONIC REENTRY VEHICLE AT ANGLES OF ATTACK FROM 20° TO 80° WITH SIMULATION OF REAL-GAS TRENDS

5. Report Date

March 1973

6. Performing Organization Code

7. Author(s)

James L. Hunt and Robert A. Jones

8. Performing Organization Report No.

L-7946

9. Performing Organization Name and Address

NASA Langley Research Center
Hampton, Va. 23365

10. Work Unit No.

117-07-01-05

11. Contract or Grant No.

12. Sponsoring Agency Name and Address

National Aeronautics and Space Administration
Washington, D.C. 20546

13. Type of Report and Period Covered

Technical Note

14. Sponsoring Agency Code

15. Supplementary Notes

16. Abstract

Data are presented from a series of phase-change heat-transfer and flow-visualization tests at Mach 7.4, 8, and 10.3 in air, Mach 19.5 in nitrogen, Mach 20.3 in helium, and Mach 6 in tetrafluoromethane (CF_4) on the windward surface of a straight-wing hypersonic reentry configuration for angles of attack from 20° to 80°. The results indicate that

(1) For hypersonic stream Mach numbers, the flow field over the straight-wing configuration is essentially independent of Mach number.

(2) The transition Reynolds number decreases with increasing angle of attack for $40^\circ \leqq \alpha \leqq 60^\circ$.

(3) At some "critical" angle of attack, the wing-shock standoff distance is greatly increased and the stagnation line moves downstream from the wing leading edge.

(4) The value of the "critical" angle of attack is very sensitive to the flow shock density ratio or effective gamma.

(5) At angles of attack above the "critical" value for all gases, the nondimensional level of heat transfer to the wing is higher for the higher shock-density-ratio flows.

17. Key Words (Suggested by Author(s)) Orbiter Straight wing Reentry vehicle Heating Flow field Real gas	18. Distribution Statement Unclassified – Unlimited

19. Security Classif. (of this report) Unclassified	20. Security Classif. (of this page) Unclassified	21. No. of Pages 94	22. Price* $3.00

*For sale by the National Technical Information Service, Springfield, Virginia 22151

HEATING AND FLOW-FIELD STUDIES ON A STRAIGHT-WING HYPERSONIC REENTRY VEHICLE AT ANGLES OF ATTACK FROM 20° TO 80° WITH SIMULATION OF REAL-GAS TRENDS

By James L. Hunt and Robert A. Jones
Langley Research Center

SUMMARY

The phase-change-coating technique was used to study the heating to the lower surfaces of the 0.0047-scale and 0.0093-scale truncated models of a straight-wing hypersonic reentry configuration. Tests were conducted at Mach 8 in air for free-stream Reynolds numbers based on model lengths of 0.81×10^6 to 6.28×10^6 at 20° angle of attack, 1.99×10^6 at 40°, 4.33×10^6 at 50°, and 2.1×10^6 and 2.9×10^6 at 60°. Tests were made at Mach 10.3 in air on the 0.0093-scale model for a Reynolds number of 1.80×10^6 and angles of attack of 20°, 40°, 60°, and 80°. Very high rates of heat transfer to the wing leading edge occurred for 20° and 40° angles of attack as well as a large area of increased heating due to impingement of the transmitted body shock on the wing. At 60° angle of attack the shock interference effects were weakened considerably, and at 80° angle of attack they disappeared completely. The disappearance of the shock interference effects was due to the merging of the fuselage shock and wing shock into essentially one shock envelope.

Maximum peak radiation equilibrium skin temperatures for a 45.72-m vehicle entering the atmosphere along a constant angle-of-attack trajectory were estimated to be 2481 K, 1965 K, 1746 K, and 1384 K for angles of attack of 20°, 40°, 60°, and 80°, respectively. These maximum values occurred only on the wing for angles of attack less than 80°; however, at 80° the maximum temperatures of the wing and body were equal.

Comparison of the heat-transfer distributions along the body center line of the truncated straight-wing orbiter for different Reynolds numbers revealed that the onset of transition from laminar to turbulent flow did not occur at a local Reynolds number (based on oblique-shock entropy) of 680 000 for 40° angle of attack but did occur at a local Reynolds number of 200 000 for 60° angle of attack; this indicates that the transition Reynolds number is decreasing with an increase in angle of attack in this angle-of-attack range. Also, at 60° angle of attack, the transition position on the fuselage was essentially stationary with increasing Reynolds number.

Flow-visualization, oil-flow, and phase-change heat-transfer data were obtained for the 0.0047-scale model of the truncated straight-wing orbiter at angles of attack of 40°, 52°, and 60° at a free-stream Mach number of approximately 20 in helium $\left(\rho_2/\rho_1 \approx 4.0\right)$ and nitrogen $\left(\rho_2/\rho_1 \approx 5.9\right)$ and at a Mach number of approximately 8 in air $\left(\rho_2/\rho_1 \approx 5.7\right)$; thus, both density ratio ρ_2/ρ_1 and Mach number were isolated as variables. Also, shock shapes obtained at a Mach number of 6 in tetrafluoromethane $\left(\rho_2/\rho_1 \approx 12\right)$ are compared herein. No significant Mach number effects were observed for either the heat-transfer distributions or the viscous streamlines; however, shock-density-ratio effects significantly influenced both of these parameters especially at angles of attack above 40°.

INTRODUCTION

One of the proposed configurations for a space-shuttle orbiter was a straight-wing vehicle suggested by the NASA Manned Spacecraft Center (ref. 1). This configuration is representative of a class of hypersonic reentry vehicles which enter at a high angle of attack $(40^\circ \leqq \alpha \leqq 80^\circ)$ to minimize entry heating and radiation equilibrium skin temperatures. At these high angles of attack which persist during the entire heat pulse, the windward surfaces receive by far the largest aerodynamic heating. The preliminary heat-transfer data discussed in reference 1 indicate a need for much more detailed measurements of heat transfer, particularly for the lower wing surfaces which may encounter wing-fuselage shock interference effects. Since very little transition data exist on slender bodies at high angles of attack, the question remains as to whether or not transition from a laminar to a turbulent boundary layer would be experienced throughout the period of peak laminar heating. The present heat-transfer data along the windward center line indicating transition from a laminar to a turbulent boundary layer are presented herein for $40^\circ \leqq \alpha \leqq 60^\circ$.

Further aggravating the heating problem in flight are real-gas effects. Large density ratios across the shock result from chemical dissociation of the molecules in the high-temperature gas behind the shock. The normal-shock density ratio at peak heating is approximately 18 on the Manned Spacecraft Center (MSC) straight-wing-orbiter trajectory for an angle of attack of 60°. Since, in the earth's atmosphere, a density ratio greater than 6 indicated molecular dissociation, the potential for real-gas effects along such a trajectory is large. For hypersonic flow conditions, aerodynamic characteristics of bodies at high angles of attack are determined primarily by the inviscid flow field which in turn is most influenced by the shock density ratio (an indicator of the amount of real-gas effects present, ref. 2). The inviscid flow controls the location and strength of the fuselage/wing shock intersection and thus will affect the location and magnitude of the resultant interference heating.

For ground tests at hypersonic Mach numbers where no dissociation occurs, the density ratio across a shock is determined by the specific-heat ratio γ of the gas; thus, ground test data obtained at hypersonic Mach numbers at various values of γ can be used to simulate the trends of equilibrium real-gas effects expected in flight (ref. 3). The shock shape, the surface oil-flow patterns, the location of the fuselage-shock/wing-shock interaction, and the distribution of the resulting interference-heating patterns were obtained on a truncated straight-wing orbiter in several facilities at $\gamma = 1.67$ and 1.4 (normal-shock density ratios of 4.0 and 5.6 to 5.9). Also, shock shapes at $\gamma = 1.12$ $(\rho_2/\rho_1 \approx 12)$ are compared herein as in reference 3. Effects of the density ratio on the wing flow field, fuselage/wing shock interference heating, and the level of heating on the wing at 60° angle of attack are shown.

Heat-transfer data were obtained on the straight-wing configuration with tail and wing tips shortened to allow testing of a larger scale model in the Langley Mach 8 variable-density hypersonic tunnel $(\rho_2/\rho_1 \approx 5.6)$ and in the Langley continuous-flow hypersonic tunnel at Mach 10.3 $(\rho_2/\rho_1 \approx 5.7)$. The phase-change-coating heat-transfer technique (ref. 4) was used in both sets of tests. For these tests, Reynolds numbers based on body length varied from 0.8×10^6 to 6.3×10^6 from $\alpha = 20^\circ$ to 80°. Flow-visualization tion and phase-change heat-transfer data were also obtained on the truncated straight-wing orbiter in helium $(\rho_2/\rho_1 \approx 4.0)$ and nitrogen $(\rho_2/\rho_1 \approx 5.9)$ for a Mach number of 20 and in air $(\rho_2/\rho_1 \approx 5.6)$ for a Mach number of 8; thus, the effects of density ratio and Mach number were isolated and studied independently.

SYMBOLS

c	specific heat
D	depth of fuselage in vicinity of wing (fig. 21(b))
h	heat-transfer coefficient
h_{ref}	reference heat-transfer-coefficient stagnation-point value for a 0.3048-m-radius sphere scaled to same scale factor as test model
k	thermal conductivity
l	length of complete configuration (20.95 cm and 41.90 cm for 0.0047-scale and 0.0093-scale models, respectively)

l'	axial distance from nose to juncture of fuselage and leading edge of wing
M	Mach number
N_{Pr}	Prandtl number
N_{St}	Stanton number, $\frac{h}{\rho_e u_e (c_p)_g}$
p	pressure
$\dot{Q}$	heat-transfer rate, $\dot{Q}_{max}(h/h_{ref})$ assuming $h/h_{ref} = \dot{Q}/\dot{Q}_{ref}$
$\dot{Q}_{max}$	maximum heat-transfer rate to a 0.3048-m-radius sphere for a constant angle-of-attack flight trajectory
$\dot{Q}_{ref}$	reference heat-transfer-rate stagnation-point value for a 0.3048-m-radius sphere scaled to same scale factor as test model
r	radius of reference sphere
$R_{e,s}$	local Reynolds number based on properties at the edge of the boundary layer and length from leading edge
R_∞/m	unit Reynolds number
$R_{\infty,l}$	Reynolds number based on free-stream conditions and scaled length of complete configuration
s	surface length along fuselage center line measured from Newtonian stagnation point
t	time
t_d	thermal interference diffusion time, $0.2(\tau)^2/\lambda$
T	temperature
$\bar{T}$	temperature parameter (eq. (2))

u	velocity
x	axial coordinate of model measured from nose
x'	chordwise coordinate (measured normal to leading edge, fig. 2(b))
y	horizontal coordinate measured normal to and from axial coordinate (fig. 5)
z	coordinate normal to plane formed by leading edge and chordwise coordinate (fig. 2(b))
α	angle of attack
β	heat-transfer parameter (see eq. (2))
γ	ratio of specific heats and/or isentropic exponent
Δ	shock standoff distance
Δ_{max}	maximum shock standoff distance
ϵ	emissivity
κ	Boltzmann constant
λ	thermal diffusivity, $k/\rho c$
μ	viscosity
ρ	density
τ	depth of heat penetration (eq. (3))

Subscripts:

aw	adiabatic wall conditions
e	edge of boundary layer
g	test gas

i	initial conditions
m	model
NS	normal-shock entropy
OS	oblique-shock entropy
p	constant pressure
pc	phase-change coating
s	stagnation condition behind normal shock
t	total condition of free stream
tr	condition at beginning of boundary-layer transition
w	wall
1	free-stream static conditions
2	static conditions behind normal shock

TEST FACILITIES

Data were obtained from tests conducted in five Langley wind tunnels. The pertinent test conditions and references are given in the following table:

Langley facility	Reference	Gas	M_1	γ	ρ_2/ρ_1	T_w/T_t	R_∞/m	Scale of model tested
Mach 8 variable-density hypersonic tunnel	5	Air	7.8 to 8	1.4	5.57	0.5	3.9×10^6	0.0047 and 0.0093
Continuous-flow hypersonic tunnel	6	Air	10.3	1.4	5.73	.4	4.3	.0093
Hypersonic nitrogen tunnel	7	N_2	19.5	1.4	5.92	.3	2.2	.0047
22-inch helium tunnel	8	He	20.3	1.67	3.97	.7	9.1	.0047
Pilot model hypersonic CF_4 blowdown tunnel	2	CF_4	6	1.12	12.0	.4	1.1	0.0011 and 0.0022

MODELS

To obtain the most accurate and detailed heat-transfer measurements, it is desirable to test as large a scale model as possible. The models (0.0047 and 0.0093 scale) were larger than those ordinarily possible to test at high angles of attack in the facilities used for this investigation; therefore, the models were truncated by cutting off the tail section and a portion of the wing tip. A sketch showing the complete 0.0047-scale configuration and the actual truncated model is presented in figure 1. The wing of the 0.0093-scale model was truncated more inboard (except for $\alpha = 20^{\circ}$ at Mach 8) than the wing of the 0.0047-scale model as shown in this figure. Figure 2 gives the details of the fuselage and wing and figure 3 shows the sting arrangement used. Both models (0.0047 and 0.0093 scale) were cast from an epoxy resin with a silica filler. The 0.0047-scale model was cast in one piece. The fuselage and wing were cast separately for the 0.0093-scale model and mated as shown in the photograph of figure 4. The models were intended to be identical except for the scale. However, the fuselage of the 0.0047-scale model was found to be slightly less blunt than that of the 0.0093-scale version (fig. 5).

Additional material was added to the lee side of the wing for both scale models as shown in figure 2(b). This material provided more strength and additional thickness in order to keep the heat penetration depth small compared with the wing thickness. This is essential to the accuracy of the phase-change-coating heat-transfer technique.

The square root of the product of the thermophysical properties $\sqrt{\rho_m c_m k_m}$ of these models is also essential to the heat-transfer technique utilized. The values of this parameter are 1.66×10^3 and 1.41×10^3 J/m^2-K-sec$^{1/2}$ for the 0.0047-scale model and the 0.0093-scale model, respectively.

The shock shape was obtained on both a complete (fig. 1) and a truncated straight-wing orbiter configuration (fig. 1, Note B) in the pilot model hypersonic CF_4 blowdown tunnel. The complete model was cast from aluminum and the truncated one from an epoxy resin (Stycast); their scales were 0.0011 and 0.0022, respectively.

TEST TECHNIQUES AND DATA REDUCTION

Heat Transfer

Heat-transfer data were obtained by using the phase-change-coating technique described in reference 4. With this technique the heat-transfer coefficients are determined by measuring the time required for a point on the surface of the model to reach the phase-change temperature of the thin fusible coating. These values of time and temperature are then used with the solution to the transient one-dimensional heat-conduction equation with a step input in h to ascertain the heat-transfer coefficients.

Motion-picture photography was used to record the phase-change patterns on the models along with the time at which they occurred. Sample photographs of phase-change patterns on the truncated straight-wing orbiter taken in three of the four Langley facilities from which heat-transfer data were obtained are presented in figures 6 to 11. The light areas are the unmelted coating, whereas the dark areas are higher heating rate areas in which the phase change has already occurred. The line separating these areas is a line of known temperature and represents a constant value of heat-transfer coefficient provided the adiabatic wall temperature is constant. Also, the time at which the phase change occurred is restricted to certain limits (to be discussed later).

A general form of the solution of the transient one-dimensional heat-conduction equation may be written as

$$h = \frac{\beta\sqrt{\rho_m c_m k_m}}{\sqrt{t_{pc}}} \tag{1}$$

where h is the heat-transfer coefficient, $\rho_m c_m k_m$ is the product of the thermophysical properties of the model material, t_{pc} is the time required for the phase change to occur and is measured from the time the model is first exposed to the flow, and β depends on the temperature parameter as follows:

$$\overline{T} = \frac{T_{pc} - T_i}{T_{aw} - T_i} = 1 - e^{\beta^2} \operatorname{erfc} \beta \tag{2}$$

The functional dependence of β on $\overline{T}$ comes from the solution of the transient one-dimensional heat-conduction equation and is given in reference 4.

Errors due to violation of semi-infinite slab assumption.- The results obtained with this one-dimensional assumption are approximations to the solution for the actual body geometry provided the depth of heat penetration is small compared with governing model dimensions. The depth of heat penetration for the semi-infinite slab is approximated in reference 4 as

$$\tau = \sqrt{\frac{\lambda_m t_d}{0.2}} \tag{3}$$

This equation can be used to estimate the minimum thickness of model material required or the minimum distance away from an abrupt change in heating rate or the minimum distance away from a model protuberance or other change in geometry for which the one-dimensional semi-infinite slab solution is valid. For a particular model geometry, equation (3) can also be used to determine the maximum allowable test time for which the solution is valid. The accuracy of the one-dimensional semi-infinite slab solution for test times longer than those given by equation (3) is unknown; therefore, one should keep test times below this maximum by selecting coatings with the proper phase-change temperature.

Errors due to initial exposure.- In addition to the limitation of the maximum allowable test time, there is also a limitation on the minimum allowable test time. This limitation means that the time from initial exposure of the model to the flow until the phase change occurs must be long relative to both the accuracy with which the initial time can be determined and the time required for the model to pass through the separated tunnel-wall boundary layer where erroneous heating rates are experienced. A minimum allowable test time of 1 sec has been determined to be sufficiently long to make any errors from these sources negligible for the Langley Mach 8 variable-density hypersonic tunnel.

Negligible error boundary.- The variation of the maximum and minimum allowable test time with distance along the chord of the wing at a position of about one-half of the exposed semispan is shown in figure 12 for both models. The minimum allowable test time for negligible error remains constant at 1 sec, whereas the maximum allowable test time which is a function of the local thickness varies with position. These trends were determined by using one-half of the thickness of the wing section for τ in equation (3) because heat is entering at both surfaces and because of the embedded fiber-glass wing support whose thermophysical properties differ from the remainder of the wing. At the stagnation line of the leading edge, there is no test time for which the error would be negligible; however, data for the lower Reynolds number at Mach 8 and $\alpha = 20^{\circ}$ were utilized for the wing leading edge for times as short as 0.7 sec and as long as 1.2 sec. The data for the wing leading edge are therefore subject to error. The error is such that the indicated heat-transfer coefficient is larger than that which actually occurs.

With the exception of the wing leading edge just discussed, all the phase-change patterns which occurred at test times outside the allowable limits were disregarded in the data reduction process. In order to obtain heat-transfer data over the entire lower surface of the body and wing and stay within the allowable test times, repeat tests at the same tunnel conditions were made by using coatings having different phase-change temperatures.

Errors due to uncertainty in adiabatic wall temperature.- At high values of the wall-to-total temperature ratio T_w/T_t, the accuracy of the heat-transfer coefficient obtained with the phase-change-coating technique becomes increasingly sensitive to the accuracy with which the adiabatic wall temperature is known. The sensitivity of the indicated heat-transfer coefficient to the adiabatic wall temperature is illustrated in figure 13 for

$T_w/T_t = 0.78$, 0.55, and 0.28 and for values of β which are representative of those used in obtaining the data presented herein.

In converting the phase-change isotherms to nominal heat-transfer coefficients in both the air (Mach 8 and 10.3) and nitrogen (Mach 19.5) data, the adiabatic wall temperature was assumed equal to the total temperature of the stream over the entire windward surface of the model. The adiabatic wall temperature obtained by using a laminar recovery factor $\left(\sqrt{N_{Pr}}\right)$ and expanding isentropically from the total pressure behind a normal shock to the local Newtonian pressure gives at most a 9-percent difference (fig. 13) in the heat-transfer coefficients obtained in air at Mach 8 for $T_w/T_t = 0.55$ at 40° angle of attack compared with that of 6 percent obtained by using an adiabatic wall temperature equal to the total temperature at $\alpha = 60^\circ$. Similarly, for the coefficients obtained in nitrogen $\left(\text{Mach } 19.5,\ T_w/T_t = 0.28\right)$ the difference is at most 5 percent at $\alpha = 40^\circ$ and 3 percent at $\alpha = 60^\circ$.

Since the helium data were obtained at a relatively high value of T_w/T_t and are more sensitive to the accuracy of the value of the adiabatic wall temperature which was used in the data reduction process (fig. 13), the adiabatic wall temperature was not assumed equal to the total temperature. For both $\alpha = 40^\circ$ and 60°, the model was submitted to the test stream coated with a phase-change paint having a melt temperature only 16.66 K below the total temperature of the test media. At both angles of attack, the paint eventually melted over the entire windward surface; this insured that the adiabatic-wall-to-total temperature ratio was above 0.96. Assuming that the distribution of this ratio with the angle between a vector normal to the model surface and the free-stream velocity is similar to that on a hemisphere in air (obtained by using a laminar recovery factor and expanding isentropically from the total pressure behind the normal shock to the local Newtonian pressure), the adiabatic-wall-to-total temperature ratio was varied from 1.0 to 0.97 at 40° angle of attack and from 1.0 to 0.98 at 60° angle of attack. These values were assigned to the isotherms along the fuselage center line and the 15-percent exposed semispan of the wing. By using this method, the adiabatic wall temperature is thought to be in error by at most 2 percent or -1.5 percent which according to figure 13 holds the error due to uncertainty in T_{aw} in the heat-transfer coefficient within a ±7.5 percent bracket for the helium data.

Flow Visualization

Oil-flow (ref. 9), schlieren (ref. 10), shadowgraph (ref. 10), and electron-beam (ref. 11) flow-visualization techniques were used to obtain insight as to the structure of the flow field both on and about the straight-wing reentry vehicle.

Reference Heat-Transfer Coefficient and Skin Temperature

The data are presented as the heat-transfer-coefficient ratio h/h_{ref}, where h is the experimental local value and h_{ref} is the theoretical value for the stagnation point of a 0.3048-m-radius sphere scaled by the same scale factors (0.0047 and 0.0093) as the model. The value at the reference heat-transfer coefficient h_{ref} was calculated as follows (ref. 12):

$$h_{ref} = 0.76\left(c_p\right)_g\left(N_{Pr,w}\right)^{-0.6}\left(\rho_w\mu_w\right)^{0.1}\left(\rho_s\mu_s\right)^{0.4}(du/ds)^{0.5} \tag{4}$$

where du/ds taken from Newtonian theory (ref. 12) is given by

$$\frac{du}{ds} = \frac{1}{r}\left[\frac{2p_s}{\rho_s}\left(1 - \frac{p_1}{p_s}\right)\right]^{1/2} \tag{5}$$

The maximum value of the radiation equilibrium skin temperature was computed in the following manner. First, the stagnation-point heat-transfer rate to a 0.3048-m-radius sphere assumed to be flying along the trajectory of the actual configuration was determined. Second, the value of $\dot{Q}_{max}$ was found for entry at each angle of attack. This maximum 0.3048-m-radius-sphere value was then multiplied by the experimental value of h/h_{ref} assuming $\left(h/h_{ref} = \dot{Q}/\dot{Q}_{ref}\right)$ to give the maximum heating rate for each of the lines of constant h/h_{ref}. Then, the maximum radiation equilibrium skin temperature was computed by assuming that all the aerodynamic heat input was radiated at an emissivity of 0.8 (ref. 13), that is,

$$T_w = \left(\frac{\dot{Q}}{\epsilon\kappa}\right)^{1/4} \tag{6}$$

The variation of the maximum reference heating rate with angle of attack is shown in figure 14. This reference heating rate is a minimum for the design angle of attack for entry which is 60°.

PRESENTATION OF RESULTS

Because of the large amount of information of different types obtained in different facilities, this section simply presents the basic data. Apparent discrepancies in the data are explained. Brief statements indicating the dominant flow phenomena influencing the data, the emerging trends, and in some instances the purpose of a particular presentation are included. These brief statements are amplified in the discussion of the results.

Flow Field

Knowledge of the flow field is pertinent in interpreting heat-transfer results especially when shock/shock intersection and/or shock/boundary-layer interaction is present. Also, the possibility that the truncated wing model (fig. 1) used in these tests may give different results from those of the complete configuration must be considered.

Excellent oil-flow patterns obtained at Ames Research Center by H. Lee Seegmiller at Mach 7.4 on a complete straight-wing orbiter are presented in figures 15 to 18. Strong interference effects from the bow/wing shock interaction are apparent from the oil-flow patterns of figure 15. The configuration on which these oil-flow patterns were obtained is slightly different from the configuration (figs. 1 to 4) tested in this investigation. The full-scale wing span, the length l, and the axial distance from nose to junction of fuselage and leading edge of wing l' for Seegmiller's model are 30.78 m, 43.58 m, and 31.08 m, respectively; whereas these full-scale dimensions on the model of figures 1 to 4 are 32.50 m, 42.25 m, and 31.70 m, respectively. Also, there is a small difference in fuselage bluntness (fig. 5) with Seegmiller's model (ref. 14) being the blunter of the two configurations.

Oil-flow patterns obtained on a complete wing at Mach 7.4 $\left(\rho_2/\rho_1 \approx 5.5\right)$ in air by H. Lee Seegmiller, on a wing of the truncated model at Mach 8 $\left(\rho_2/\rho_1 \approx 5.7\right)$ in air, and on the same truncated model at Mach 20 $\left(\rho/\rho_1 \approx 5.9\right)$ in nitrogen are presented in figure 16 for $\alpha = 60^{\circ}$. The oil-flow patterns on the complete and truncated wings are very similar. At this angle of attack, the stagnation line is downstream of the leading edge of the wing and the weak shock interference effects appear as a small distortion of the wing stagnation line near the 35-percent exposed span position.

Oil-flow patterns on the complete straight-wing configuration are presented in figure 17 for $\alpha = 60^{\circ}$ and 80°. The patterns on the wing surface no longer show the strong V-shape shock-interaction interference effect which appears at the lower angles of attack (fig. 15).

The oil-flow pattern on the windward surface of the complete straight-wing configuration at 80° angle of attack is shown in figure 18. This pattern shows several stagnation-point-type flows along the fuselage center line forward of the wing.

The manner in which the truncated-straight-wing-orbiter flow field changes with increasing angle of attack is shown in the electron-beam (ref. 11) photographs (taken normal to wing span) of figure 19 and schlieren photographs (profile view) of figure 20. The electron-beam photographs were taken in the Langley 22-inch helium tunnel

$(\rho_2/\rho_1 \approx 4.0)$ and the schlieren profiles were obtained in the Langley Mach 8 variable-density hypersonic tunnel $(\rho_2/\rho_1 \approx 5.6)$.

An example of the influence of the density ratio on the inviscid flow field of the truncated MSC straight-wing orbiter at $\alpha = 60^\circ$ is shown in the schlieren and shadowgraph photographs of figure 21(a) for a free-stream Mach number of 8 in air and 6 in CF_4 with density ratios of 5.6 and 12.1, respectively. The shock profiles on a complete straight-wing configuration at 60° angle of attack are given in figure 21(b) for $M_1 = 19.5$ in nitrogen $(\rho_2/\rho_1 \approx 5.9)$ and $M_1 \approx 6$ in CF_4 $(\rho_2/\rho_1 \approx 12.1)$. Oil-flow patterns obtained in helium $(\rho_2/\rho_1 \approx 4.0)$ and nitrogen $(\rho_2/\rho_1 \approx 5.9)$ at $M_1 \approx 20$ for angles of attack of 40° and 52° are given in figures 22 and 23, respectively. Note the much more rearward movement of the stagnation point on the fuselage and the stagnation line on the wing in going from $\alpha = 40^\circ$ to $\alpha = 52^\circ$ in helium than in nitrogen.

Heat-Transfer-Coefficient and Skin-Temperature Distributions

The heat-transfer data are presented in terms of nondimensional heat-transfer-coefficient contours with the corresponding skin temperatures listed. Center-line coefficient distributions are also included. These data are categorized according to angle of attack.

$\underline{\alpha = 20^\circ}$.- Contours of h/h_{ref} at $\alpha = 20^\circ$ are shown in figure 24 for $M_1 \approx 8$ in air and values of $R_{\infty,l}$ from 0.81×10^6 to 6.28×10^6 and in figure 25 for $M_1 = 10.3$ in air and $R_{\infty,l} = 1.80 \times 10^6$. Fuselage/wing shock interaction and wing-body corner interference both caused increased heating over a considerable portion of the wing.

The h/h_{ref} data along the fuselage center line of the model from figures 24 and 25 are plotted as a function of s/l in figure 26.

$\underline{\alpha = 40^\circ}$.- The heat-transfer-coefficient contours with corresponding skin temperatures on the truncated straight-wing orbiter at $\alpha = 40^\circ$ are given in figure 27 for $M_1 \approx 8$ in air and $R_{\infty,l} = 1.99 \times 10^6$ and in figure 28 for $M_1 = 10.3$ in air and $R_{\infty,l} = 1.80 \times 10^6$. Again, as at $\alpha = 20^\circ$, fuselage/wing shock interaction and wing-body corner interference both caused increased heating over a considerable portion of the wing.

The heat-transfer-coefficient distributions along the windward center line from figures 27 and 28 are plotted in figure 29. The two distributions obtained in the present study are practically the same except for the spike in the Mach 10.3 data at $s/l = 0.47$. This deviation is due in part to a small rise (ramp-like protrusion) in the windward surface profile where the wing attaches to the fuselage on the 0.0093-scale model. Also, the attachment of the wing to the fuselage left a slight discontinuity (seam line) in the windward surface. The 0.0047-scale model was made in one piece and therefore did not have a seam line at the wing-body juncture which may explain the absence of a spike in the heating distribution for this model.

The Reynolds numbers were not sufficient in either test (Mach 8 or 10.3) to cause transition from a laminar to a turbulent boundary layer. However, tests conducted at Ames Research Center on a straight-wing-orbiter fuselage without wings (ref. 15) at Mach 7.4 produced transition at $\alpha = 40^\circ$ for $R_{\infty,l} = 9.6 \times 10^6$. These data are included in figure 29.

Phase-change heat-transfer tests were made in air on a complete straight-wing-orbiter model (with slightly blunter nose); the results indicate a significant Reynolds number influence on the fuselage/wing shock interference heating distribution (fig. 30).

Heat-transfer-coefficient contours obtained in helium and nitrogen at $M_1 \approx 20$ and in air at $M_1 \approx 8$ $\left(\rho_2/\rho_1 \approx 4.0, 5.9, \text{and } 5.6, \text{respectively}\right)$ are presented in figure 31.

$\underline{\alpha = 50^\circ}$.- The heat-transfer-coefficient contours on the truncated straight-wing orbiter at an angle of attack of 50° are given in figure 32 for a Mach number of 8 in air and $R_{\infty,l} = 4.33 \times 10^6$. The maximum heat-transfer coefficients on the wing and wing leading edge were not obtained because the paint melted on these surfaces under the influence of the tunnel wall boundary layer through which the model was injected. However, the important point to note is that shock-interaction-type interference does occur over the wing surface at this angle of attack.

The heat-transfer-coefficient distribution at 50° angle of attack along the windward center line is given in figure 33. Transition from a laminar to a turbulent boundary layer (indicated by the beginning of a rise in the heat-transfer distribution) occurs at $0.5 < s/l < 0.55$.

The heat-transfer-coefficient contours on the truncated straight-wing orbiter for a Mach number of 20.3 in helium $\left(\rho_2/\rho_1 \approx 4.0\right)$ and $R_{\infty,l} = 1.93 \times 10^6$ are given in figure 34. In contrast to the Mach 8 tests in air $\left(\rho_2/\rho_1 \approx 5.6\right)$, the strong shock/boundary-layer interaction (V-shape interference) over the wing surface no longer appears.

$\underline{\alpha = 60^\circ}$.- Heat-transfer-coefficient contours on the windward surface of the orbiter at an angle of attack of 60° are given in figure 35 for $M_1 \approx 8$ and $R_{\infty,l} = 2.1 \times 10^6$ and 2.9×10^6. The contours are given in figure 36 for a Mach number of 10.3 and a Reynolds number of 1.80×10^6. The contours on the wing surface no longer show the strong V-shape shock/boundary-layer interaction which appeared at lower angles of attack.

The heat-transfer-coefficient distributions along the windward center line from figures 35 and 36 are plotted in figure 37. The distributions $\left(M_1 \approx 8 \text{ and } M_1 = 10.3\right)$ are essentially the same except for the transition indications (upward trend of data with increasing s/l). Again, as at $\alpha = 40^\circ$, tests conducted at Ames Research Center (ref. 15) at Mach 7.4 on a thermocouple model of the straight-wing-orbiter fuselage without wings produced transition at $\alpha = 60^\circ$ for $R_{\infty,l} = 9.6 \times 10^6$.

Heat-transfer-coefficient contours (Mach 8, air) on and in the vicinity of the wing leading edge are shown in figure 38. The weak shock-interaction interference effects just slightly downstream of the leading edge are evident. Even more evident in both intensity and extent is the wing-root interference heating.

Heat-transfer-coefficient contours obtained on the truncated straight-wing orbiter in density-ratio flows of 4.0 and 5.9 at $M_1 \approx 20$ in helium and nitrogen and 5.6 at $M_1 \approx 8$ in air for 60° angle of attack are presented in figure 39. Again, none of these contours show the large V-shape patterns which resulted from bow/wing shock interference effects at lower angles of attack. At $\alpha = 60^\circ$, the density ratio had a significant effect on the level of heating over the entire wing surface with a lower level of heating at the lower density ratio.

$\underline{\alpha = 80^\circ}$.- Heat-transfer-coefficient contours for an angle of attack of 80° at $M_1 = 10.3$ and $R_{\infty,l} = 1.80 \times 10^6$ are given in figure 40. No effect of shock interference heating on the wing appears in these contours. The heat-transfer-coefficient distribution along the center line is given in figure 41. This rather erratic distribution, evident from the circular-shape contours on the body (fig. 40), probably resulted from multiple stagnation points along the fuselage.

Side.- The phase-change isotherm patterns obtained on the side of the model are shown in figure 42 for $\alpha = 20^\circ, 40^\circ, 60^\circ$, and 80° at $M_1 = 10.3$. In order to simplify the comparison, only the maximum equilibrium values of skin temperature are shown. At the lower angles of attack, the interference in the vicinity of the wing may be influenced by the thickened top of the wing (fig. 2(b)); however, at angles of attack of 40° or more the effect of the thickened wing should be negligible.

DISCUSSION OF RESULTS

In this discussion, an attempt is made to isolate the effects of the pertinent variables. The influence of the free-stream variables (Mach number and Reynolds number) is discussed first, followed by the effects of variations in test angle of attack and shock density ratio. The effects of flow interaction on the wing which are peculiar to the test configuration are then pointed out, and the discussion is terminated with a summary of the maximum heating and corresponding skin temperatures encountered.

Free-Stream Mach Number Effects

The shock standoff distance distributions along the center line of the fuselage on the truncated straight-wing orbiter in air at Mach 8 and on the complete straight-wing orbiter in nitrogen at Mach 19.5 and in CF_4 at Mach 6 are given in figure 43 for 60° angle of attack. Since the shock density ratio is essentially the same for the Mach 8 and Mach 19.5 data, these two distributions show only Mach number effects. The shock standoff distances were taken from the schlierens and electron beam photographs of figures 20 and 21. These two distributions are almost the same as far aft as the wing-body juncture where the center-line standoff distance on the truncated model moves slightly inside that on the complete model at Mach 19.5. This result indicates that the Mach number effects on fuselage shock shape are essentially negligible from Mach 8 to Mach 19.5. Also, truncating the model at this high angle of attack ($\alpha = 60^\circ$) allows a slight inboard movement of the fuselage shock.

A comparison of the Mach 8 and 10.3 heat-transfer-coefficient contours (figs. 24, 25, 27, 35, and 36) and the fuselage center-line distributions (figs. 26, 29, and 37) for 20° to 60° angle of attack indicates no significant Mach number effects on the heat-transfer distribution of the straight-wing orbiter. A similar comparison of the contours obtained in nitrogen at Mach 19.5 and in air at Mach 8 at about the same density ratio for $\alpha = 40^\circ$ and 60° (figs. 31 and 39) gives credence to this observation.

Reynolds Number Effects (Transition)

The heat-transfer-coefficient distributions along the fuselage at $\alpha = 40^\circ$, 50°, and 60° (figs. 29, 33, and 37) and the contours on the complete wing in figure 30 indicate that the Reynolds number effects on the windward surface of the straight-wing orbiter are essentially confined to two types of flow phenomenon, namely, transition of a laminar boundary layer to a turbulent boundary layer and shear layer and/or supersonic-jet/boundary-layer interactions (refs. 16 and 17). The influence of the Reynolds number on the second type of flow phenomenon is discussed in the section entitled "Flow Interference Effects on the Wing."

Data for $\alpha = 40^\circ$, 50°, and 60° (figs. 29, 33, and 37) rather definitely indicate transition from a laminar to a turbulent boundary layer. Calculations of local flow conditions were made by assuming both normal- and oblique-shock entropies and then expanding the flow isentropically to the local Newtonian surface pressure. The oblique-shock angles were taken from schlieren photographs. A judgment was made as to the location of the streamline at the shock which was just entering the boundary layer at the transition station. A summary of the local Mach number M_e and local Reynolds number $\rho_e u_e s_{tr}/\mu_e$ at the transition onset location (assuming both normal- and oblique-shock entropies) is given in table I for both the truncated straight-wing orbiter (0.0047 scale) and the fuselage with the wing.

The variation of transition Reynolds number (oblique shock) with transition position is presented in figure 44 for the conditions given in table I. For 60° angle of attack the transition position remains essentially fixed over almost an order of magnitude change in transition Reynolds number. This phenomenon (fixed transition location with increasing transition Reynolds number) is called transition sticking (refs. 13 and 16). Transition sticking may possibly occur at $\alpha = 50^{\circ}$ since the flow field at this angle of attack is subsequently shown to be somewhat similar to that at $\alpha = 60^{\circ}$ and since the one transition point at this angle of attack falls in the $\alpha = 60^{\circ}$ sticking band (fig. 44).

The transition Reynolds number (oblique shock) for the truncated straight-wing configuration is given as a function of angle of attack in figure 45 along with the highest local Reynolds number (based on model length) at which tests were conducted for which transition did not occur. Indications are that the transition Reynolds number decreases with increasing angle of attack on the truncated straight-wing orbiter for $40^{\circ} \leqq \alpha \leqq 60^{\circ}$.

Angle-of-Attack Effects

The change in the truncated straight-wing-orbiter flow field with increasing angle of attack is shown in the electron beam photographs of figure 19. These photographs show the fuselage/wing shock intersection moving inboard along the wing span with increasing angle of attack. Between 40° and 50° angles of attack, the flow field about the wing undergoes a change in that the wing shock standoff distance has suddenly increased very greatly and the fuselage and wing shocks begin to merge. The critical angle-of-attack range in which the flow-field changeover occurs is shown in a subsequent section to depend on the shock density ratio of the test media.

The flow-field changeover with increasing angle of attack is also very evident in the oil-flow patterns in air. The oil-flow patterns of figure 15 for $\alpha = 18^{\circ}$ and 50° $\left(\rho_2/\rho_1 \approx 5.5\right)$ clearly show the effects of the shock/boundary-layer interaction on the wing. They also show the spreading out of the area subjected to interference with increasing angle of attack. Oil-flow patterns at $\alpha = 60^{\circ}$ (fig. 17) show none of the V-shape interference patterns that appeared at the lower angles of attack. The stagnation line on the wing moves slightly downstream of the leading edge as the angle of attack increases; at the higher angles of attack the shock interference effects now appear only as a small distortion in this line. Thus, above the "critical" angle of attack the interference shock interaction is appreciably weakened.

The phase-change heat-transfer patterns also show the effects of the flow-field changeover with increasing angle of attack. In figures 24 and 25 for $\alpha = 20^{\circ}$ and figures 27 and 28 for $\alpha = 40^{\circ}$ $\left(\rho_2/\rho_1 \approx 5.6\right)$, the effects of the shock/boundary-layer interaction is evident from the V-shape heat-transfer-coefficient contours. These patterns compare well with the oil-flow patterns in both location and extent of the shock/boundary-layer interaction effects on the wing. Increasing the angle of attack to 60° in the same test media (air) produces the heat-transfer-coefficient contours of figures 35 and 36.

Outboard of the wing-root interference, the contour lines on the wing are essentially normal to the fuselage and show no qualitative evidence at this angle of attack ($\alpha = 60^{\circ}$) of body-shock—wing-shock intersection/boundary-layer interaction along the wing. However, the camera view angle from which these phase-change contours (figs. 35 and 36) were obtained is misleading in that the wing leading-edge view presented in figure 38 shows contours just downstream of the leading edge (5 percent chord, 38 percent exposed semispan), which indicates a weak shock interaction effect.

Impingement of shock interaction disturbance on wing leading edge.- The effect of angle of attack on the location of the shock interaction disturbance impingement point on the wing leading edge for both the 0.0047- and 0.0093-scale models is shown in figure 46. The data in air were obtained from the nominal heat-transfer-coefficient contours presented previously by extrapolating along the narrow region of high heating produced by the shock/boundary-layer interaction over wing surface to wing leading edge. The data in helium were obtained from the electron-beam photographs of figure 19, the heat-transfer-coefficient contours of figure 34, and the oil-flow patterns of figure 23. Spanwise measurements from the fuselage along the leading edge to the impingement point were made on both wing semispans for each test condition and averaged for the data points shown.

Figure 46 shows the impingement of the transmitted shock (or shocks) and/or shear layer from the fuselage/wing shock intersection moving slightly inboard along the wing leading edge with increasing angle of attack ($20^{\circ} \leqq \alpha \leqq 40^{\circ}$) in both helium and air. For the same model (0.0047 scale), the impingement point is farther outboard in this angle-of-attack range in helium. This anomaly resulted from the larger bow-shock standoff distance in helium (high γ, low density ratio, large shock standoff distance).

As the angle of attack increases above 20° (fig. 46), the bow shock moves closer to the body (fig. 20) and the impingement point of the transmitted shock on the wing moves farther and more rapidly inboard. As the angle of attack increases above 50° in air (fig. 21), the wing shock standoff distance increases drastically and the impingement point begins to move outboard (fig. 46). This increase substantially weakens the bow-shock/wing-shock interaction because of the increasing obliqueness of the shock intersection. As the merger of the two shocks progresses with increasing angle of attack, the shock interaction moves rapidly outboard and disappears somewhere above $\alpha = 50^{\circ}$ for helium and $\alpha = 60^{\circ}$ for air. With increasing wing standoff distance and obliqueness of the shock intersection, a point is reached where no transmitted shock can exist. At this point the effects of the disturbance from the intersection are dissipated somewhat by the distance the disturbance must travel before contacting the wing.

Completely merged shock system.- The heat-transfer data (fig. 40) and oil-flow patterns (figs. 17 and 18) at $\alpha = 80^{\circ}$ show a considerable change from those at the lower angles. The stagnation line on the wing is now near midchord with none of the distortion that appeared at $\alpha = 60^{\circ}$. The bow shock and wing shock have completely merged into essentially one shock envelope and no effect of shock interference heating appears in the heat-transfer contours (fig. 40). At this high angle of attack ($\alpha = 80^{\circ}$), the increase in the effective bluntness of the wing, as indicated by the midchord position of the stagnation line, is responsible for smaller peak heating rates than those which occur on the wing leading edge at the lower angles of attack.

The oil-flow patterns on the body at $\alpha = 80^{\circ}$ (fig. 18), show stagnation-point-type flows along the fuselage center line forward of the wing. These multiple stagnation points are believed to be the cause of the circular heat-transfer patterns on the body shown in figures 10 and 40. The general level of the fuselage heating is at its highest (compared with that at the lower angles of attack) because of the transition from slender to blunt body flow as the angle of attack increases to 80°.

Density-Ratio Effects

For hypersonic flow conditions, the inviscid aerodynamic characteristics of bodies at high angles of attack are determined primarily by the shock density ratio (ref. 2). Equilibrium normal-shock density ratios encountered along the straight-wing-orbiter trajectory for $\alpha = 60^{\circ}$ are given in figure 47. The normal-shock density ratio at peak heating is approximately 18. Since in the earth's atmosphere a density ratio greater than approximately 6 indicates molecular dissociation, the potential for real-gas effects along this trajectory is great. For ground tests at hypersonic Mach numbers where no dissociation occurs, the density ratio across a shock is determined by the specific-heat ratio γ of the gas (the lower γ, the higher the density ratio); thus, ground test data obtained at hypersonic Mach numbers at various values of γ (as already presented herein) can be used to simulate the trends of equilibrium real-gas effects expected in flight.

Flow field.- The influence of the density ratio on the inviscid flow field of the truncated straight-wing orbiter at $\alpha = 60^{\circ}$ can be seen in the flow-visualization photographs of figure 21 for density ratios of 5.6, 5.9, and 12.1. The profile views show that the body shock is much closer to the fuselage at the higher density ratio. (See shock standoff distance distribution of fig. 43.) However, the wing shock bulges out farther than the body shock at the lower density ratio, whereas the wing shock lies inside the body shock at the higher density ratio. The photographs taken normal to the wing span (fig. 21(a)) show the body shock impinging the wing much closer inboard to the body in the higher density-ratio flow, and the wing-shock standoff distance in the higher density-ratio flow is about one-fourth that in the lower flow. Thus, a significant change in the flow field over the wing can be attributed to density-ratio effects. This large change in wing-shock standoff distance at the higher density ratio is believed to be due to a change in the critical angle of attack with density ratio. For the angle-of-attack effect described previously (fig. 19), the flow-field changeover occurs when the density ratio is held constant and the angle of attack is increased. In figure 21, the flow-field changeover occurs when the angle of attack is held constant and the density ratio is increased. The variation of the location of the impingement of the shock interaction disturbance on the wing leading edge with normal-shock density ratio at $\alpha = 60^\circ$ is shown in figure 48. Comparing this figure with that showing the variation of the location of the impingement of the shock-interaction disturbance on the wing leading edge with angle of attack (fig. 46) indicates that below the critical angle of attack, the density ratio has a stronger influence on the impingement location than angle of attack.

Oil-flow patterns obtained at Mach 20 in helium $\left(\rho_2/\rho_1 \approx 4.0\right)$ and in nitrogen $\left(\rho_2/\rho_1 \approx 5.9\right)$ for $\alpha = 40^\circ$ (fig. 22) show the stagnation point near the apex of the orbiter at both density ratios. The effects of shock interference on the wing are clearly visible. This effect is more sharply defined at the higher density ratio with the appearance of a two-prong (V-shape) interference pattern. Also, the wing stagnation streamline is on the leading edge in both density-ratio flows at this angle of attack.

Similar patterns on the truncated straight-wing orbiter for $\alpha = 52^\circ$ in both nitrogen and helium at $M_1 \approx 20$ (fig. 23) show that the stagnation point in the flow with the lower density ratio has moved a significant distance farther downstream than the stagnation point in the flow with the higher density ratio. On the fuselage, the oil-flow patterns show a greater divergence of the viscid streamlines near the edges of the body in the lower density-ratio flow. The oil-flow patterns on the wing in the lower density-ratio flow show a sharp contrast to those at $\alpha = 40^\circ$ (fig. 22). The wing stagnation line (fig. 23, $\rho_2/\rho_1 \approx 4.0$) has moved downstream of the wing leading edge and the only evidence of interference effects is the bend in the stagnation line at approximately 39 percent of the exposed semispan. At the higher density ratio $\left(\rho_2/\rho_1 \approx 5.9\right)$, however, the stagnation line is still on the wing leading edge and shock impingement interference effects across the wing are still apparent but are less severe and farther inboard than those for $\alpha = 40^\circ$.

Heat transfer.- An example of the density-ratio influence on the interference heating from the body-shock/wing-shock intersection can be seen by comparing the nominal heat-transfer-coefficient contours obtained on the truncated straight-wing orbiter in density-ratio flows of 4.0, 5.9, and 5.6 at $\alpha = 40^\circ$ (fig. 31). The heat-transfer-coefficient distribution along the center line of the fuselage is essentially the same for each test condition shown in this figure; however, the contours for a density ratio of 5.6 are swept back to a greater extent on the fuselage than those for 4.0. Also, there is essentially no difference in the level of heating on the wing at this angle of attack between these three density-ratio flows.

The significant difference between the contours obtained in the different density-ratio flows is in the interference effects on the wings. The contours obtained in helium $\left(M_1 \approx 20,\ \rho_2/\rho_1 \approx 4.0\right)$ show only a weak bow-shock/wing-shock interference effect. The contours obtained in nitrogen $\left(M_1 \approx 20,\ \rho_2/\rho_1 \approx 5.9\right)$ at one-half the Reynolds number of that for the helium test show a much stronger bow-shock/wing-shock interference effect. In helium, the wing-root interference is mainly inboard of the wing-body junction. In nitrogen, the wing-root interference is entirely outboard of the wing-body junction. The contours obtained in air $\left(M_1 \approx 8,\ \rho_2/\rho_1 \approx 5.6\right)$ indicate a bow-shock/wing-shock interference effect similar to that for nitrogen $\left(\rho_2/\rho_1 \approx 5.9\right)$.

The foregoing results may be influenced somewhat by the differences in the wall-to-total temperature ratio T_w/T_t; however, this influence is believed to be negligible. The level of noninterference heating on the wing at $\alpha = 40^\circ$ is essentially the same for the helium, nitrogen, and air data at wall-to-total temperature ratios of 0.78, 0.28, and 0.55, respectively. This result is in accord with boundary-layer theory predictions. (See appendix.) If the wall temperature effects on the heat transfer are negligible in the interference-free regions, one might reasonably expect not to see a large wall temperature effect in the regions where interference is present. Furthermore, at $\alpha = 40^\circ$, the intensity of the interference heating, which is governed to some extent by the nature of the boundary layer, is only slightly more severe in nitrogen and air than in helium for the most inboard of the shock/boundary-layer interactions. The pattern of the interference heating for this most inboard interaction is more oblique to the wing chord and somewhat less sharply defined in helium. The pattern of the interference heating for the more outboard wing interaction phenomenon is much more oblique to the wing chord and weaker in helium. This severe divergence and spreading of the wing V-shape interference heating pattern for the helium test compared with that which occurred in air and nitrogen suggest that the controlling mechanism is inviscid.

In helium $\left(\rho_2/\rho_1 \approx 4.0\right)$ at $\alpha = 40^\circ$ (fig. 31), the wing-root interference heating is approximately a factor of 2 higher than the seemingly undisturbed distribution along the wing chord between the wing-body junction and the bow-shock/wing-shock interference region. The bow-shock/wing-shock interference heating (again compared with the seemingly undisturbed inboard distribution) factor is approximately 1.4. In air the shock intersection heating and wing-root interference heating are essentially the same magnitude (interference heating factor of 1.9).

A similar set of heat-transfer-coefficient contours for $\alpha = 60^\circ$ are given in figure 39. In this figure the angle of attack is above the critical value for each of the density-ratio flows. None of these contours show the large V-shape patterns which resulted from bow-shock/wing-shock interference effects at lower angles of attack. The heating distribution and level along the fuselage center line are about the same in each gas. However, a comparison of the lines of constant heat-transfer coefficient on the wing of the orbiter obtained in helium and nitrogen at $M_1 \approx 20$ and in air at $M_1 \approx 8$ shows that the nondimensional level of overall heating is clearly a factor of approximately 2 or higher in air and nitrogen (normal-shock density ratio of 5.6 and 5.9, respectively) than in helium (normal-shock density ratio of 4.0). The contours obtained in air and nitrogen are viewed from a slightly more aft position than those obtained in helium; this gives the somewhat misleading appearance of the slightly more rearward position of the first isotherm in air and nitrogen compared with that in helium. Moreover, regardless of the first isotherm, the evidence supplied by the remaining five or six isotherms on the wing substantiates the factor of approximately 2 difference in the nondimensional level of heating for these density-ratio flows. At very high angles of attack, this trend of an increase in level of heating with an increase in density ratio could have significant effects for the higher density ratios expected in flight.

Again, the influence of the differences in wall-to-total temperature ratios for the data of figure 39 is believed negligible as discussed in the appendix. This lack of influence of wall temperature in the difference in the nondimensional levels of heating on the wing at $\alpha = 60^\circ$ (fig. 39) is more apparent on the wing at $\alpha = 40^\circ$ (fig. 31). At $\alpha = 40^\circ$ where the same wall temperature combination and test conditions exist as at $\alpha = 60^\circ$, no difference in the levels of noninterference heating on the wing was observed. Since interference is more severe and viscous effects more dominant at $\alpha = 40^\circ$ than at $\alpha = 60^\circ$, the fact that no difference in noninterference heating levels exist indicates that the difference in level of heating at $\alpha = 60^\circ$ is due to inviscid-flow-field changes. At $\alpha = 40^\circ$ (below critical angle of attack), the wing shock is weak and the density ratio across this oblique embedded shock is small in both helium and air. At $\alpha = 60^\circ$ (above critical angle of attack), the wing shock is strong and the density ratio across this near-normal embedded shock is comparatively large but much larger for air and nitrogen than for helium because of the limiting density ratio of the flows. The increase in density behind the wing shock increases the local pressures and probably accounts for the higher heating level.

The flow-visualization photographs (schlieren, shadowgraph, electron beam, and oil flow) and the phase-change heat-transfer patterns have shown that a critical angle-of-attack range exists in each gas; this critical range is associated with a large change in the flow field which causes the wing-shock standoff distance to greatly increase, the local stagnation region to move off the wing leading edge toward the central portion of the wing, and the fuselage and wing shock to begin to merge into one shock envelope. The angle-of-attack range at which this phenomenon occurs is relatively independent of stream Mach number but is strongly dependent on shock density ratio – that is, the greater the density ratio, the larger the angle of attack at which the flow-field changeover occurs.

Flow Interference Effects on the Wing

α < critical value (shock intersection).- On and in the vicinity of the wing stagnation line, interference heating results from flow which has been processed by passage through multiple shocks and then stagnated. Interference heating resulting from this type of interference flow structure appears in the phase-change patterns on the wing leading edge. (See, for example, figs. 8 and 38.) As this disturbance proceeds downstream of this region, interference heating results from the more conventional shock-intersection-disturbance/boundary-layer interaction. This type of interference which occurs downstream of the stagnation region is evident throughout the flow-visualization photographs and heat-transfer-coefficient contours of this report (figs. 15, 24, 25, 27, 28, and 30) for angles of attack below the "critical" range (below the angle of attack at which the wing shock standoff distance increases drastically and the wing stagnation line moves downstream of the wing leading edge).

The spanwise heat-transfer-coefficient distribution at various chord locations over the truncated wing of the 0.0093-scale model at $\alpha = 20^{\circ}$ is given in figures 49(a) and 49(b) for Mach 8 and Mach 10.3, respectively. The spanwise distributions at the two Mach numbers are essentially the same except for the shock-intersection-disturbance/boundary-layer interaction which is slightly more inboard (2.5 percent of exposed semispan) at Mach 10.3 as expected. At Mach 8 and 10.3, the wing-root interference heating is only slightly less severe in level and extent than that produced by the transmitted-shock/boundary-layer interaction.

Similar heat-transfer-coefficient distributions over the truncated wing at $\alpha = 40^{\circ}$ are given in figure 50. The Mach 8 data (fig. 50(a)) were obtained with the 0.0047-scale model and the Mach 10.3 data were obtained with the 0.0093-scale model. The slight bluntness deficiency (fig. 5) in the 0.0047-scale model is reflected in the more inboard location of the interference heating from the shock-intersection-disturbance/boundary-layer interaction for the Mach 8 data (25.5 percent of exposed semispan, fig. 50(a)) over that for the Mach 10 data (30 percent of exposed semispan, fig. 50(b)). The sensitivity of shock intersection disturbance impingement location on the wing to the fuselage bluntness is noted in reference 18.

The spanwise heat-transfer distribution at the 5-percent-chord location obtained by Seegmiller (ref. 14) on an untruncated wing instrumented with thermocouples (slightly different configuration, see p. 12), is shown in figures 50(a) and 50(b). The position of the interference heating from the shock-intersection-disturbance/boundary-layer interaction is in reasonable agreement with that of the Mach 10.3 data (fig. 50(b)) but is slightly outboard (5 percent of the exposed semispan) of that of the Mach 8 data (fig. 50(a)). The Mach 10.3 data were obtained with the 0.0093-scale model whose wings were truncated at 51.5 percent of the exposed semispan and the Mach 8 data were obtained with the 0.0047-scale model whose wings were truncated at 56.8 percent of the exposed semispan. Seegmiller's data which were obtained on a complete wing are in fair agreement with the data obtained on the more truncated model. This result essentially rules out any truncation effects. Therefore, the discrepancy between Seegmiller's data and the Mach 8 data is probably due to the difference in the bluntness of the models (fig. 5). The level of this distribution (Seegmiller's) in the shock interference heating region is in reasonable accord with both sets of the present data. However, the data presented herein (Mach 8 and 10.3) show that the wing-root interference heating is almost as severe as the shock interference heating, whereas Seegmiller's data show no indication of wing-root effects.

Two fuselage/wing shock intersection interference flow models for angles of attack below the critical value have been proposed for the straight-wing orbiter. Seegmiller's shock intersection and impingement model (ref. 14) is presented in figure 51 and Edney's type V shock/shock interaction model (ref. 17) as proposed by McDonnell Douglas (ref. 19) and supported by Bertin and associates (ref. 18) is presented in figure 52. The data presented herein are not sufficient to substantiate either of these shock interference flow models; however, the electron-beam photographs in helium (fig. 19) which clearly show the transmitted shock (interference shock in fig. 51) show no evidence of the second shock which appears in Seegmiller's shock interference flow model.

The influence of Reynolds number on the interference heating resulting from either the shear-layer or supersonic-jet impingement (depending on the flow model one accepts) on the wing surface can be seen by comparing the heat-transfer-coefficient contours given in this region in figure 24 for $\alpha = 20^\circ$ and in figure 30 for $\alpha = 40^\circ$.

α > critical value.- At an angle of attack of 50° in helium (fig. 19) and 60° in air (figs. 20 and 21), the wing-shock standoff distance has increased substantially over that at lower angles of attack and the wing stagnation line has moved downstream of the leading edge. The steeper shock angle is forcing the bow shock closer to the fuselage. Thus, the wing shock and fuselage shock begin to merge into essentially a single shock envelope. The wing/fuselage shock intersection is now so oblique that the shock/boundary layer and/or shear-layer/boundary-layer interaction noted at the lower angles of attack has disappeared. This disappearance is evident in the oil-flow patterns of figure 16 where the patterns on both the complete and truncated wings in air show only a distortion in the wing stagnation line. The stagnation lines on the complete and truncated wings are shown superimposed in figure 53. The distortion from the truncated-wing oil-flow results is slightly inboard of that on the complete wing; this is probably due to the slight difference in the fuselage bluntness between the two models rather than to the truncation.

The heat-transfer-coefficient contours in the vicinity of the leading edge of the truncated wing at $\alpha = 60^{\circ}$ in air are shown in figure 38. The V-shape heating patterns of the shock/boundary-layer interaction no longer appear inasmuch as the shock-interaction interference effects are now confined to the leading-edge region in the vicinity of the 35-percent exposed semispan. The extent of wing-root interference heating has increased substantially over that at the lower angles of attack. The spanwise (junction of leading edge and fuselage taken as zero point) heat-transfer-coefficient distributions at the 5-percent-chord and 20-percent-chord locations at $\alpha = 60^{\circ}$ in air are given in figure 54. Seegmiller's data (ref. 14) at the two chord locations on the complete wing are also shown. Peak heating now occurs in the wing-root interference. The effects of fuselage/wing shock interaction at the 5-percent-chord location appear slightly more inboard on the 0.0047-scale truncated model (32 percent of exposed semispan) than on the complete wing (36 percent of exposed semispan). As pointed out previously, this more inboard appearance is due to the slight difference in fuselage bluntness between the two models (fig. 5) and not to the truncation. Again, the sensitivity of the position of the shock impingement on the wing to fuselage bluntness is noted in reference 18. At $\alpha = 80^{\circ}$, the fuselage shock and wing shock have essentially merged into one shock envelope; thus, no shock-interaction interference effects appear.

Maximum Heating and Equilibrium Temperatures

Windward surface.- For an angle of attack of 60° and below, the highest heating rates on the wing are still considerably above the highest values on the body. However, there is a large decrease in maximum heat-transfer coefficient and maximum skin temperature with an increase in angle of attack. A comparison of these maximum values can be made from the following compilation:

α, deg	Figure	Maximum h/h_{ref}	Maximum T_w, K	Location of maximum values
20	24(b)	1.184	2410	Wing
40	27	1.032	2108	Wing
50	32	Not measured	----	Wing
60	38	0.563	1753	Wing
80	40	0.178	1343	Wing and fuselage

For angles of attack up to 60°, the decrease in maximum skin temperature is due to both a decrease in the reference $\dot{Q}_{max}$ value (0.3048-m-sphere value) with angle of attack (fig. 14) and the change in heat-transfer distribution over the model shown by the foregoing maximum h/h_{ref} values. However, for $\alpha = 80^{\circ}$, the large decrease in maximum heat-transfer coefficient and skin temperature is due entirely to the change in heat-transfer distribution over the model as the reference $\dot{Q}_{max}$ value of figure 14 increases with an increase in angle of attack for angles above 60°. It is interesting to note that for $\alpha = 80^{\circ}$ the maximum heating on the wing is the same as the maximum heating on the body.

Side.- The maximum equilibrium values of the skin temperature obtained on the side of the model are shown in figure 42. With the exception of the skin temperature for $\alpha = 20^{\circ}$ which is believed to be influenced by the thickened wing section, the interference on the side of the body due to the wing results in higher skin temperature at the higher angle of attack.

SUMMARY OF RESULTS

The results of a series of phase-change heat-transfer and flow-visualization tests at Mach 7.4, 8, and 10.3 in air, Mach 19.5 in nitrogen, Mach 20.3 in helium, and Mach 6 in tetrafluoromethane (CF_4) on a straight-wing reentry configuration for angles of attack from 20° to 80° are summarized as follows:

(1) For hypersonic stream Mach numbers $(M_\infty \geqq 6)$, the flow field over the straight-wing configuration is essentially independent of Mach number.

(2) The transition Reynolds number decreases with increasing angle of attack α for $40^{\circ} \leqq \alpha \leqq 60^{\circ}$. At $\alpha = 60^{\circ}$ the transition position remains essentially fixed over almost an order of magnitude change in transition Reynolds number.

(3) The impingement position of the transmitted shock from the fuselage/wing shock intersection moves slightly inboard along the wing leading edge with increasing angle of attack. At some "critical" angle of attack, the wing-shock standoff distance is greatly increased and the stagnation line moves downstream of the wing leading edge. At this critical angle, further increases in the angle of attack move the impingement position outboard and slightly downstream of the leading edge as the merger of the two shocks stifles the interaction.

(4) The value of the critical angle of attack is very sensitive to flow shock density ratio or effective gamma. This critical angle of attack is higher for higher shock-density-ratio flows. In helium the critical angle of attack is between 40° and 50°, in air it is between 50° and 60°, and in CF_4 it is above 60°.

(5) At angles of attack above the critical for all gases, the level of heat transfer to the wing is higher for the higher shock-density-ratio flows (increasing the density ratio ρ_2/ρ_1 from 4 to 5.6 essentially doubles the wing heating rate). This effect is believed to be due to a higher pressure level on the wing resulting from the higher shock-density-ratio flow.

(6) Interference from fuselage/wing shock interaction resulted in a large area with increased heating rates on the windward surface of the wing at $\alpha = 20^\circ$, 40°, and 50° for flows with a normal-shock density ratio equal to or greater than 5.6. At $\alpha = 60^\circ$ this interference was much weaker and exhibited an entirely different heating distribution. At $\alpha = 80^\circ$ shock interference did not appear.

(7) At 60° angle of attack and lower $\left(\text{again for flows with } \rho_2/\rho_1 \geqq 5.6\right)$, a large portion of the wing surface had heating rates higher than the highest heating rates on the body, but at $\alpha = 80^\circ$ the highest heating rates on the wing and body were about equal.

Langley Research Center,
National Aeronautics and Space Administration,
Hampton, Va., January 17, 1973.

APPENDIX

INFLUENCE OF WALL-TO-TOTAL TEMPERATURE RATIO ON HEAT-TRANSFER COEFFICIENT

In obtaining heating data in relatively low enthalpy wind tunnels with the phase-change-coating heat-transfer technique, it is often necessary to use phase-change paint temperatures that result in high values of the wall-to-total temperature ratio. When comparing data with large differences in the wall-to-total temperature ratio as in figures 31 and 39, the question arises as to the influence of the wall temperature on the heat-transfer coefficient.

The product of the Stanton number and square root of local Reynolds number $N_{St}\sqrt{R_{e,s}}$ for a flat plate is given as a function of local Mach number M_e in figure 55(a) for a total temperature of 467 K in helium, in figure 55(b) for a total temperature of 810 K in air (representative of the Mach 8 tests), and in figure 55(c) for a total temperature of 1644 K in air (representative of the Mach 19.5 tests in nitrogen). Also, the $N_{St}\sqrt{R_{e,s}}$ distributions are given for wall-to-total temperature ratios T_w/T_t of 0.28, 0.55, and 0.78 in figure 55. These distributions were obtained by using the laminar-boundary-layer similar solutions of references 20 and 21.

The only variable affected by wall temperature in the parameter $N_{St}\sqrt{R_{e,s}}$ is the heat-transfer coefficient h. A change in $N_{St}\sqrt{R_{e,s}}$ with wall temperature reflects a change in h. If the flat-plate similar solutions are assumed to give an adequate indication of the influence of wall temperature on the heat-transfer coefficient on the windward surface of the straight-wing orbiter in the regions free of flow interference, the data at different wall temperatures given in figures 31 and 39 could be converted to a common wall temperature from the plots of figure 55. At $\alpha = 40^{\circ}$, the local Mach number M_e is less than 2 on the fuselage center line and probably nearer 1 on the wing. In this local Mach number range in helium, there is only a 3- to 4-percent difference between the heat-transfer coefficients at $T_w/T_t = 0.78$ and $T_w/T_t = 0.55$ (fig. 55). Similarly for the nitrogen data of figures 31 and 39 $\left(T_t = 1644 \text{ K}, \quad T_w/T_t = 0.28\right)$, there is only a 5- to 6-percent difference between heat-transfer coefficients at $T_w/T_t = 0.28$ and at $T_w/T_t = 0.55$ (fig. 55(c)). At $\alpha = 60^{\circ}$, the local Mach number is subsonic on most of the windward surface of the orbiter and the wall temperature effects on the heat-transfer coefficient are less than at $\alpha = 40^{\circ}$. Thus, if any similarity exists between the interference-free boundary layer on the windward surface of the fuselage and wing of the straight-wing orbiter and results of similar solutions for the boundary layer on a flat plate, the wall temperature effects on the interference-free data presented herein are negligible.

REFERENCES

1. Faget, Max: Space Shuttle: A New Configuration. Astronaut. & Aeronaut., vol. 8, no. 1, Jan. 1970, pp. 52-61.

2. Jones, Robert A.; and Hunt, James L. (With appendix A by James L. Hunt, Kathryn A. Smith, and Robert B. Reynolds, and appendix B by James L. Hunt and Lillian R. Boney): Use of Tetrafluoromethane To Simulate Real-Gas Effects on the Hypersonic Aerodynamics of Blunt Vehicles. NASA TR R-312, 1969.

3. Hunt, James L.; and Creel, Theodore R., Jr.: Shock Interference Heating and Density-Ratio Effects. Part II – Hypersonic Density-Ratio Effects. NASA Space Shuttle Technology Conference, Vol. 1, NASA TM X-2272, 1971, pp. 217-243.

4. Jones, Robert A.; and Hunt, James L.: Use of Fusible Temperature Indicators for Obtaining Quantitative Aerodynamic Heat-Transfer Data. NASA TR R-230, 1966.

5. Stainback, P. Calvin: Heat-Transfer Measurements at a Mach Number of 8 in the Vicinity of a 90° Interior Corner Alined With the Free-Stream Velocity. NASA TN D-2417, 1964.

6. Schaefer, William T., Jr.: Characteristics of Major Active Wind Tunnels at the Langley Research Center. NASA TM X-1130, 1965.

7. Clark, Frank L.; Ellison, James C.; and Johnson, Charles B.: Recent Work in Flow Evaluation and Techniques of Operations for the Langley Hypersonic Nitrogen Facility. NASA paper presented at Fifth Hypervelocity Techniques Symposium (Denver, Colo.), Mar. 28-30, 1967.

8. Arrington, James P.; Joiner, Roy C., Jr.; and Henderson, Arthur, Jr.: Longitudinal Characteristics of Several Configurations at Hypersonic Mach Numbers in Conical and Contoured Nozzles. NASA TN D-2489, 1964.

9. Loving, Donald L.; and Katzoff, S.: The Fluorescent-Oil Film Method and Other Techniques for Boundary-Layer Flow Visualization. NASA MEMO 3-17-59L, 1959.

10. Liepmann, H. W.; and Roshko, A.: Elements of Gasdynamics. John Wiley & Sons, Inc., c.1957.

11. Weinstein, Leonard M.; Wagner, Richard D., Jr.; Henderson, Arthur, Jr.; and Ocheltree, Stewart L.: Electron Beam Flow Visualization in Hypersonic Helium Flow. Paper presented at the 1969 IEEE Third International Congress on Instrumentation in Aerospace Simulation Facilities (Farmingdale, N.Y.), May 1969.

12. Fay, J. A.; and Riddell, F. R.: Theory of Stagnation Point Heat Transfer in Dissociated Air. J. Aeronaut. Sci., vol. 25, no. 2, Feb. 1958, pp. 73-85, 121.

13. Henderson, Arthur; Dunavant, James C.; and Jones, Robert A.: Heating Studies on Manned Space Shuttle Concepts. Paper presented at Space Technology and Heat Transfer Conference ASME (Los Angeles), June 1970.

14. Seegmiller, H. Lee: Shock Interference Heating and Density-Ratio Effects. Part I – Flow Field Visualization, Thermocouple Measurements, and Analysis. NASA Space Shuttle Technology Conference, Vol. I, NASA TM X-2272, 1971, pp. 185-215.

15. Marvin, J. G.; Seegmiller, H. L.; Lockman, W. K.; Mateer, G. G.; Pappas, C. C.; and DeRose, C. E.: Surface Flow Patterns and Aerodynamic Heating on Space Shuttle Vehicles. AIAA Paper No. 71-594, June 1971.

16. Hefner, Jerry N.: Boundary-Layer Transition for Space-Shuttle-Type Configurations at Angles of Attack. NASA TM X-2254, 1971.

17. Edney, Barry E.: Shock Interference Heating and the Space Shuttle. Space Transportation System Technology Symposium, NASA TM X-52876, Vol. I, 1970, pp. 338-389.

18. Bertin, John J.; Williams, Frank E.; Baker, Robert C.; Goodrich, Winston D.; and Kessler, William C.: Aerothermodynamic Measurements for Space Shuttle Configurations in Hypersonic Wind Tunnels. Space Shuttle Aerothermodynamics Technology Conference, Vol. II, NASA TM X-2507, 1972, pp. 469-501.

19. Kessler, W. C.; Reilly, J. F.; and Sampatcos, E.: Hypersonic Shock Wave Interaction and Impingement. MDC E0427, McDonnell Douglas Corp., July 21, 1971.

20. Beckwith, Ivan E.; and Cohen, Nathaniel B.: Application of Similar Solutions to Calculation of Laminar Heat Transfer on Bodies With Yaw and Large Pressure Gradient in High-Speed Flow. NASA TN D-625, 1961.

21. Cohen, Nathaniel B.: Boundary-Layer Similar Solutions and Correlation Equations for Laminar Heat-Transfer Distribution in Equilibrium Air at Velocities up to 41,100 Feet Per Second. NASA TR R-118, 1961.

TABLE I.- TRANSITION CONDITIONS AND LOCATION ON WINDWARD SURFACE OF FUSELAGE

M_1	α, deg	Wing	$R_{\infty,l}$	s_{tr}/l	$\left(\frac{\rho_e u_e}{\mu_e}\right)_{NS}$, m^{-1}	$\left(\frac{\rho_e u_e s_{tr}}{\mu_e}\right)_{NS}$	$\left(\frac{\rho_e u_e}{\mu_e}\right)_{OS}$, m^{-1}	$\left(\frac{\rho_e u_e s_{tr}}{\mu_e}\right)_{OS}$	$(M_e)_{NS}$	$(M_e)_{OS}$
7.4	40	No	9.6×10^6	0.20	4.56×10^6	0.40×10^6	6.23×10^6	0.55×10^6	1.05	1.3
8.0	50	Yes	4.3	.53	3.71	.42	6.04	.68	.86	1.2
7.4	60	No	9.6	.40	3.91	.69	4.59	.80	.65	.8
7.9	60	Yes	3.0	.47	2.23	.22	2.56	.25	.65	.74
7.9	60	Yes	2.1	.50	1.54	.17	1.84	.20	.65	.74

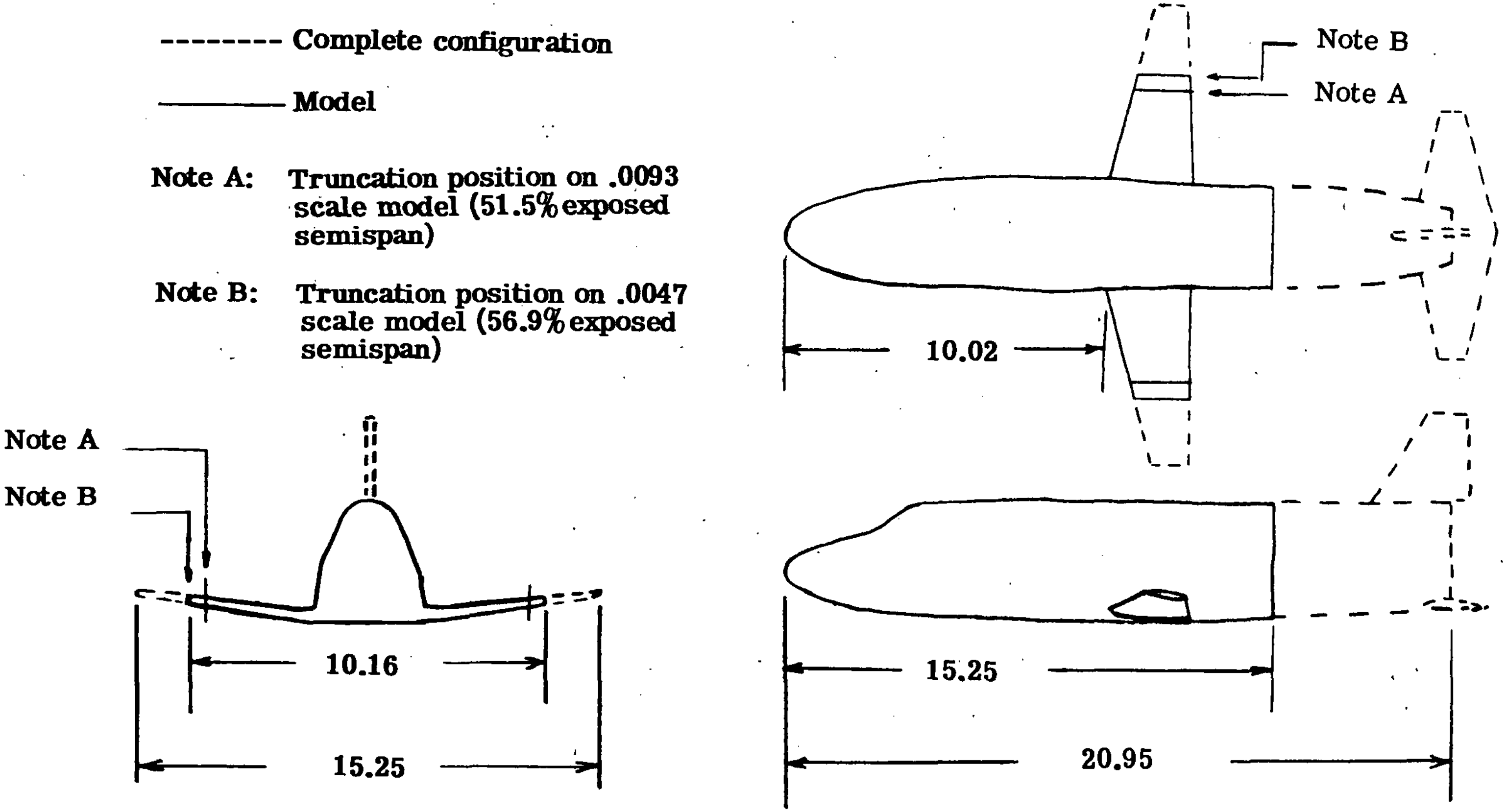

Figure 1.- Straight-wing-orbiter model (0.0047 scale). Dimensions are in centimeters.

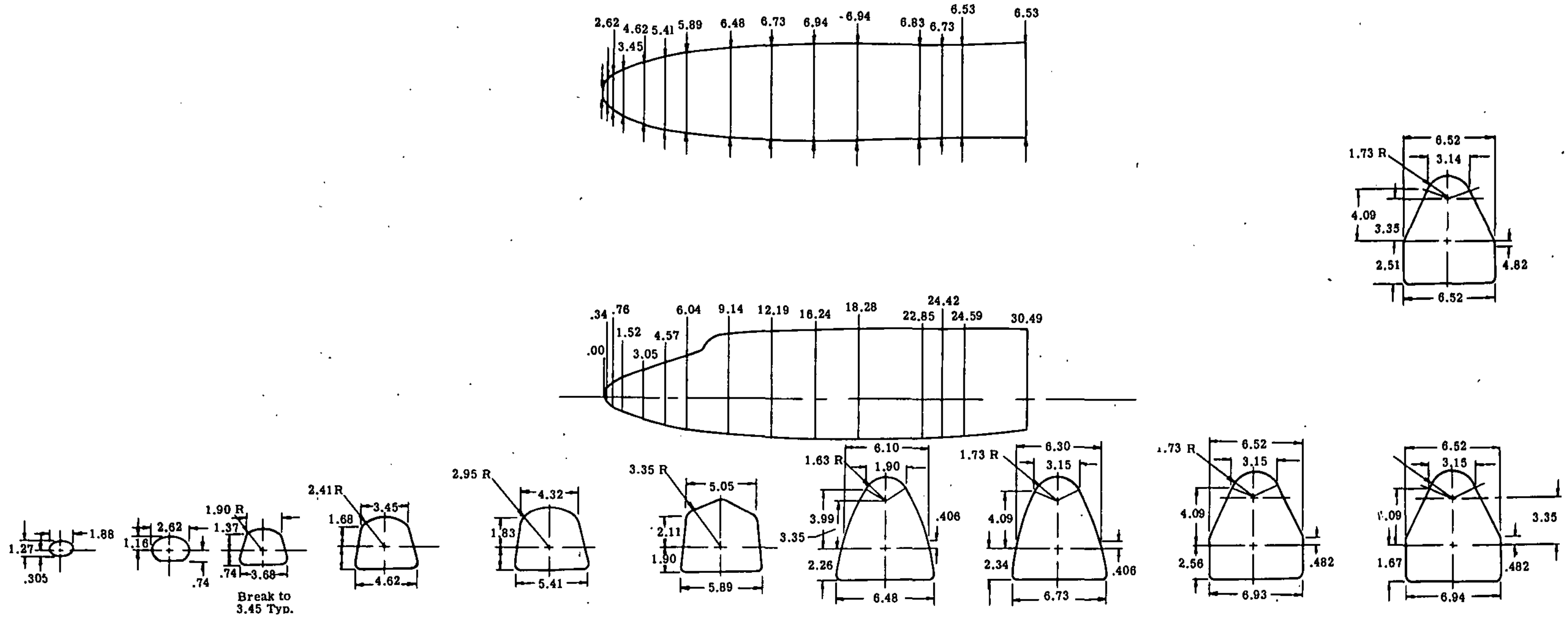

(a) Fuselage (0.0093 scale).

Figure 2.- Nominal coordinates (in centimeters) of straight-wing orbiter.

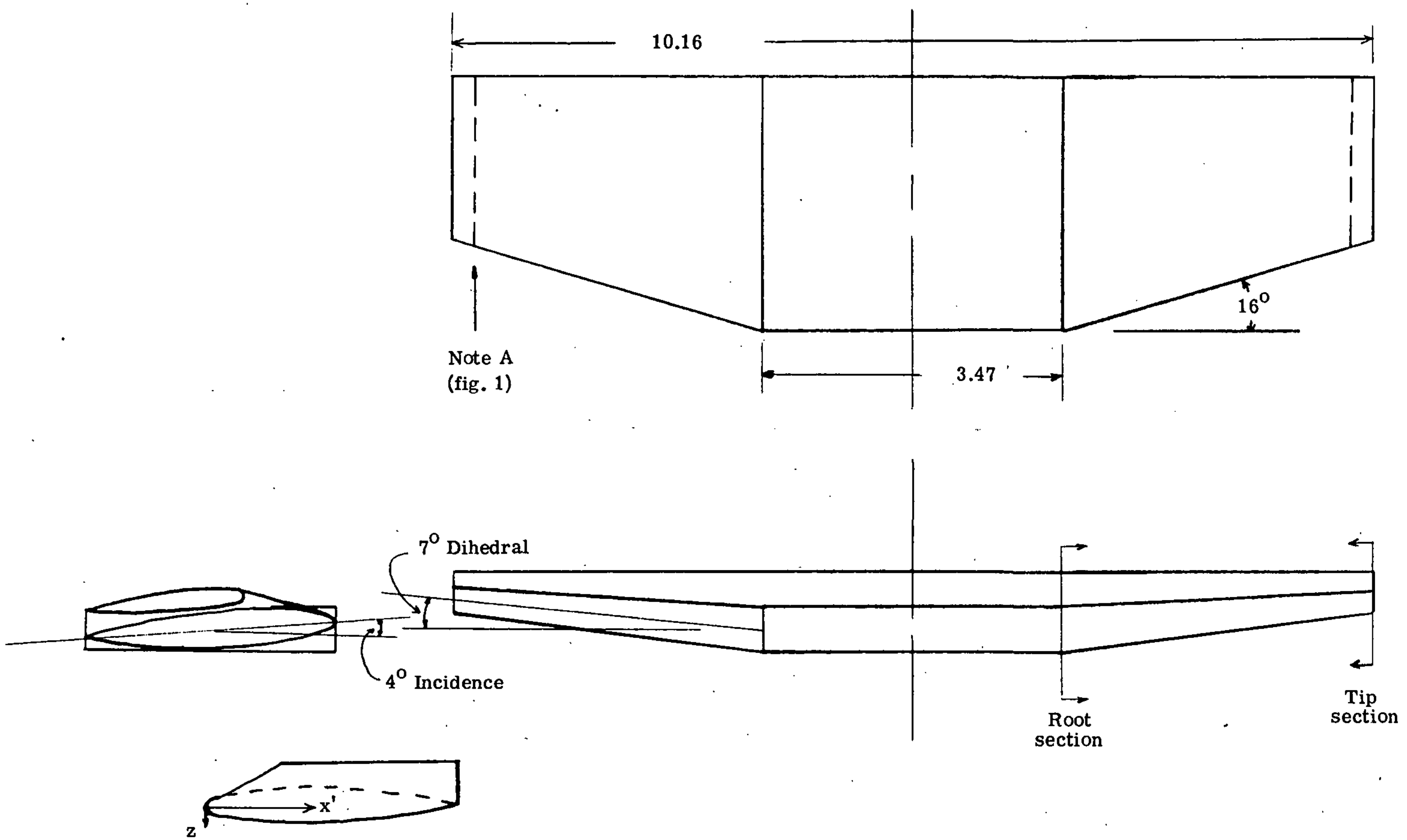

Root		Tip	
x'	z	x'	z
2.793	0	1.829	0
.418	.152	.273	.099
1.391	.194	.904	.127
2.506	.054	1.637	.355
2.780	.005	1.815	.0033
L.E. RAD. = 0.056		L.E. RAD. = 0.038	

(b) Wing (0.0047 scale).

Figure 2.- Concluded.

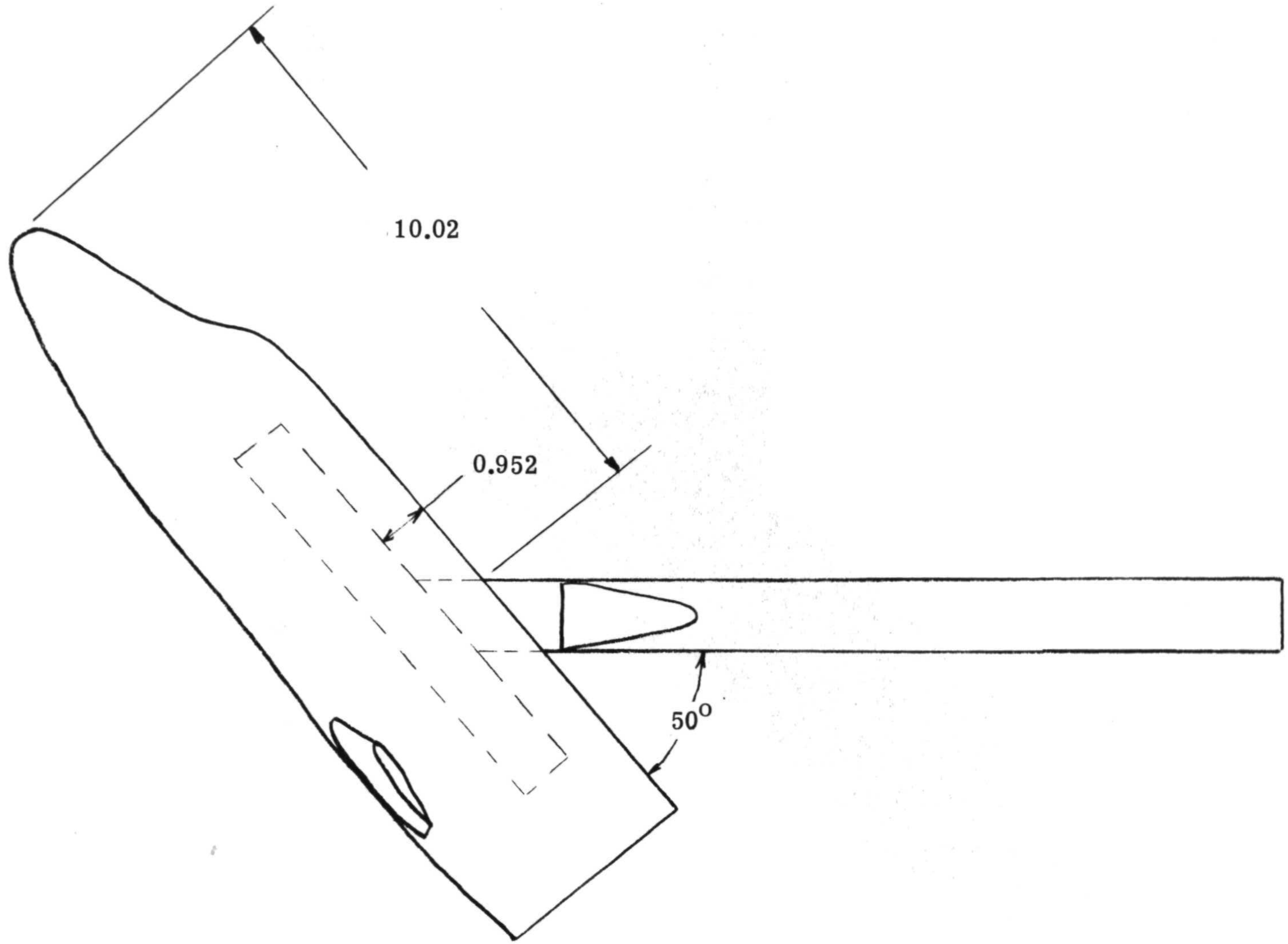

Figure 3.- Sting arrangement with 0.0047-scale model. Dimensions are in centimeters.

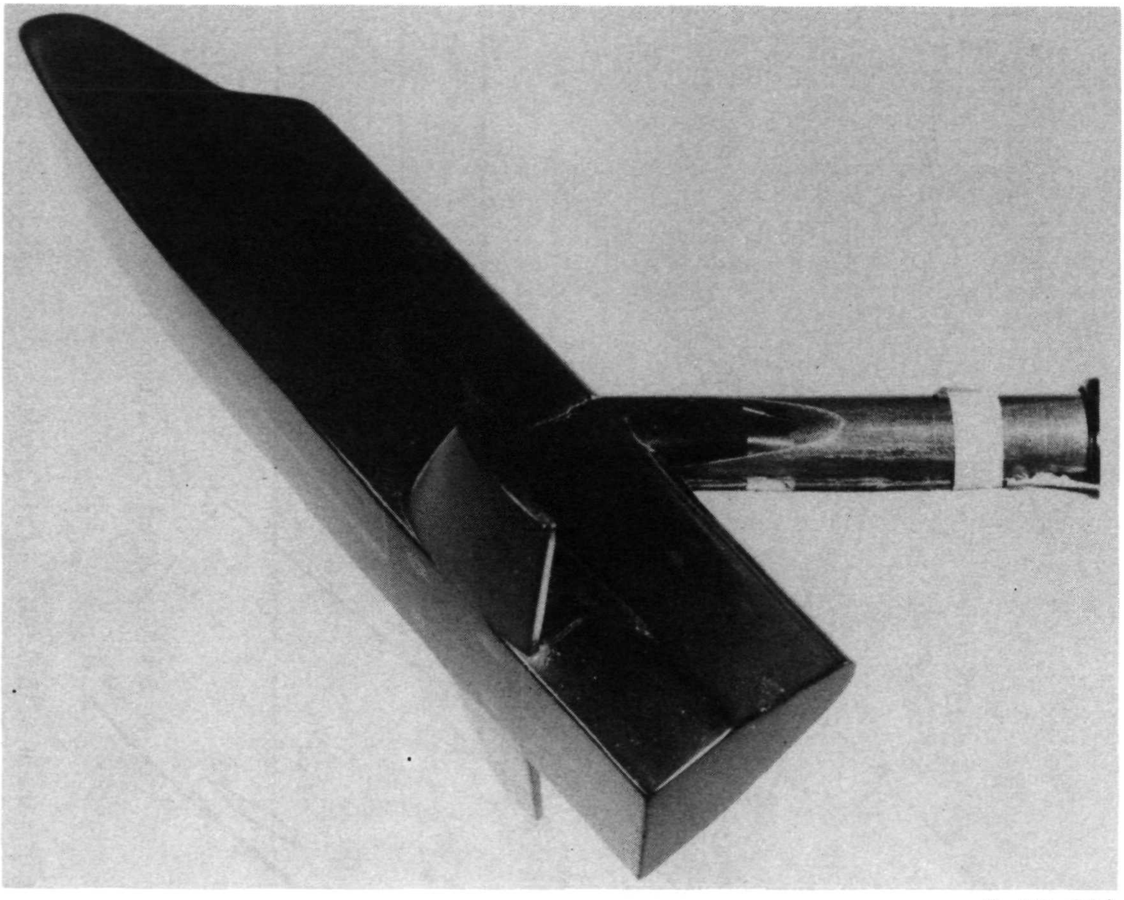

L-73-214

Figure 4.- The 0.0093-scale model.

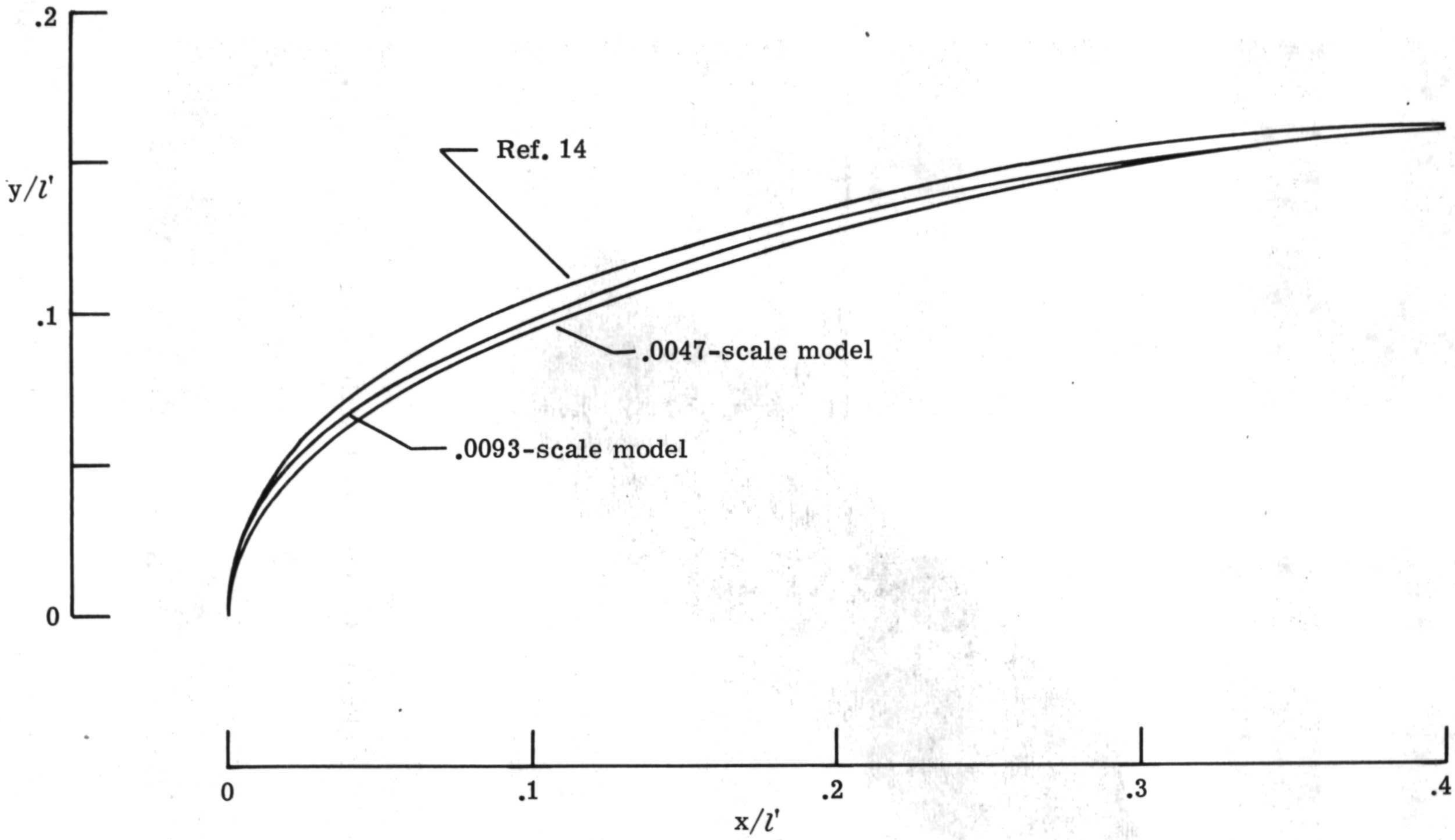

Figure 5.- Measured fuselage profiles.

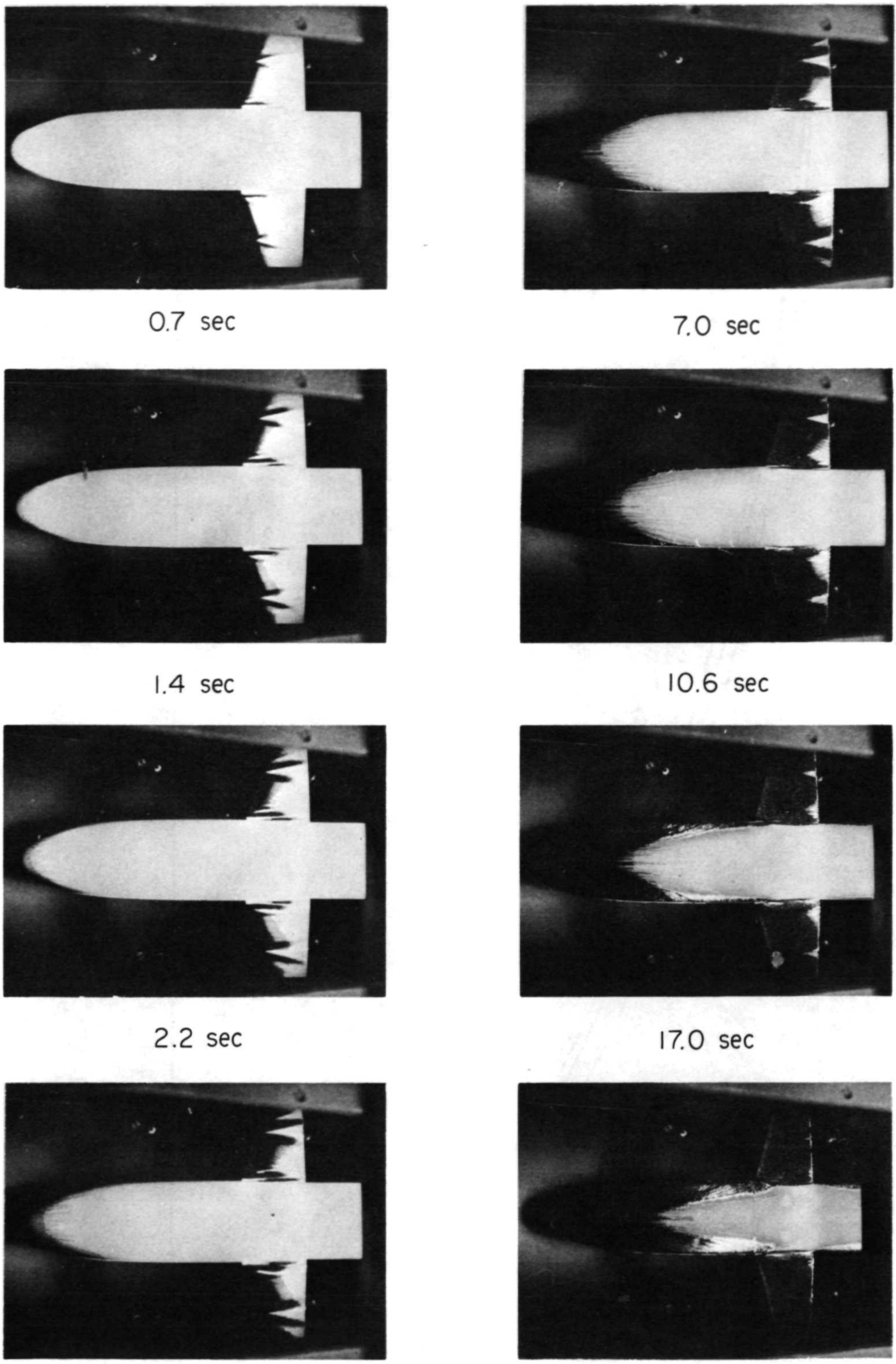

0.7 sec

1.4 sec

2.2 sec

4.0 sec

7.0 sec

10.6 sec

17.0 sec

24.2 sec

L-73-215

Figure 6.- Phase-change patterns obtained in Langley Mach 8 variable-density hypersonic tunnel at $\alpha = 20^{\circ}$. $R_{\infty,l} = 1.45 \times 10^{6}$.

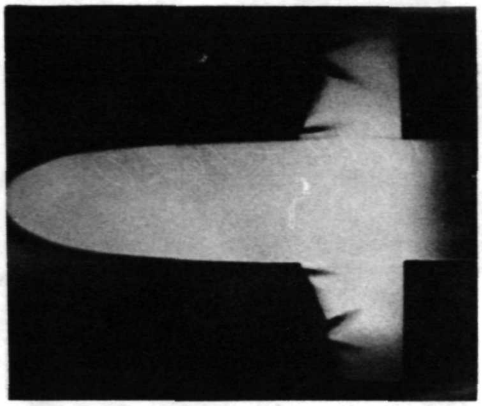

0.7 sec

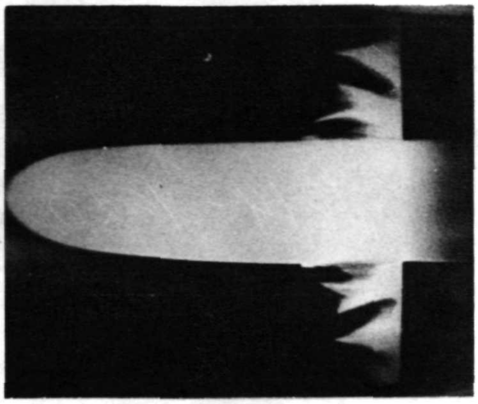

4.0 sec

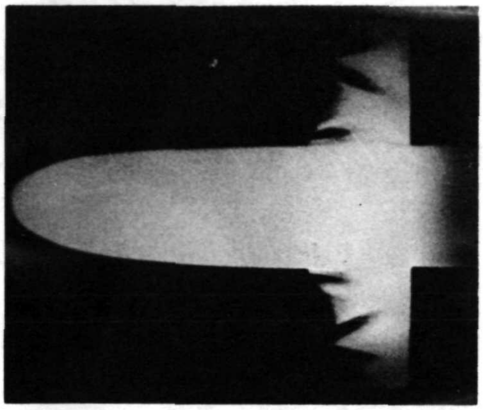

1.4 sec

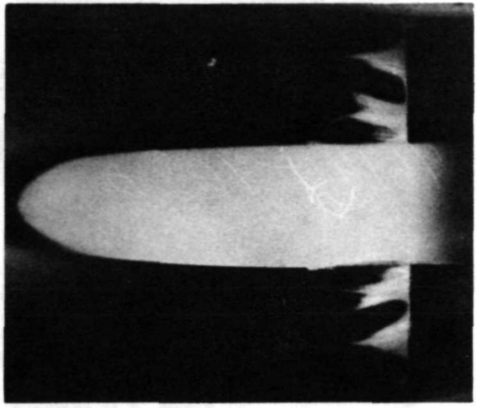

7.0 sec

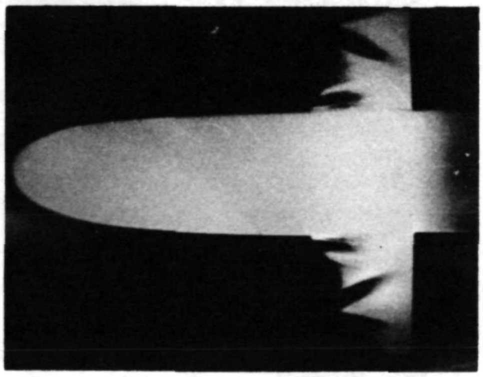

2.2 sec

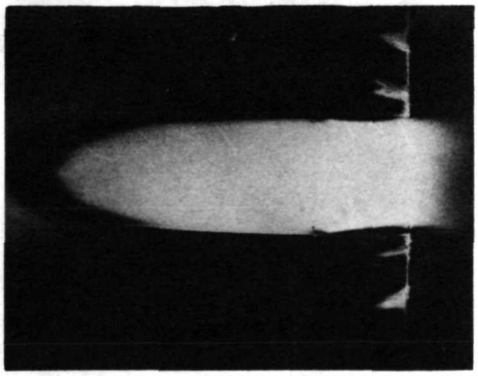

14.0 sec

L-73-216

Figure 7.- Phase-change patterns obtained in Langley Mach 8 variable-density hypersonic tunnel at $\alpha = 40^{\circ}$. $R_{\infty,l} = 1.45 \times 10^{6}$.

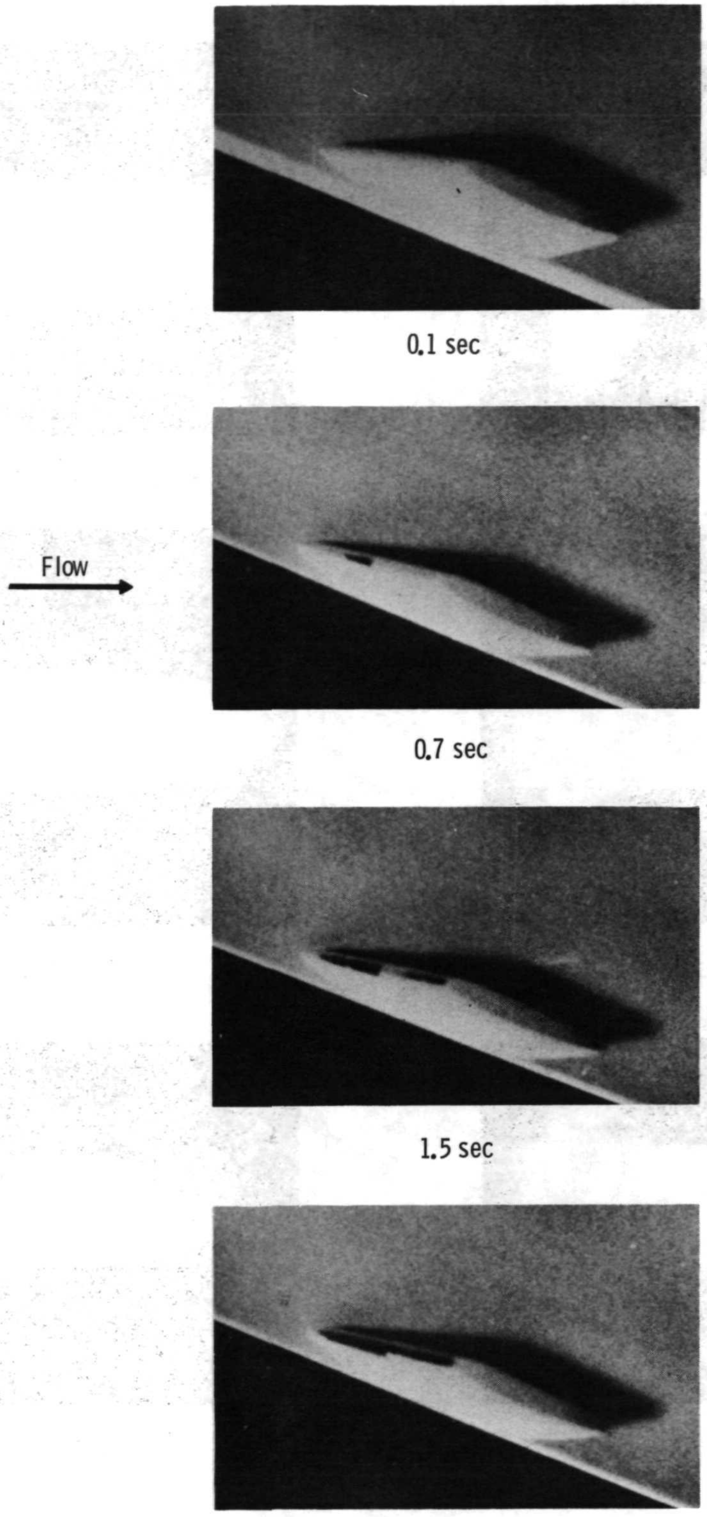

L-73-217

Figure 8.- Phase-change patterns obtained on leading edge of wing in Langley Mach 8 variable-density hypersonic tunnel at $\alpha = 20^{\circ}$.

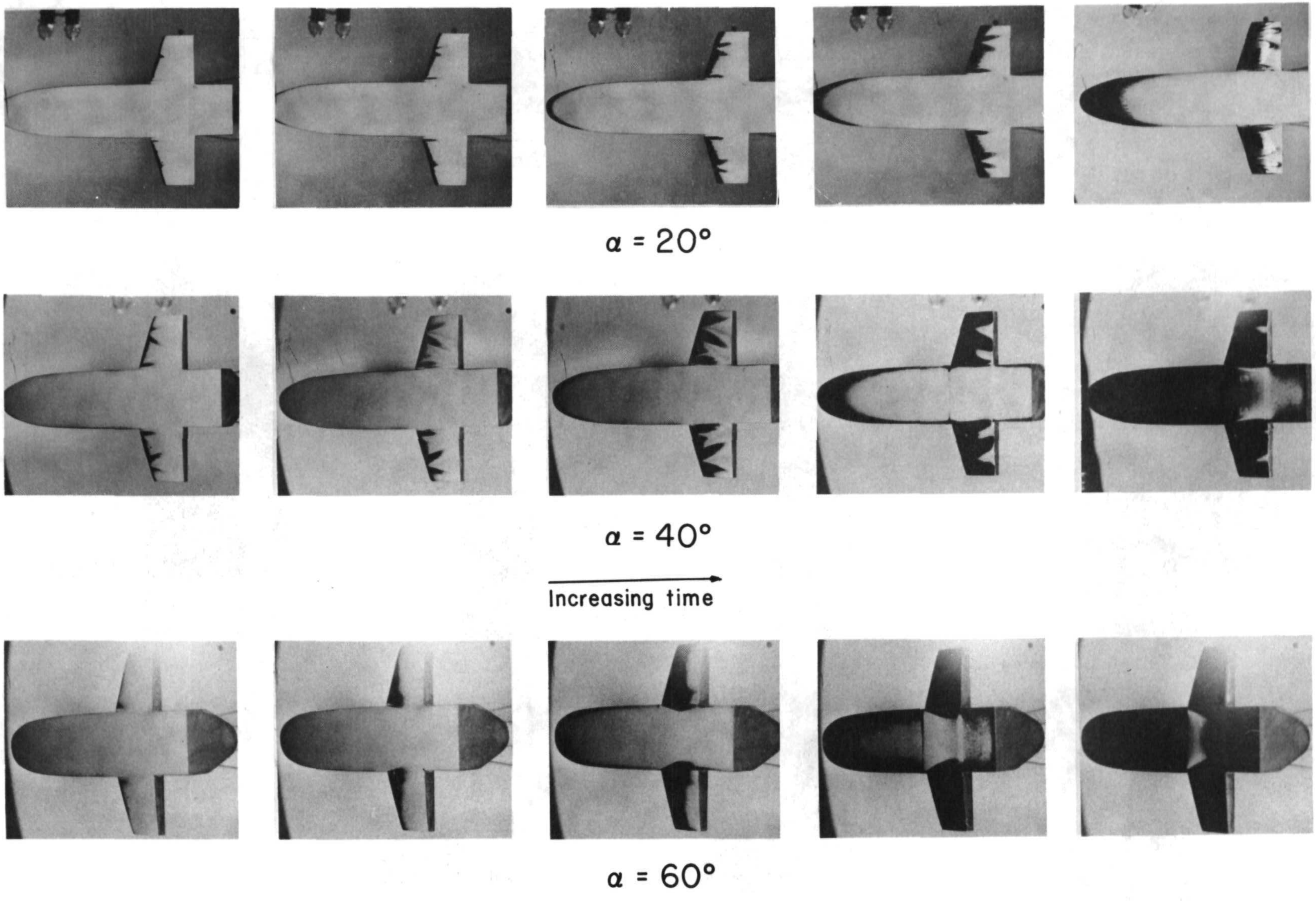

L-73-218

Figure 9.- Phase-change patterns obtained in Langley continuous-flow hypersonic tunnel. $R_{\infty,l} = 1.80 \times 10^6$.

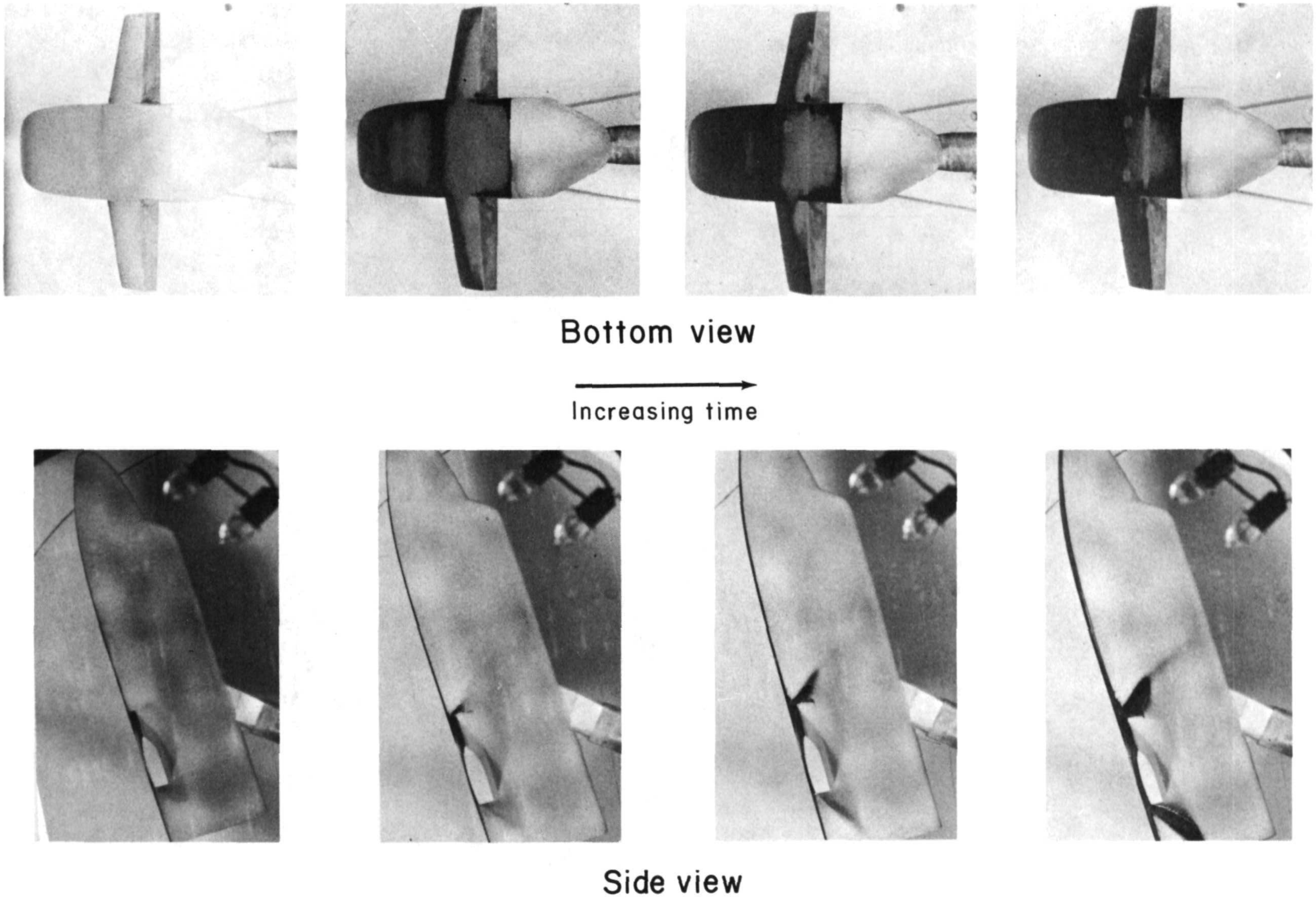

L-73-219

Figure 10.- Phase-change patterns obtained in Langley continuous-flow hypersonic tunnel at $\alpha = 80^{\circ}$. $R_{\infty,l} = 1.80 \times 10^{6}$.

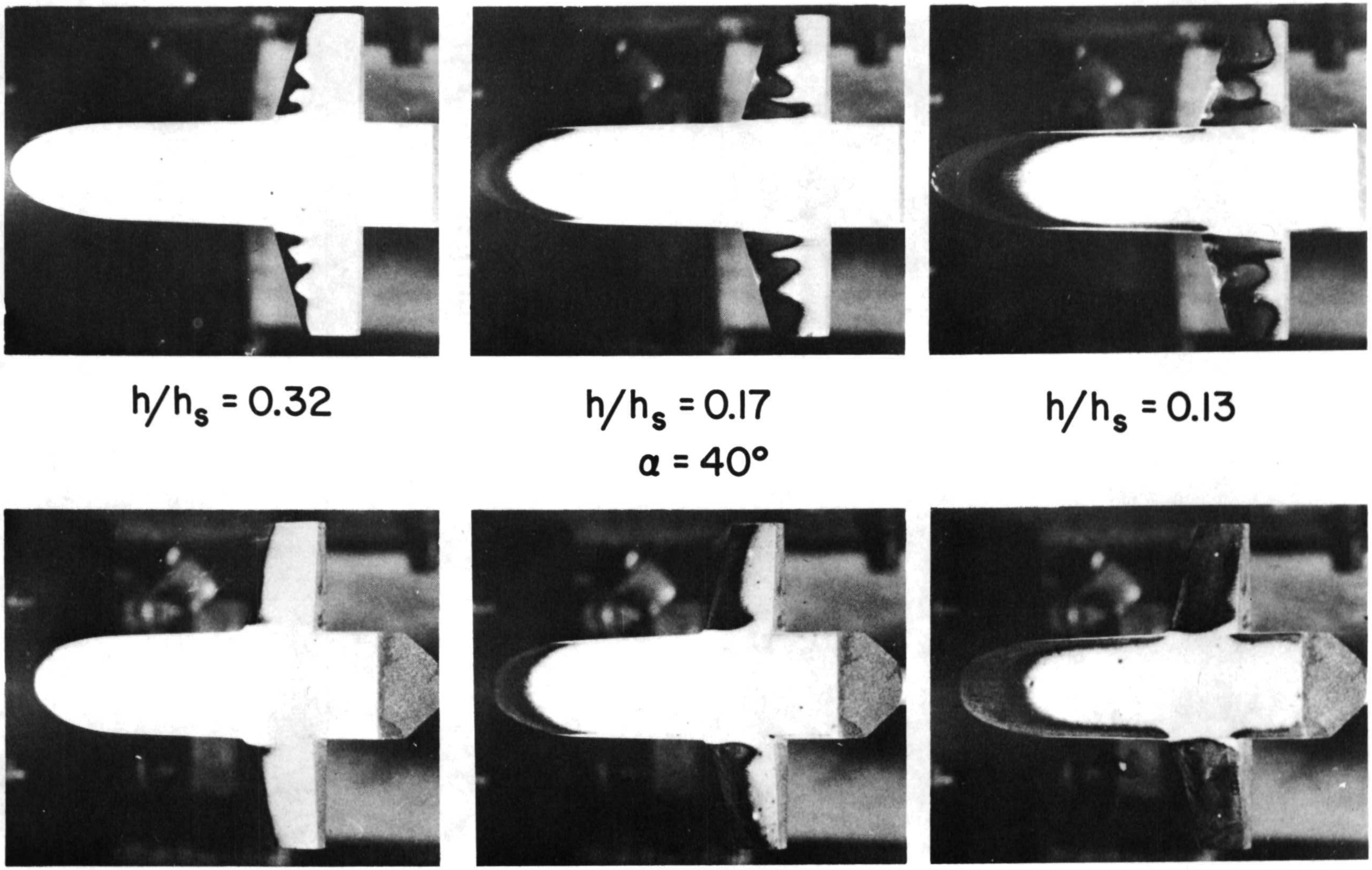

$h/h_s = 0.32$

$h/h_s = 0.17$
$\alpha = 40°$

$h/h_s = 0.13$

$h/h_s = 0.32$

$h/h_s = 0.19$
$\alpha = 60°$

$h/h_s = 0.14$

L-73-220

Figure 11.- Phase-change patterns obtained on truncated straight-wing orbiter in Langley hypersonic nitrogen tunnel. $M_1 = 19.5$.

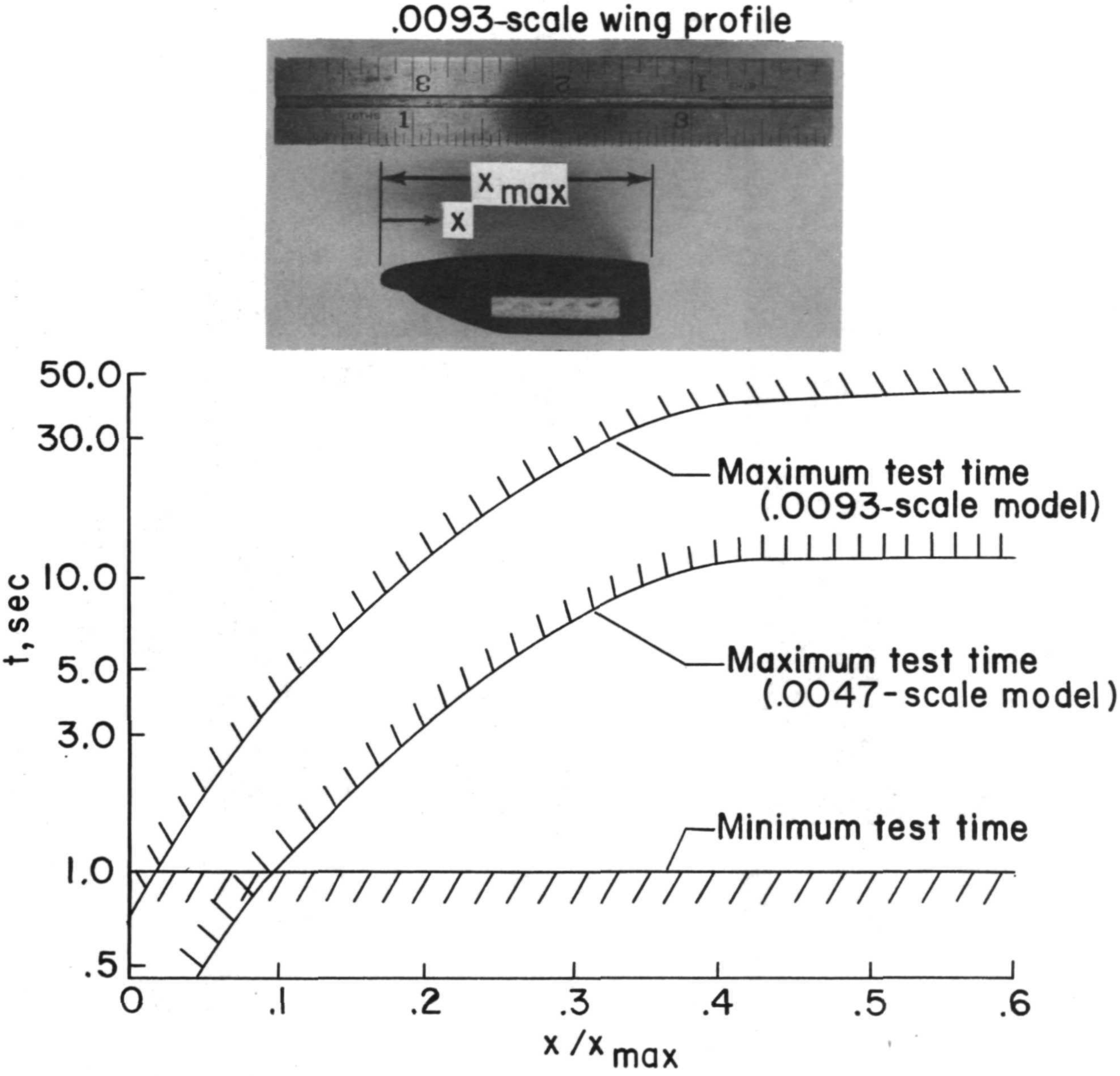

L-73-221

Figure 12.- Allowable test time.

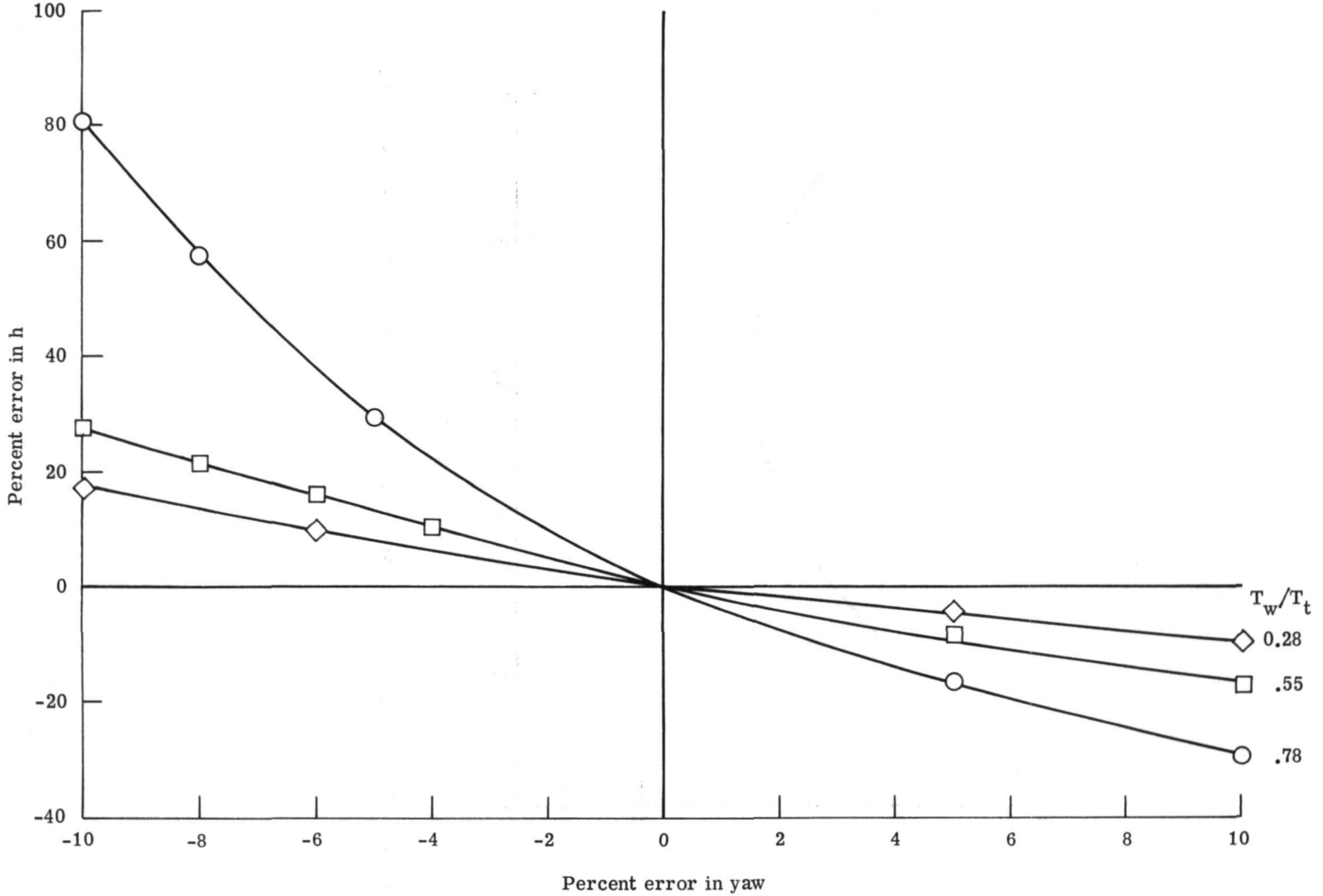

Figure 13.- Error in heat-transfer coefficient due to error in adiabatic wall temperature for three values of the wall-to-total temperature ratio.

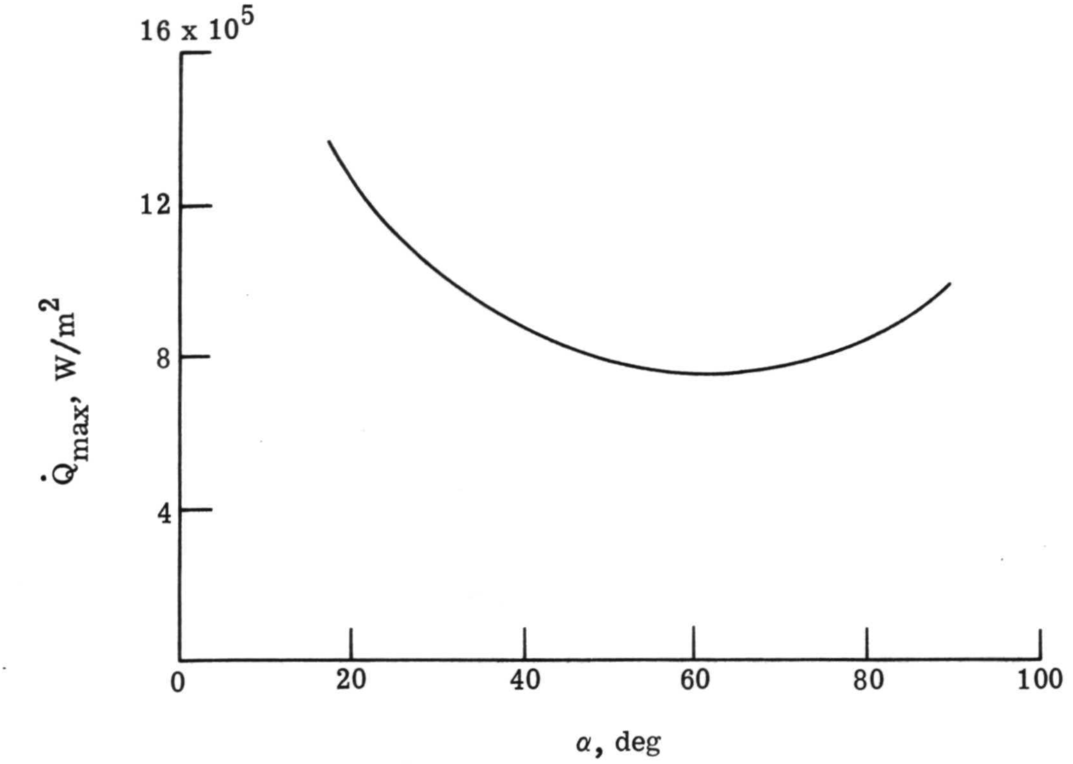

Figure 14.- Maximum sphere heating rate for constant angle-of-attack entry.

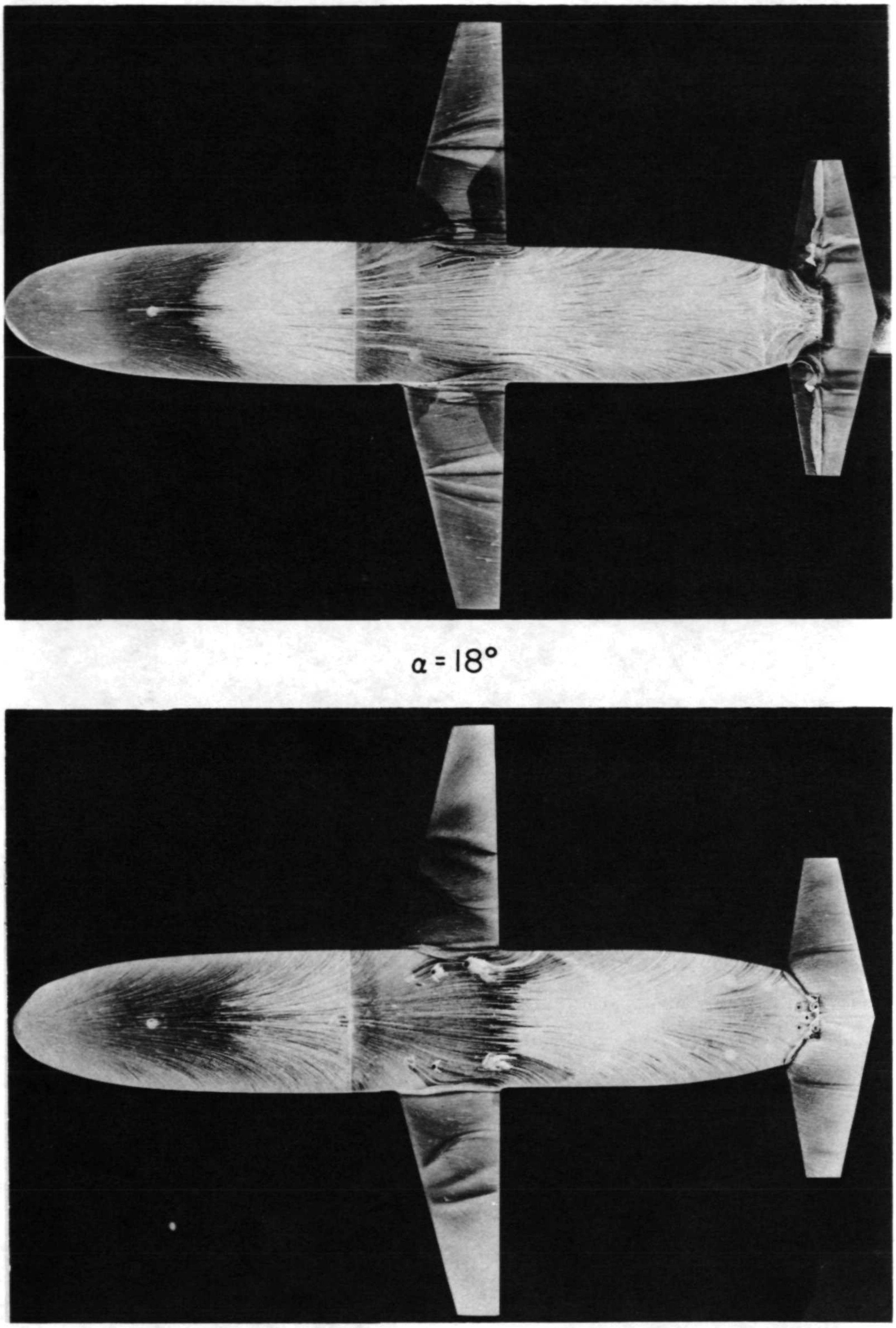

$\alpha = 18^\circ$

$\alpha = 50^\circ$

L-73-222

Figure 15.- Oil-flow patterns obtained on straight-wing orbiter at Mach 7.4 and angles of attack of 18° and 50°.

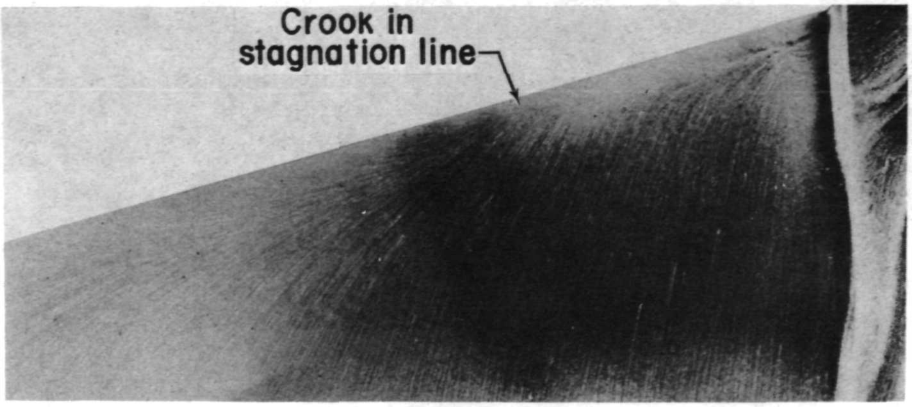

$M_1 \approx 7.4$; air (Ames)

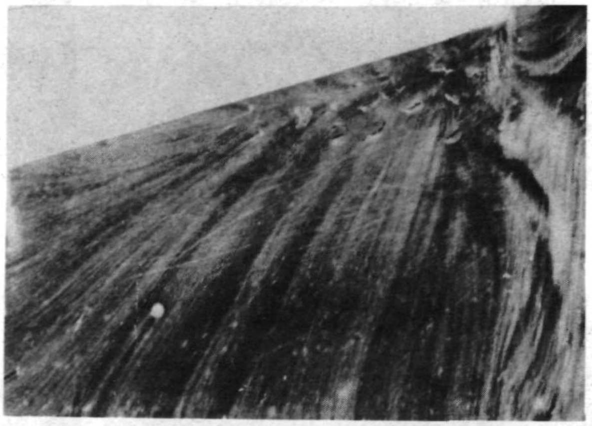

$M_1 \approx 8.0$; air

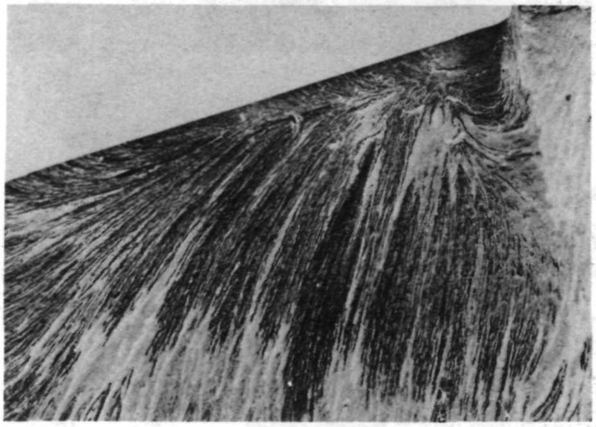

$M_1 \approx 20$; N_2

L-73-223

Figure 16.- Oil-flow patterns on complete and truncated wings at $\alpha = 60^{\circ}$.

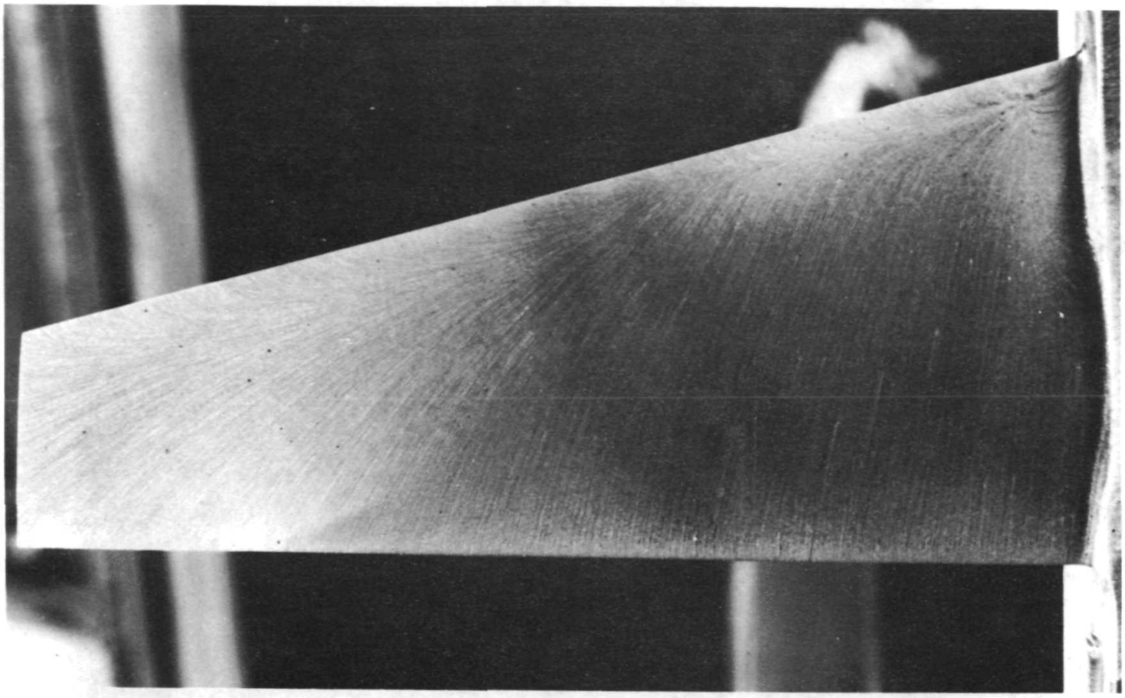

$\alpha = 60°$

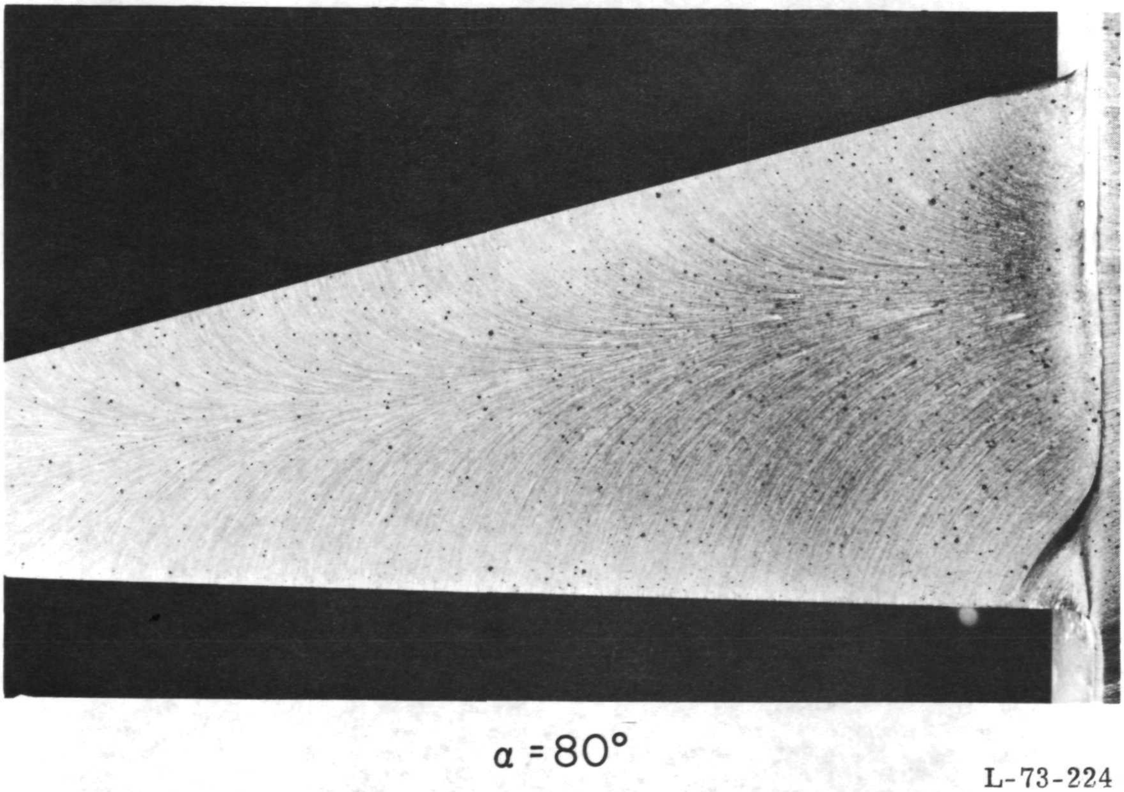

$\alpha = 80°$

L-73-224

Figure 17.- Oil-flow patterns obtained on straight-wing orbiter at Mach 7.4 at angles of attack of 60° and 80°. (Ames data.)

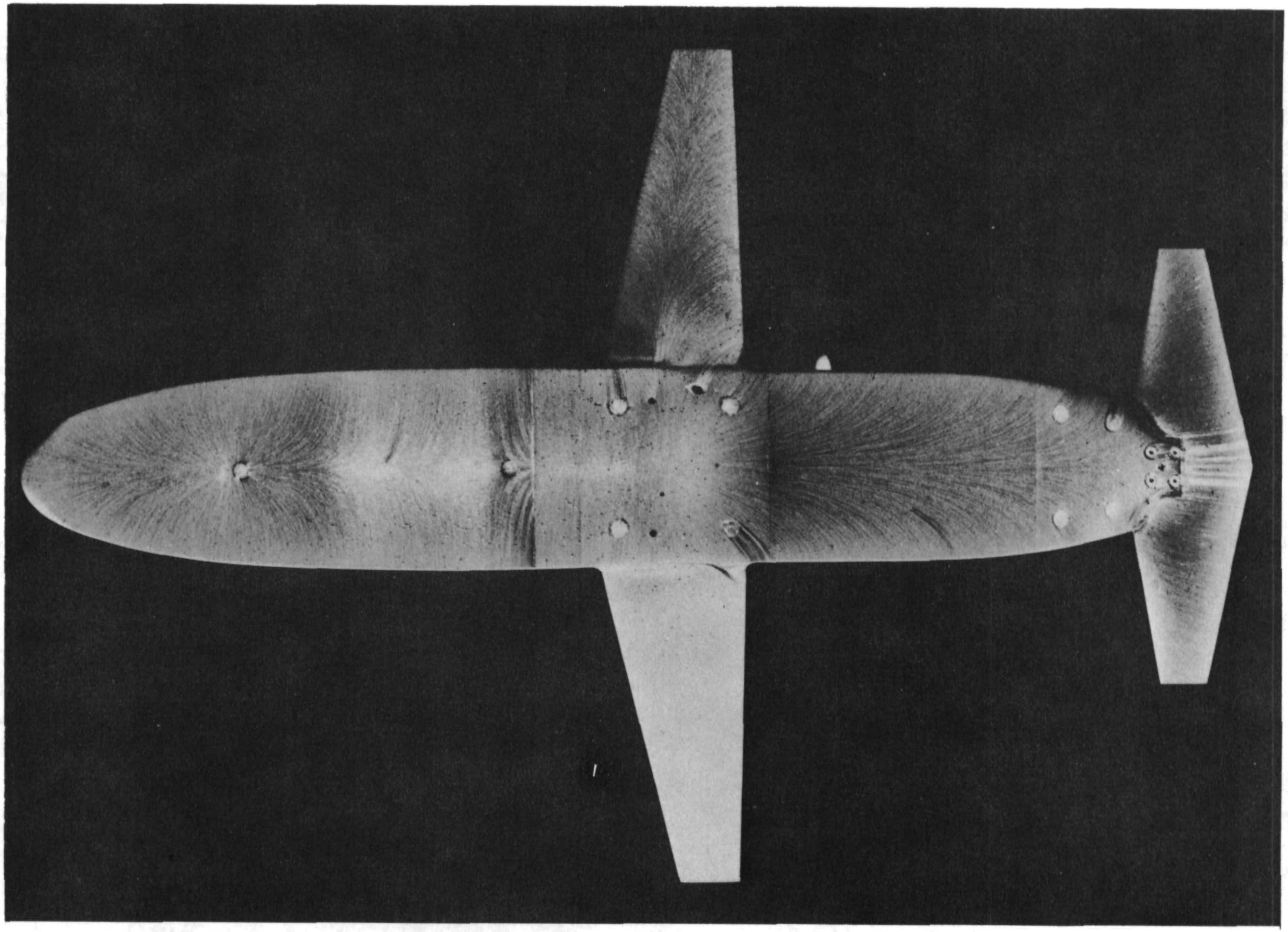

L-73-225

Figure 18.- Oil-flow patterns at $\alpha = 80^{\circ}$. (Ames data.)

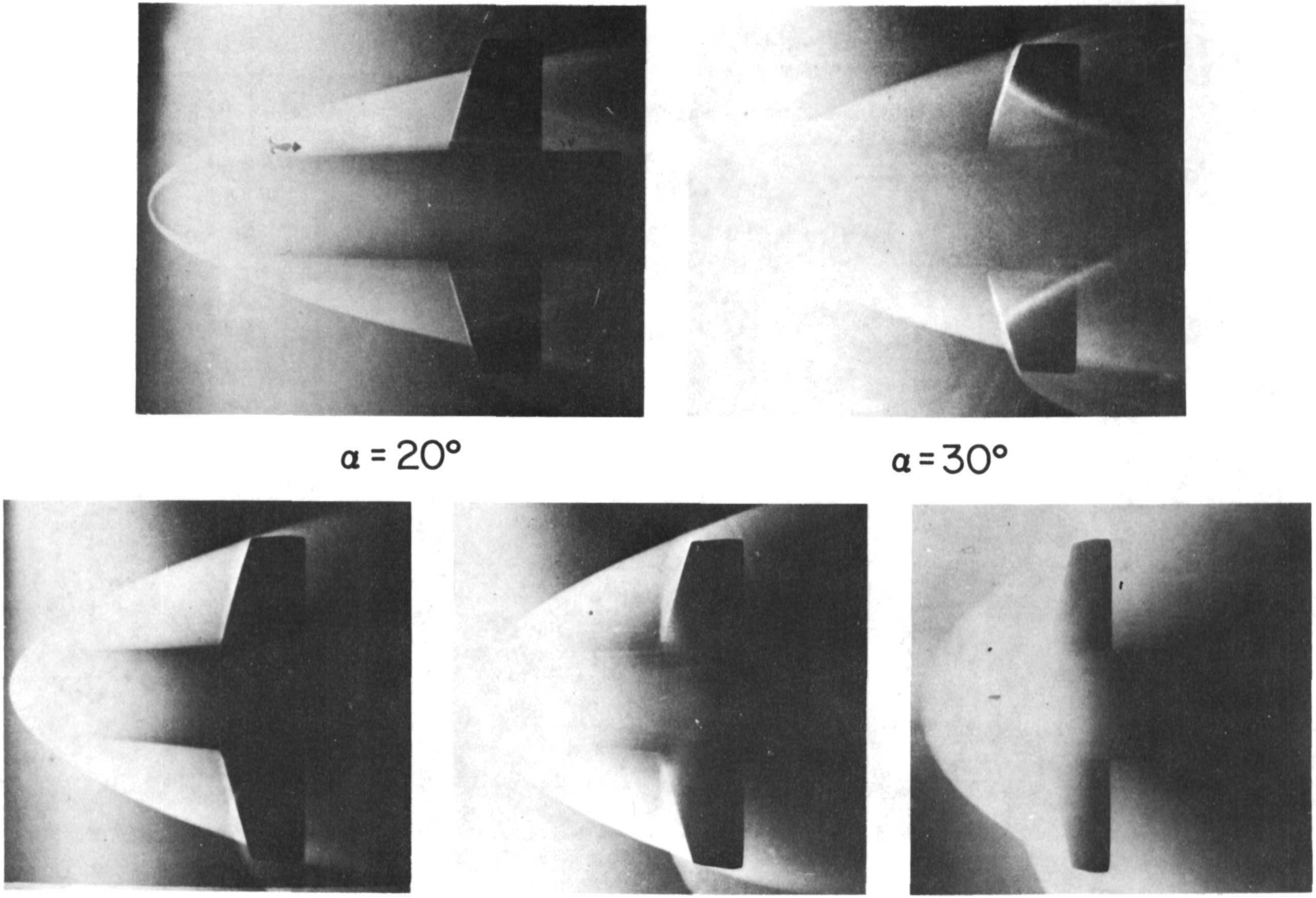

α = 20°

α = 30°

α = 40°

α = 50°

α = 60°

Figure 19.- Electron-beam photographs of truncated straight-wing orbiter in Langley 22-inch helium tunnel. $\rho_2/\rho_1 \approx 4.0$.

L-73-226

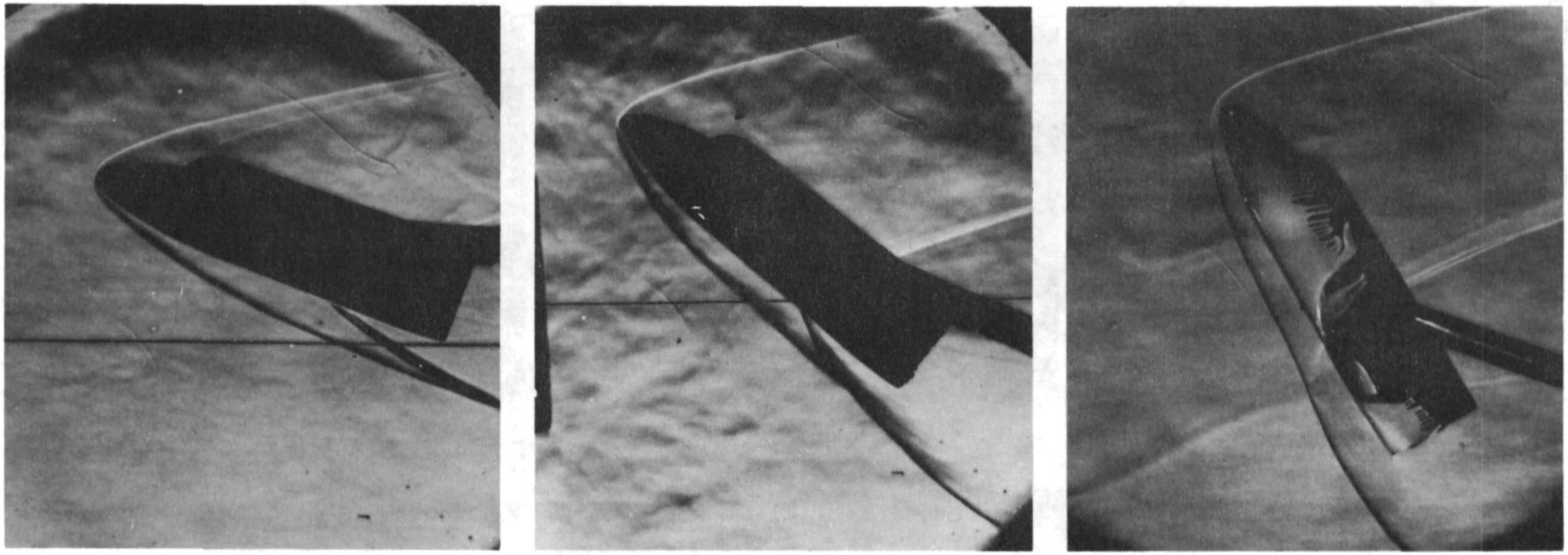

$\alpha = 20^0$ $\alpha = 40^0$ $\alpha = 60^0$

L-73-227

Figure 20.- Schlieren profiles for 0.0047-scale model of truncated straight-wing orbiter in air at Mach 8.

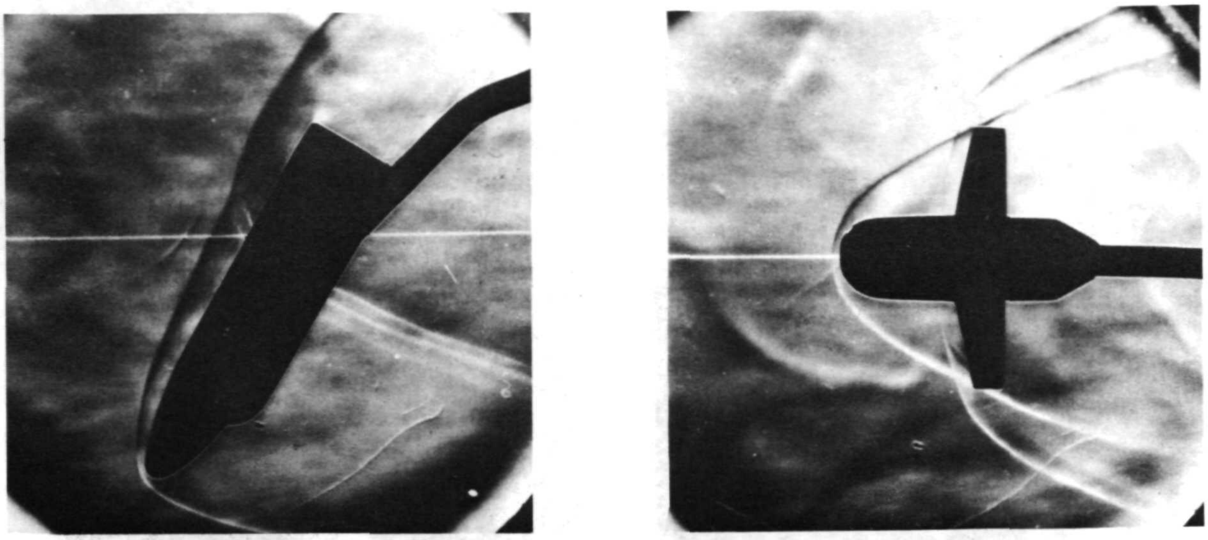

Air : $M_1 \approx 8$; $\gamma = 1.40$; $\rho_2/\rho_1 \approx 5.6$

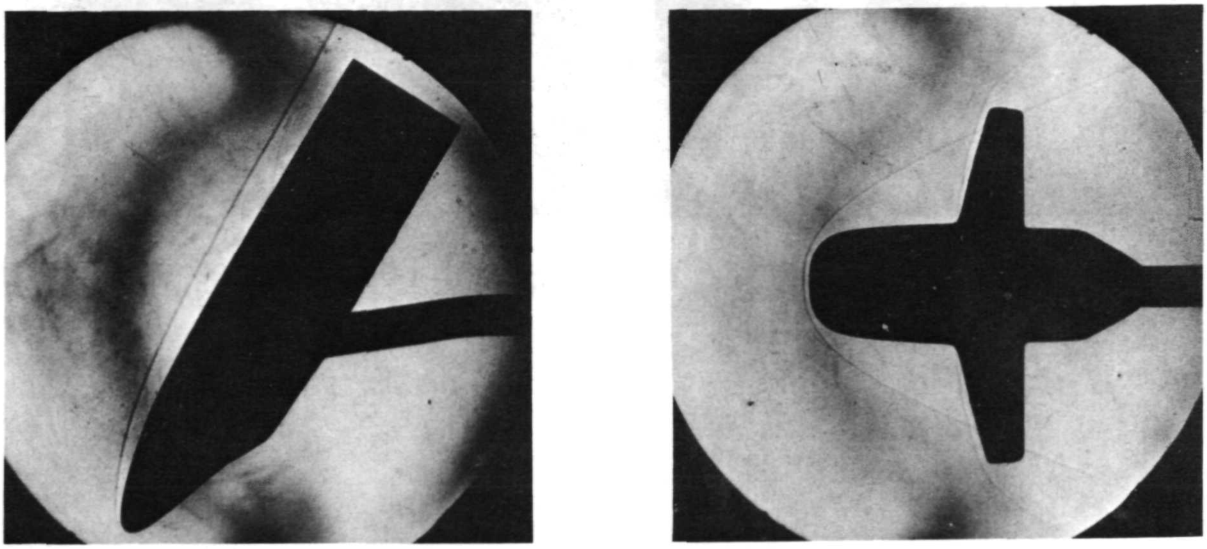

CF_4 : $M_1 \approx 6$; $\gamma \approx 1.12$; $\rho_2/\rho_1 \approx 12.1$

L-73-228

(a) Air and CF_4 (truncated model).

Figure 21.- Shock patterns on 0.0047-scale model of straight-wing orbiter in air and CF_4 at $\alpha = 60^{\circ}$.

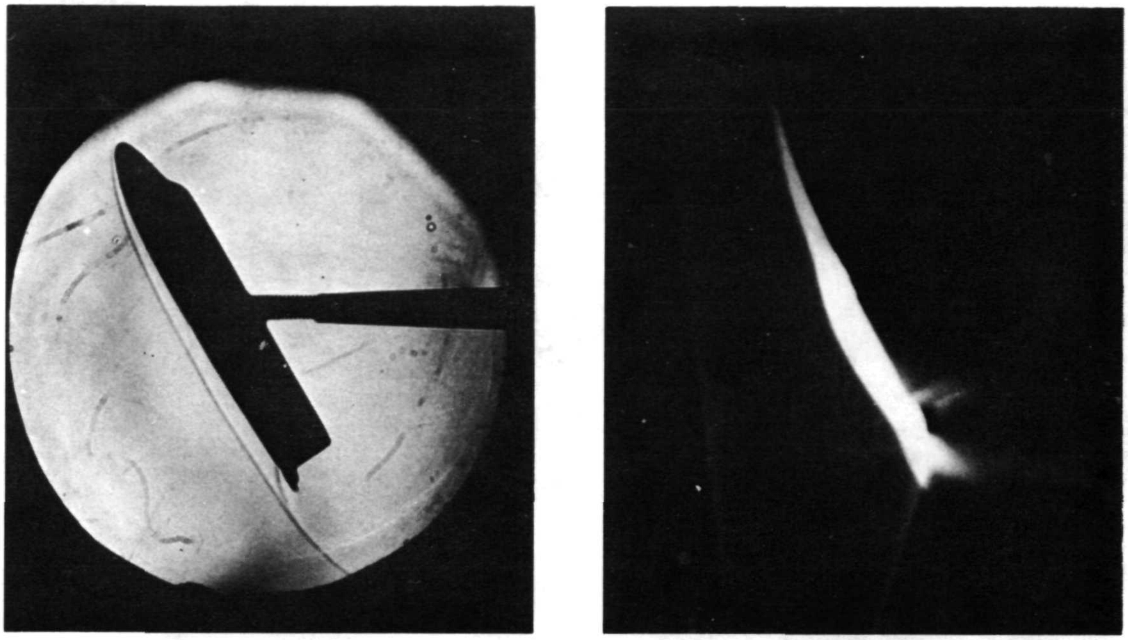

Shadowgraph in CF_4

$M_1 \approx 6$; $\rho_2/\rho_1 \approx 12.1$; $\Delta_{max}/D = 0.3$

Electron-beam photograph in nitrogen

$M_1 \approx 20$; $\rho_2/\rho_1 \approx 5.9$; $\Delta_{max}/D = 0.6$

L-73-229

(b) CF_4 and nitrogen (complete model).

Figure 21.- Concluded.

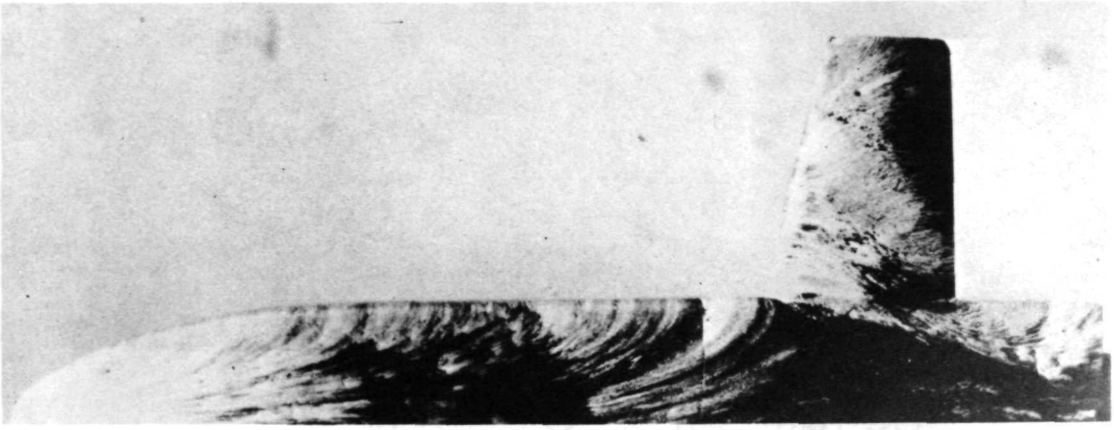

Helium : $M_1 \approx 20$; $\rho_2/\rho_1 \approx 4.0$

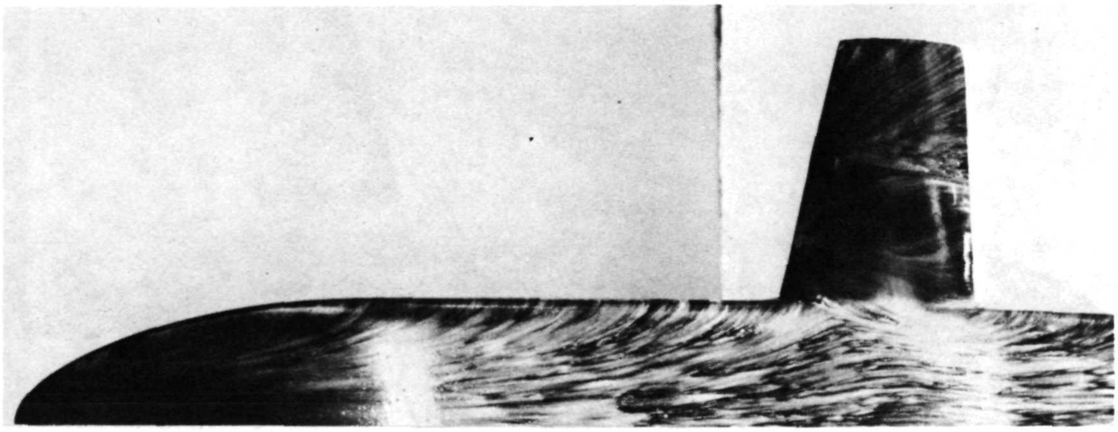

Nitrogen : $M_1 \approx 20$; $\rho_2/\rho_1 \approx 5.9$

L-73-230

Figure 22.- Oil-flow patterns on truncated straight-wing orbiter at $\alpha = 40^{\circ}$ and $M_1 \approx 20$.

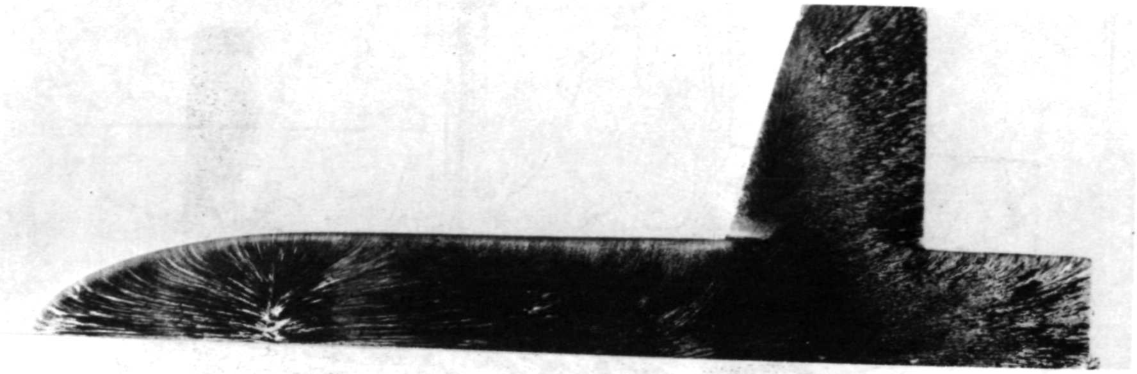

Helium : $M_1 \approx 20$; $\rho_2/\rho_1 \approx 4.0$

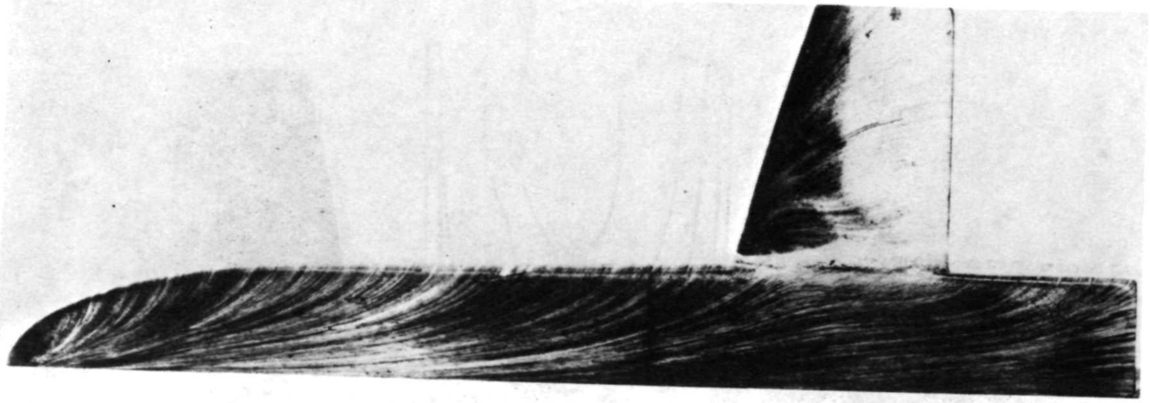

Nitrogen : $M_1 \approx 20$; $\rho_2/\rho_1 \approx 5.9$

L-73-231

Figure 23.- Oil-flow patterns on truncated straight-wing orbiter at $\alpha = 52^{\circ}$ and $M_1 \approx 20$.

Isotherm	$\frac{h}{h_{ref}}$	T_w, K
1	0.421	1860
2	.215	1572
3	.147	1429
4	.108	1324
5	.056	1125
6	.043	1052
7	.035	999
8	.030	961
9	.028	945
10	.025	918

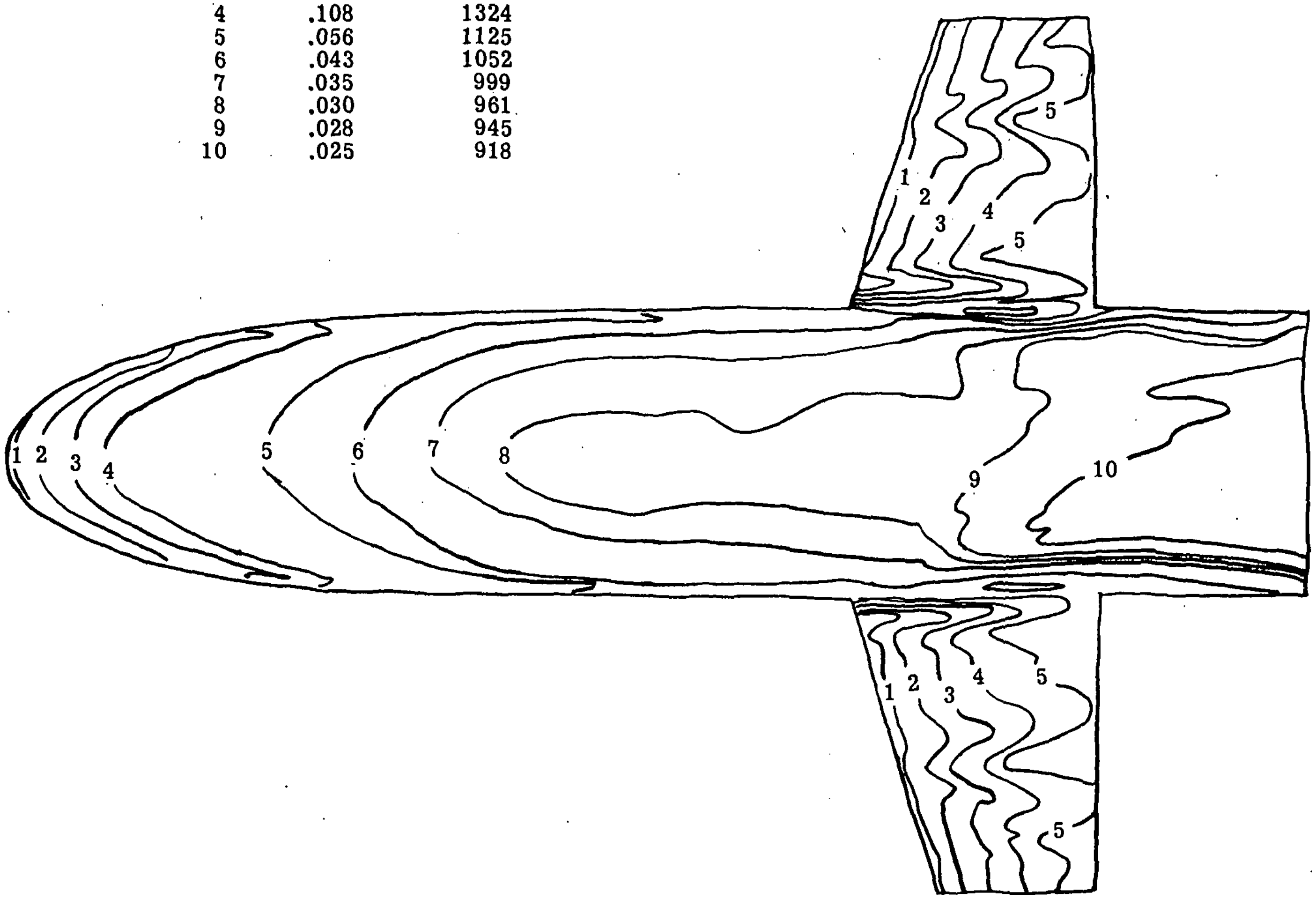

(a) $R_{\infty,l} = 0.81 \times 10^6$; 0.0047-scale model; $h_{ref} = 1.13 \times 10^3$ W/m^2-K; $\dot{Q}_{max} = 1.30 \times 10^6$ W/m^2.

Figure 24.- Heat-transfer-coefficient and skin-temperature contours for $M_1 \approx 8$ and $\alpha = 20^o$.

Isotherm	$\frac{h}{h_{ref}}$	T_w, K
1	1.184	2410
2	.593	2026
3	.393	1830
4	.129	1385
5	.089	1263
6	.069	1185
7	.053	1109
8	.047	1075
9	.042	1045
10	.037	1014
11	.032	977

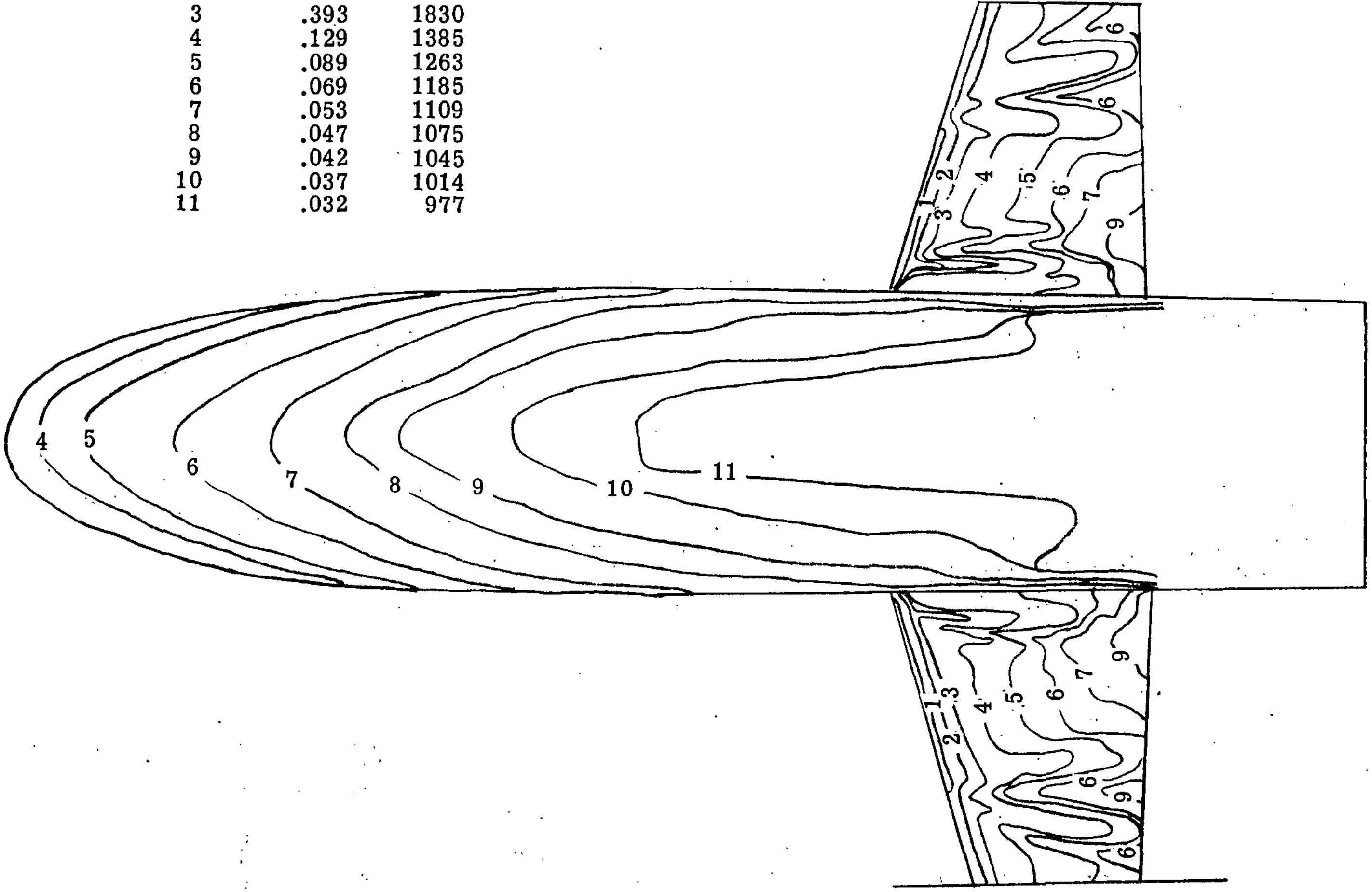

(b) $R_{\infty,l} = 1.45 \times 10^6$; 0.0093-scale model; $h_{ref} = 6.91 \times 10^2$ W/m^2-K; $\dot{Q}_{max} = 1.30 \times 10^6$ W/m^2.

Figure 24.- Continued.

Iso-therm	$\frac{h}{h_{ref}}$	T_w, K
1	0.499	1942
2	.317	1734
3	.224	1589
4	.131	1390
5	.085	1247
6	.066	1170
7	.050	1093
8	.033	985
9	.027	936
10	.023	899

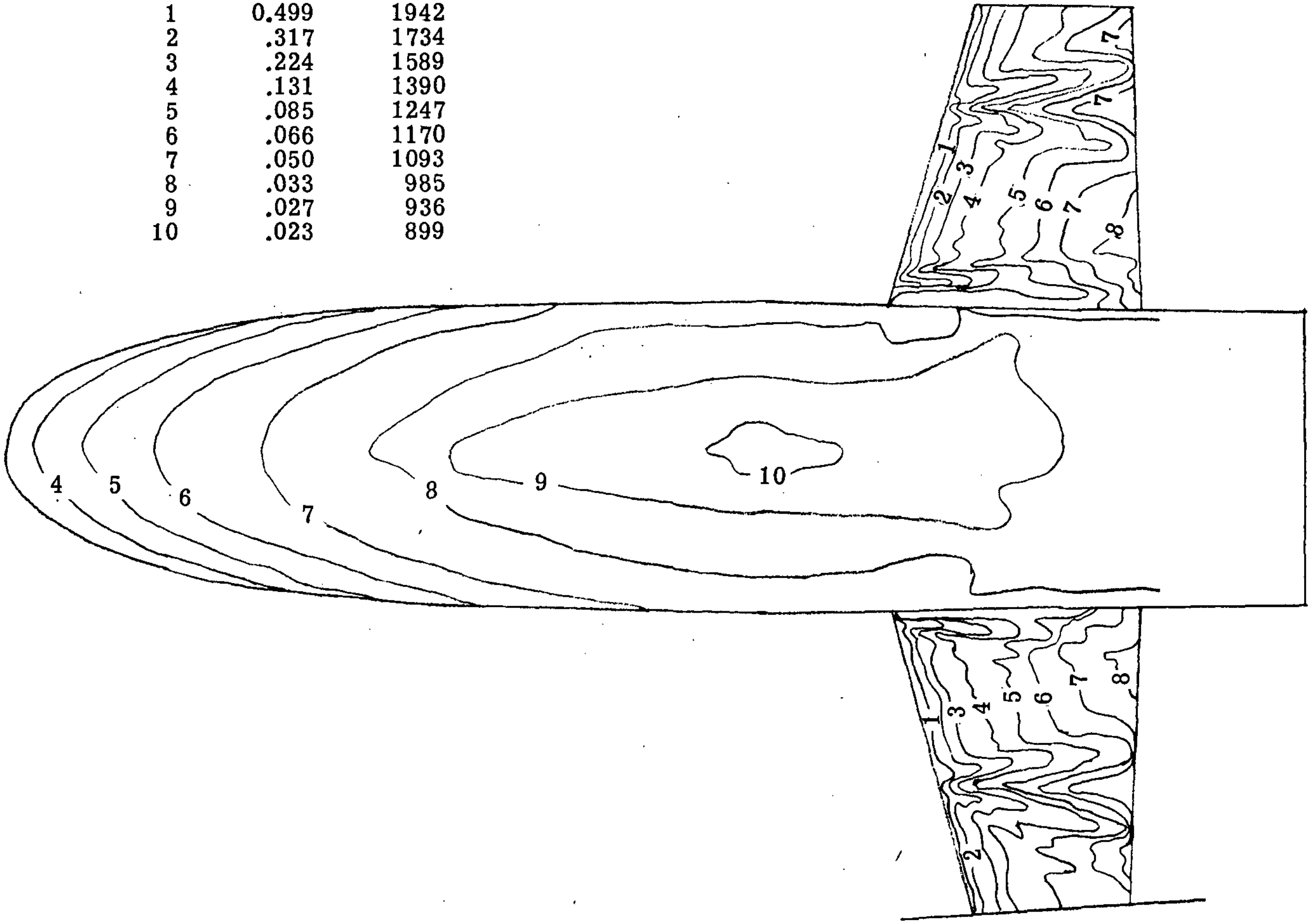

(c) $R_{\infty,l} = 3.39 \times 10^6$; 0.0093-scale model; $h_{ref} = 1.08 \times 10^3$ W/m^2-K; $\dot{Q}_{max} = 1.30 \times 10^6$ W/m^2.

Figure 24.- Continued.

Isotherm	$\frac{h}{h_{ref}}$	T_w, K
1	0.783	2172
2	.498	1941
3	.208	1559
4	.120	1359
5	.049	1086
6	.036	1006
7	.030	961
8	.028	946

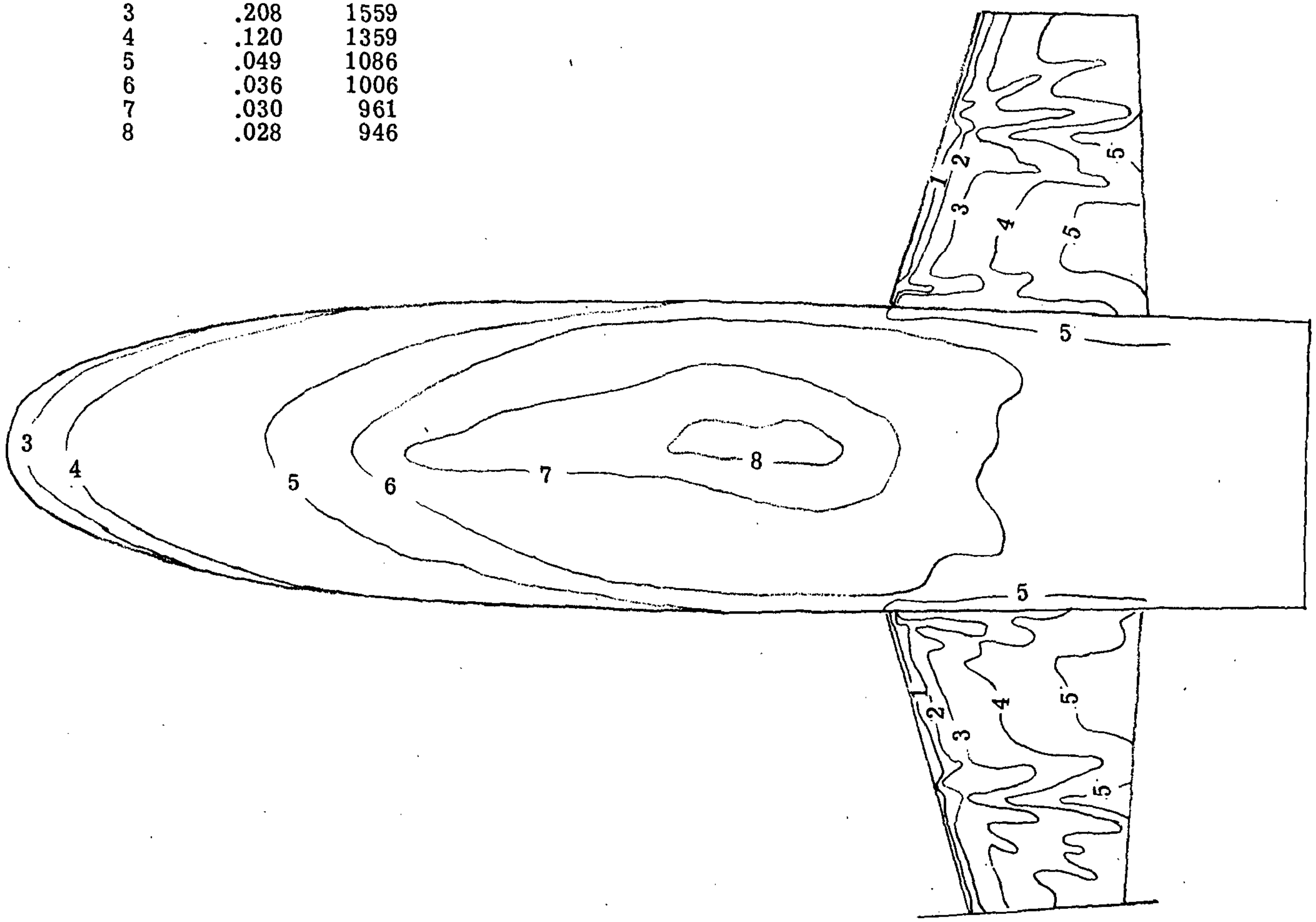

(d) $R_{\infty,l} = 6.28 \times 10^6$; 0.0093-scale model; $h_{ref} = 1.51 \times 10^3$ W/m^2-K; $\dot{Q}_{max} = 1.30 \times 10^6$ W/m^2.

Figure 24.- Concluded.

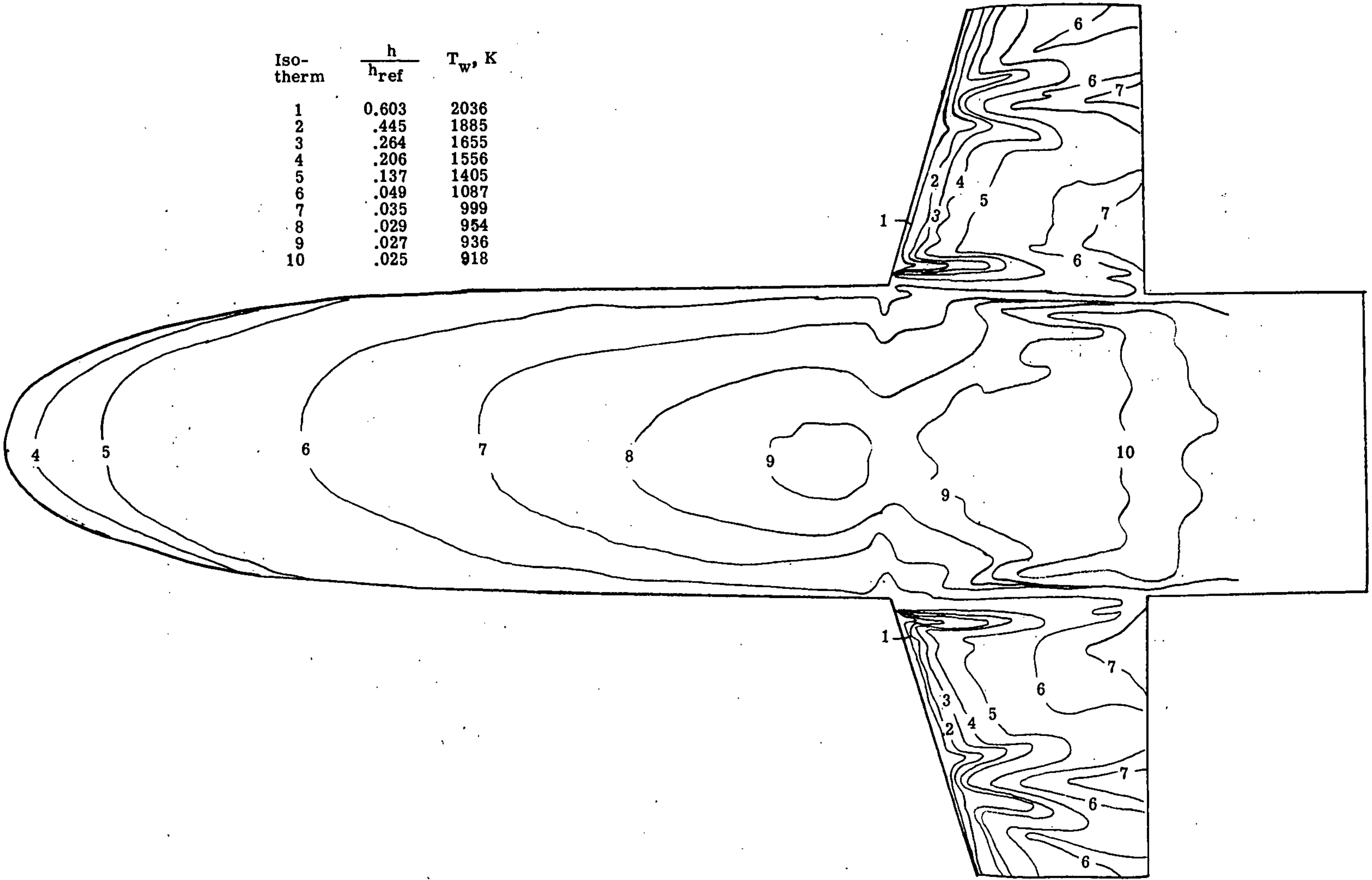

Iso-therm	$\frac{h}{h_{ref}}$	T_w, K
1	0.603	2036
2	.445	1885
3	.264	1655
4	.206	1556
5	.137	1405
6	.049	1087
7	.035	999
8	.029	954
9	.027	936
10	.025	918

Figure 25.- Heat-transfer-coefficient and skin-temperature contours on 0.0093-scale model at $\alpha = 20^{o}$ and $M_1 = 10.3$. $R_{\infty,l} = 1.80 \times 10^6$; $h_{ref} = 7.11 \times 10^2$ W/m2-K; $\dot{Q}_{max} = 1.30 \times 10^6$ W/m2.

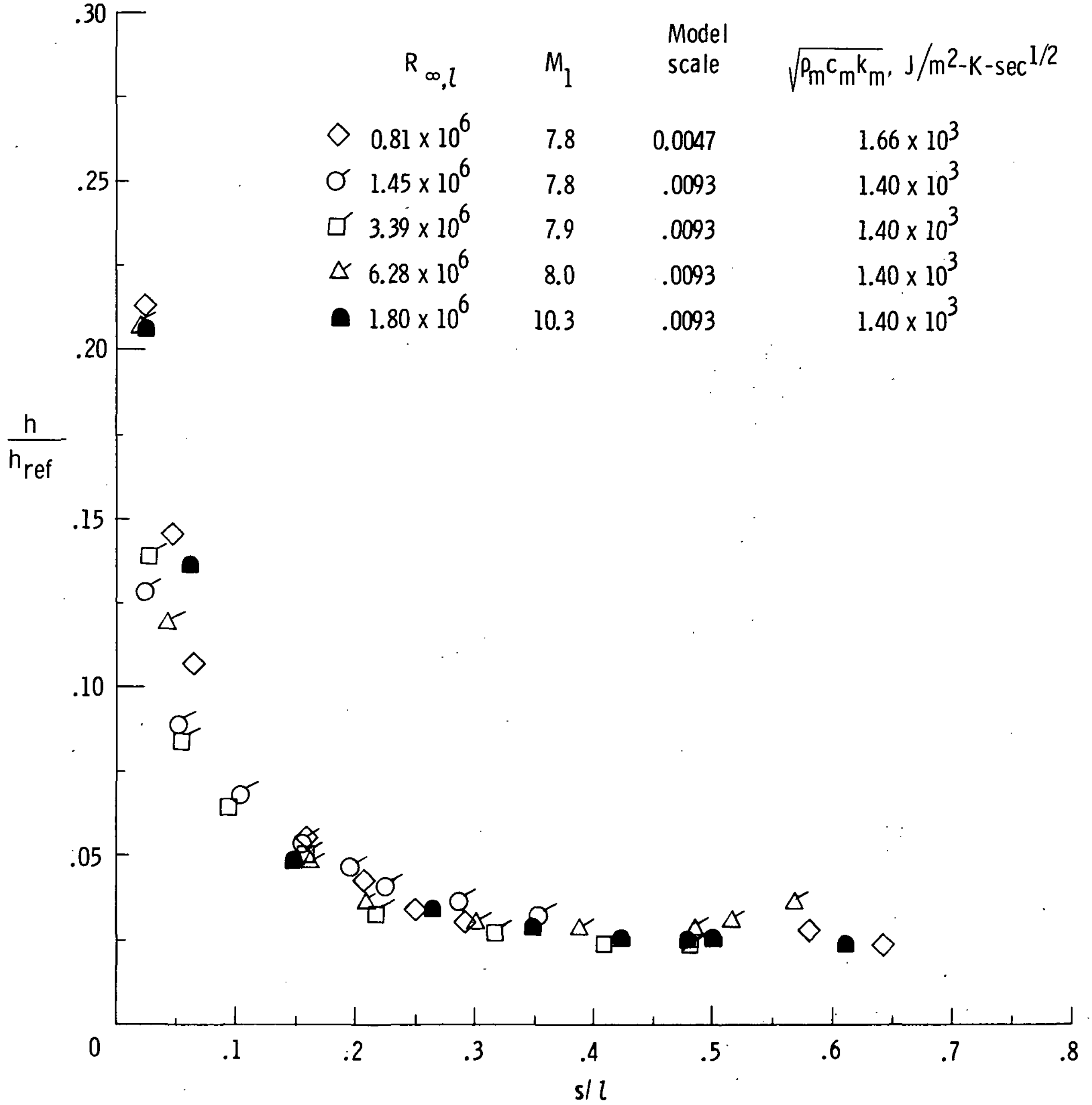

Figure 26.- Windward center-line heat-transfer-coefficient distributions at $\alpha = 20^{\circ}$.

Isotherm	$\frac{h}{h_{ref}}$	T_w, K
0	1.032	2108
1	.696	1909
2	.499	1756
3	.362	1620
4	.264	1498
5	.245	1470
6	.137	1270
7	.117	1222
8	.098	1169
9	.080	1111
10	.069	1071
11	.065	1055
12	.061	1038
13	.057	1021
14	.052	998

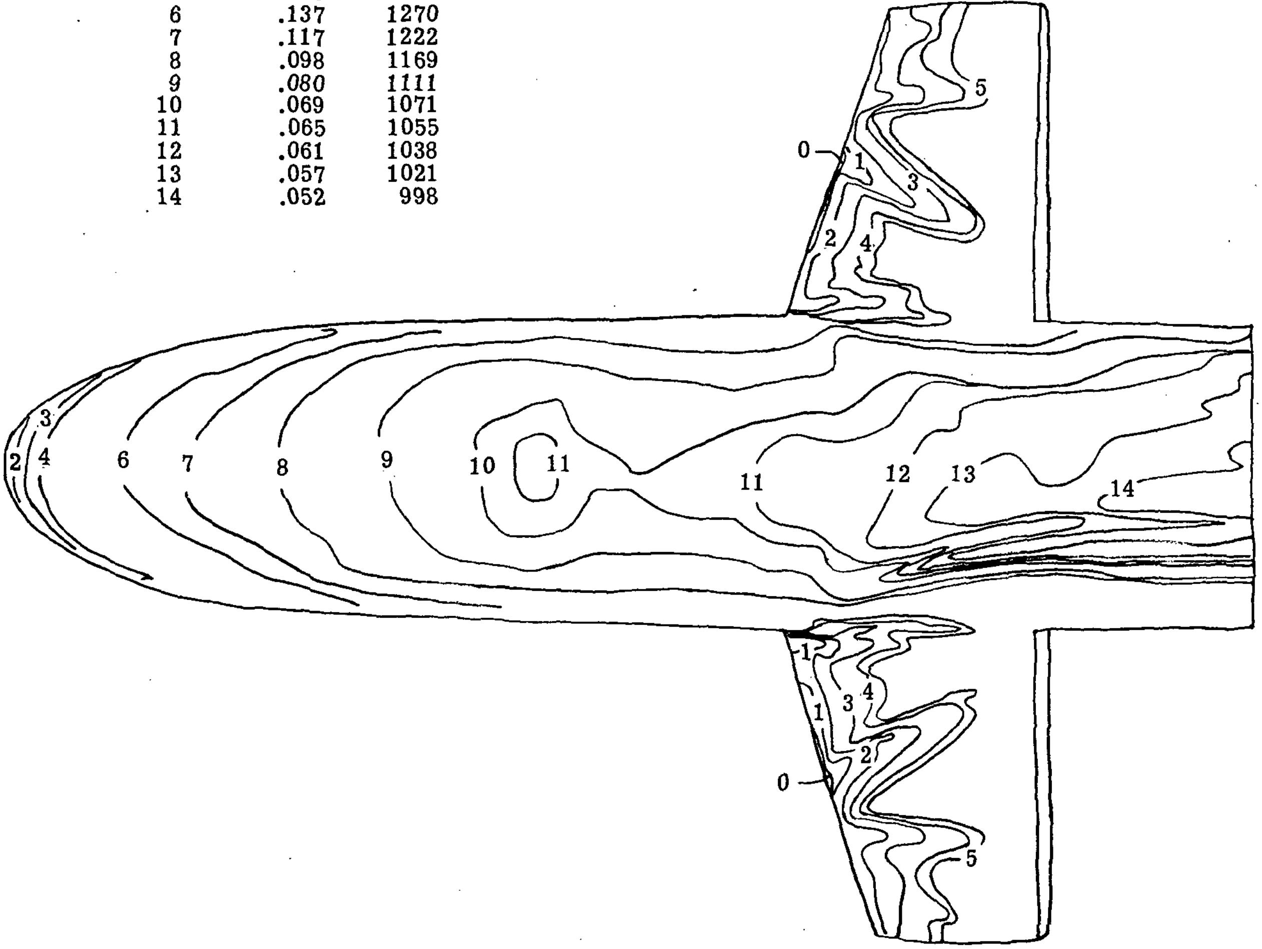

Figure 27.- Heat-transfer-coefficient and skin-temperature contours on 0.0047-scale model at $\alpha = 40^{\circ}$ and $M_1 \approx 8$. $R_{\infty,l} = 1.99 \times 10^6$; $h_{ref} = 1.71 \times 10^3$ W/m2-K; $\dot{Q}_{max} = 8.73 \times 10^5$ W/m2.

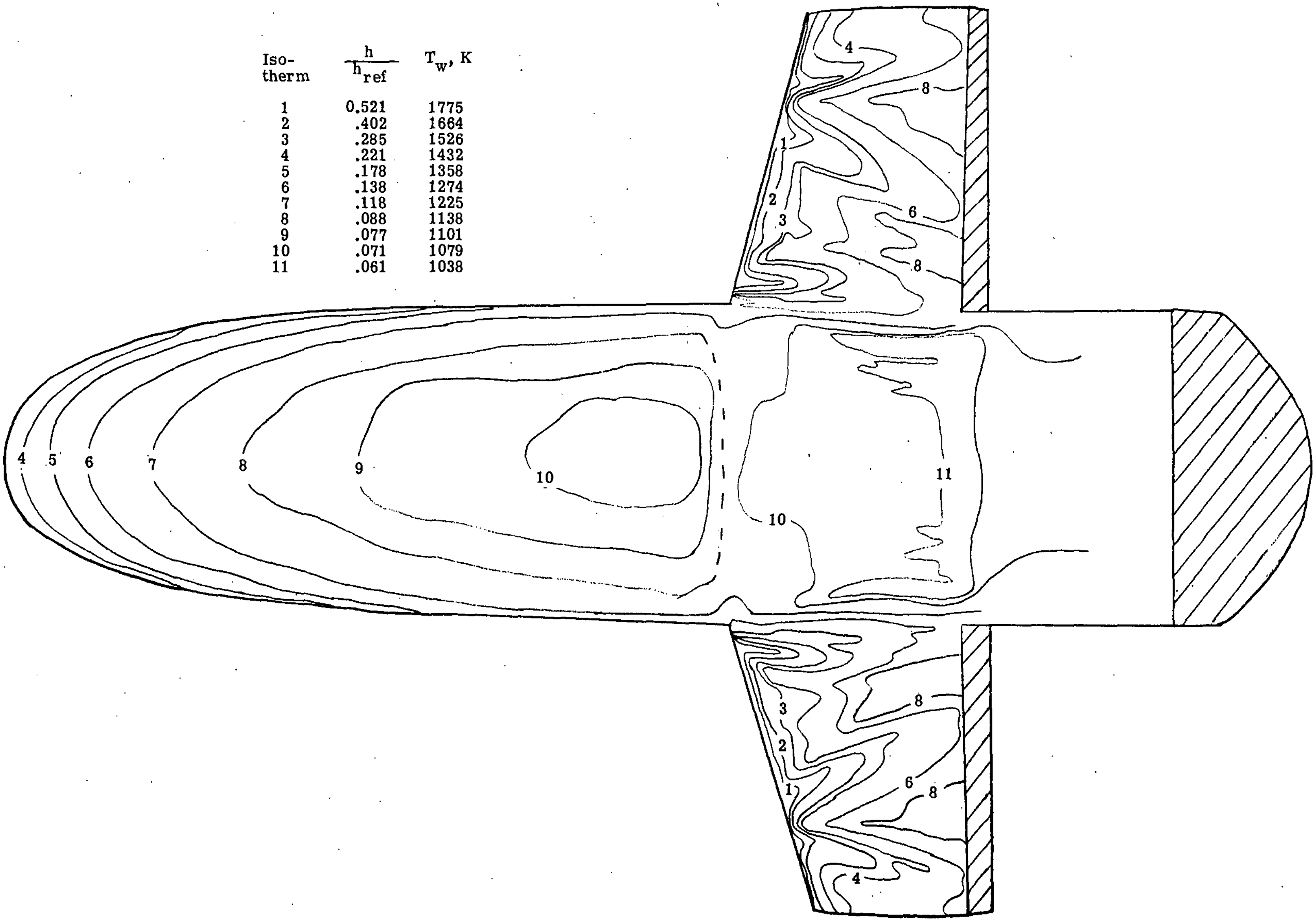

Isotherm	$\frac{h}{h_{ref}}$	T_w, K
1	0.521	1775
2	.402	1664
3	.285	1526
4	.221	1432
5	.178	1358
6	.138	1274
7	.118	1225
8	.088	1138
9	.077	1101
10	.071	1079
11	.061	1038

Figure 28.- Heat-transfer-coefficient and skin-temperature contours on 0.0093-scale model at $\alpha = 40^{\circ}$ and $M_1 = 10.3$. $R_{\infty,l} = 1.80 \times 10^6$; $h_{ref} = 7.05 \times 10^2$ W/m^2-K; $\dot{Q}_{max} = 8.73 \times 10^5$ W/m^2.

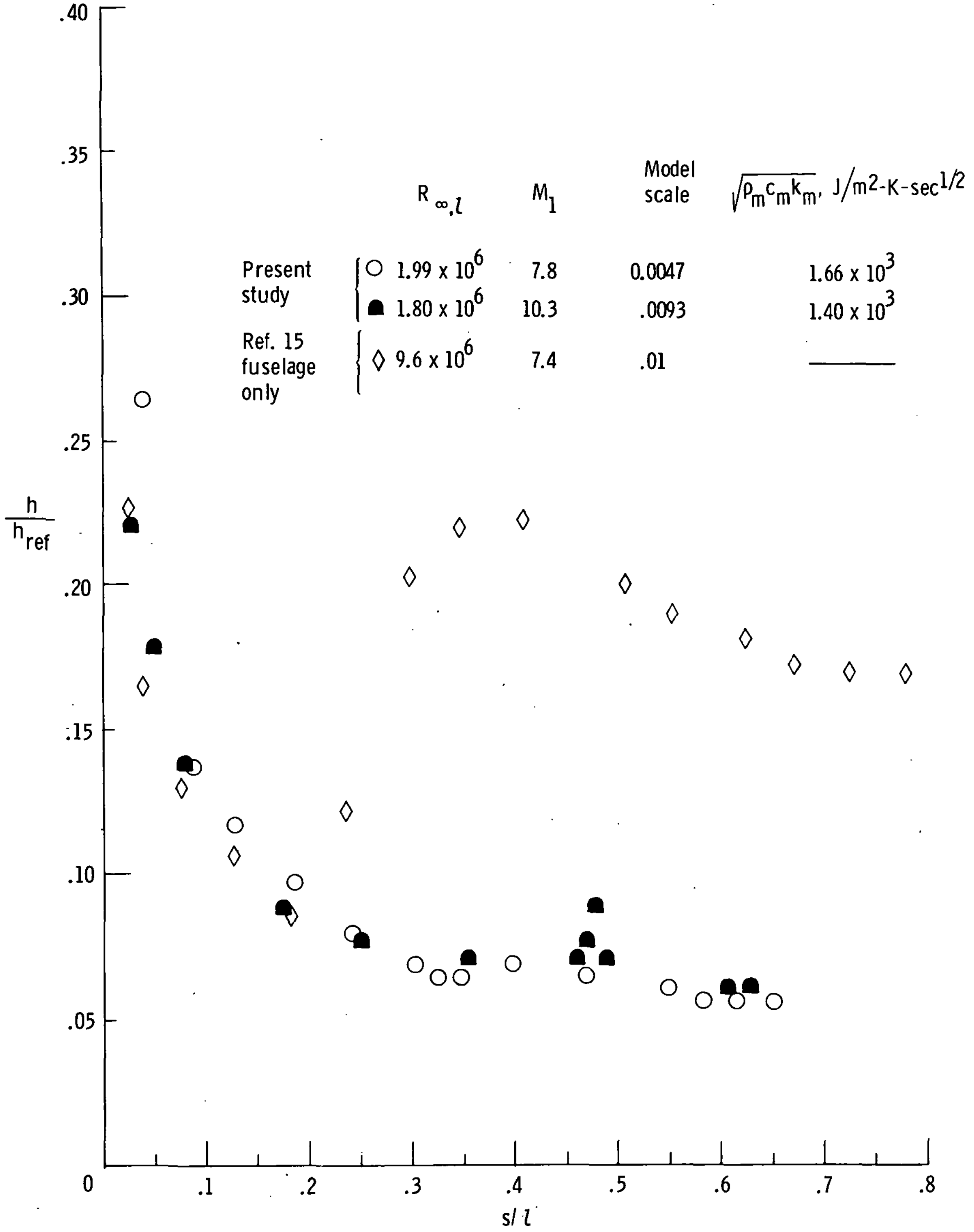

Figure 29.- Windward center-line heat-transfer-coefficient distributions at $\alpha = 40^{\circ}$.

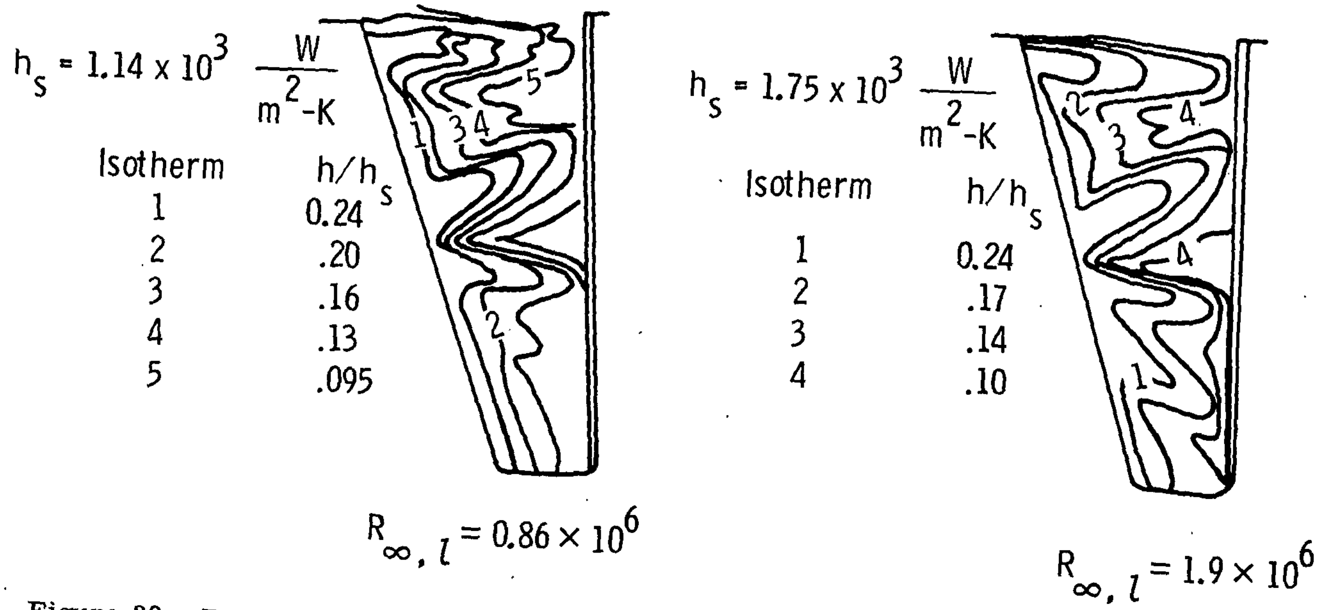

Figure 30.- Reynolds number influence on shear-layer impingement on wing at $\alpha = 40^{\circ}$. $M_1 \approx 8$; $\rho_2/\rho_1 \approx 5.6$.

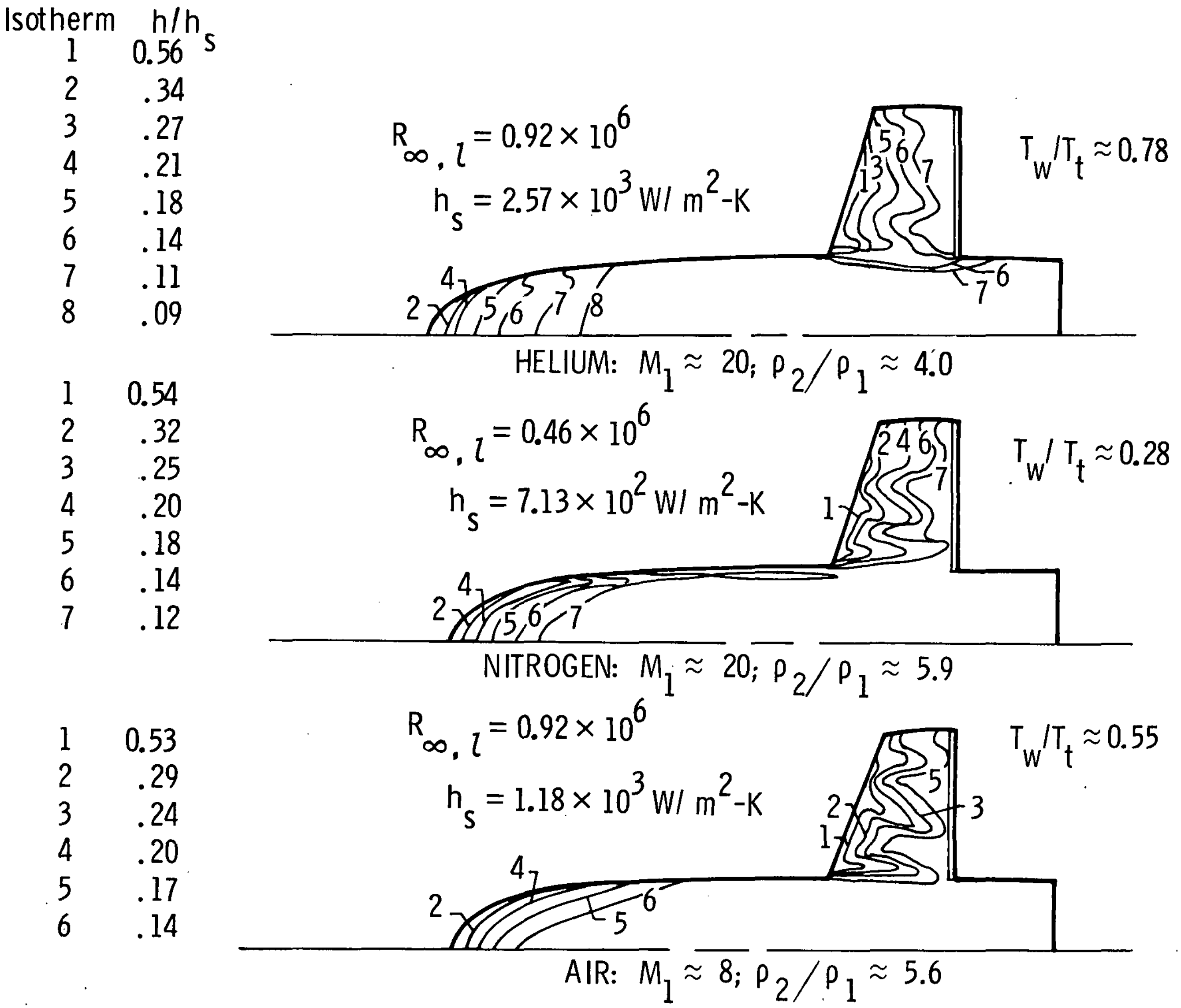

Figure 31.- Heat-transfer-coefficient contours at $\alpha = 40^{\circ}$.

Isotherm	$\frac{h}{h_{ref}}$	T_w, K
1	0.225	1405
2	.176	1321
3	.157	1285
4	.127	1218
5	.108	1170
6	.098	1142
7	.095	1132
8	.088	1111

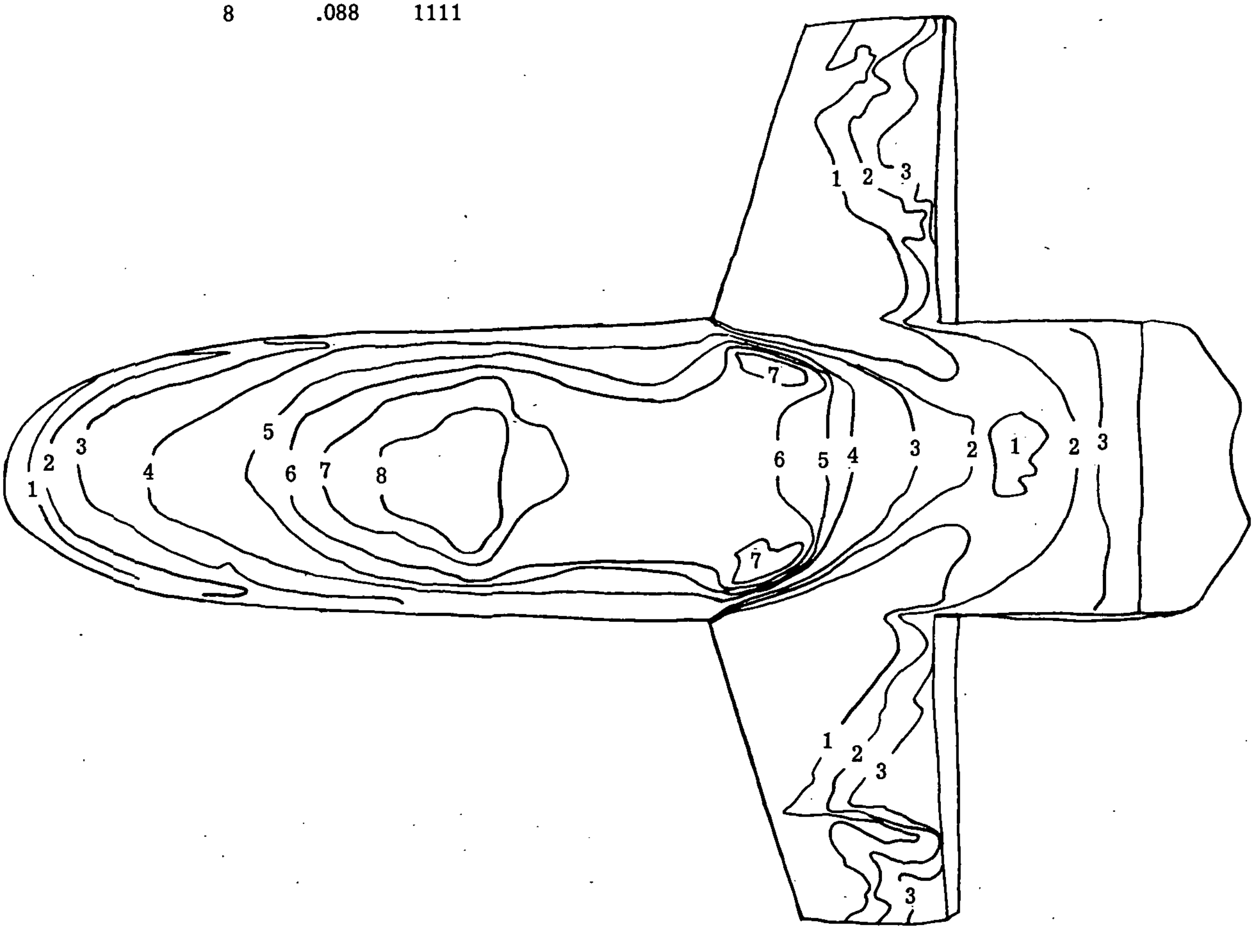

Figure 32.- Heat-transfer-coefficient and skin-temperature contours on 0.0047-scale model at $\alpha = 50^o$ and $M_1 \approx 8$. $R_{\infty,l} = 4.33 \times 10^6$; $h_{ref} = 2.55 \times 10^3$ W/m^2-K; $\dot{Q}_{max} = 7.94 \times 10^5$ W/m^2.

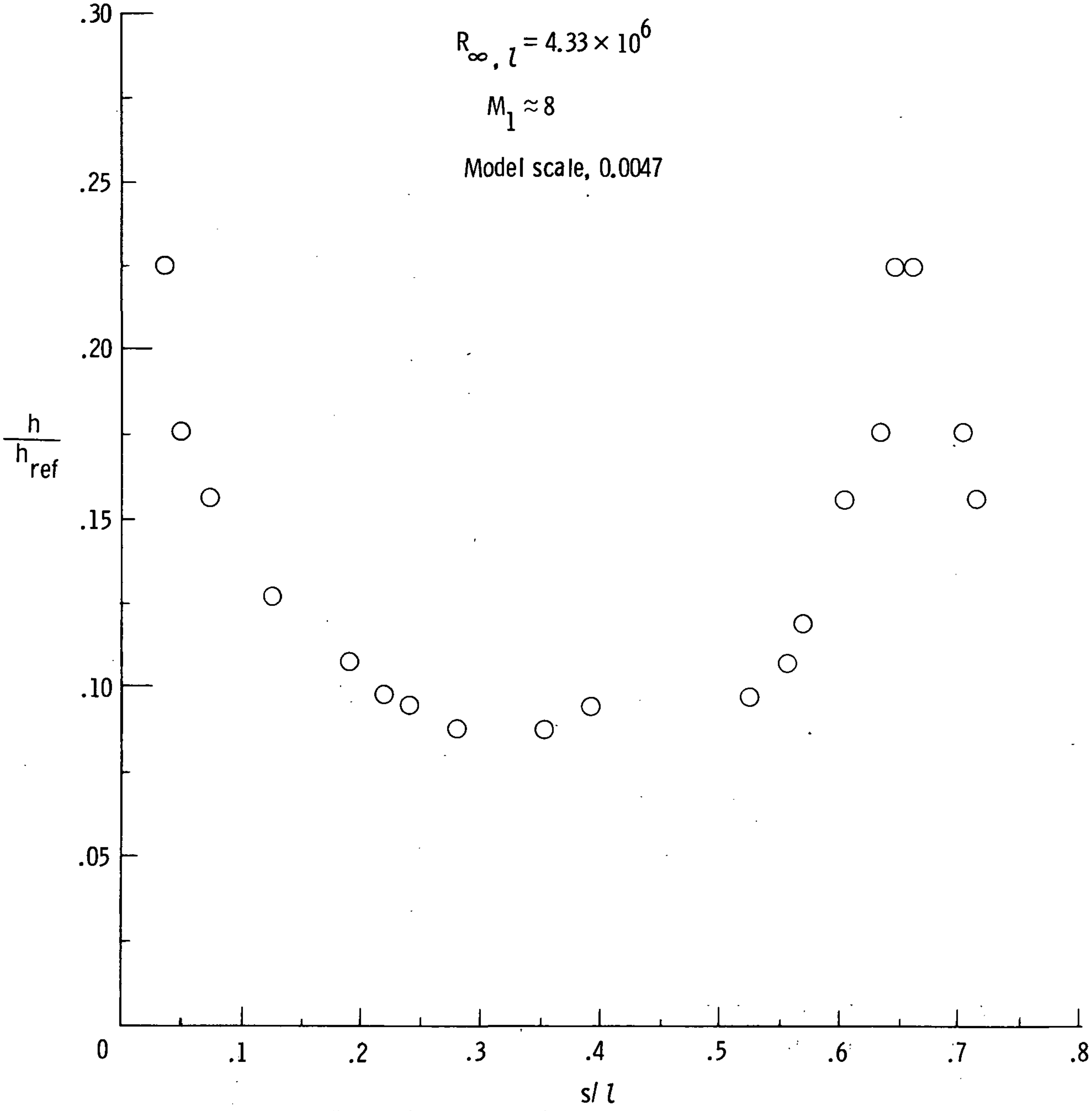

Figure 33.- Windward center-line heat-transfer-coefficient distribution at $\alpha = 50^{\circ}$.

Isotherm	$\frac{h}{h_{ref}}$
1	0.28
2	.23
3	.17
4	.14
5	.11
6	.094

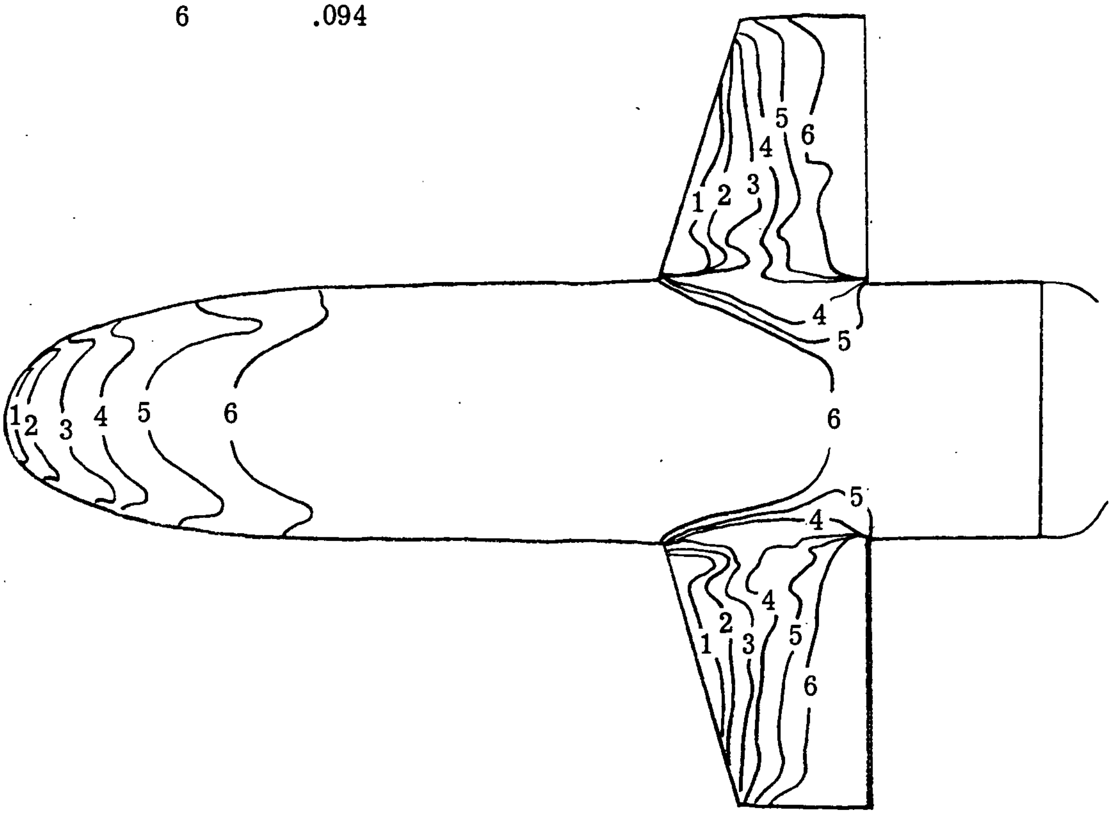

Figure 34.- Heat-transfer-coefficient contours on 0.0047-scale model in helium at $\alpha = 50^\circ$ and $M_1 = 20.3$. $R_{\infty,l} = 1.93 \times 10^6$; $h_{ref} = 3.60 \times 10^3$ W/m^2-K.

Iso-therm	$\frac{h}{h_{ref}}$	T_w, K
1		
2	0.232	1406
3	.190	1336
4	.164	1289
5	.147	1253
6	.134	1225
7	.116	1181
8	.106	1155
9	.099	1136
10	.096	1127

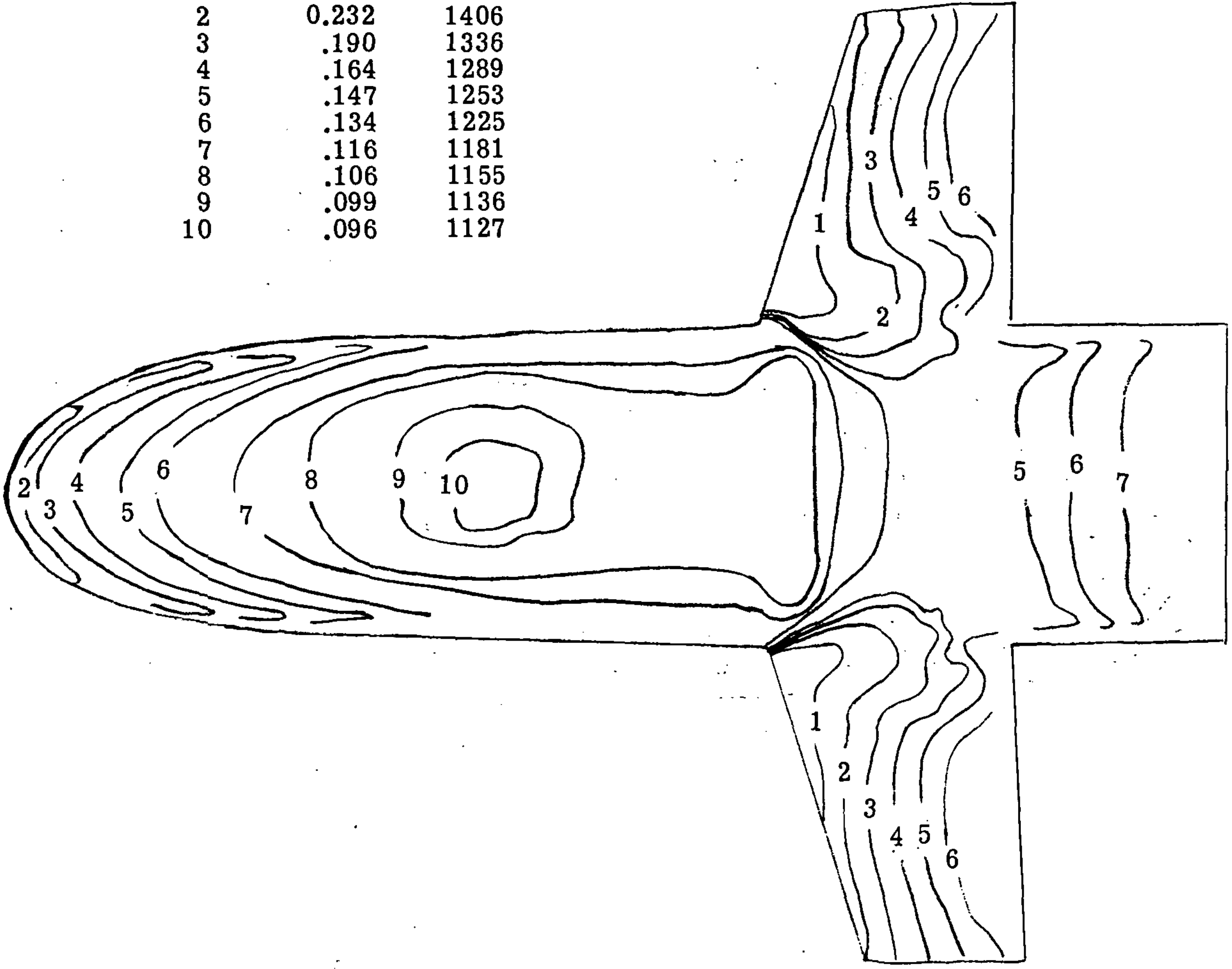

(a) $R_{\infty,l} = 2.1 \times 10^6$; $h_{ref} = 1.71 \times 10^3$ W/m^2-K; $\dot{Q}_{max} = 7.71 \times 10^5$ W/m^2.

Figure 35.- Heat-transfer-coefficient and skin-temperature contours on 0.0047-scale model at $\alpha = 60^o$ and $M_1 \approx 8$ in air.

Isotherm	$\frac{h}{h_{ref}}$	T_w, K
1	0.205	1364
2	.179	1318
3	.149	1259
4	.126	1207
5	.107	1159
6	.102	1145

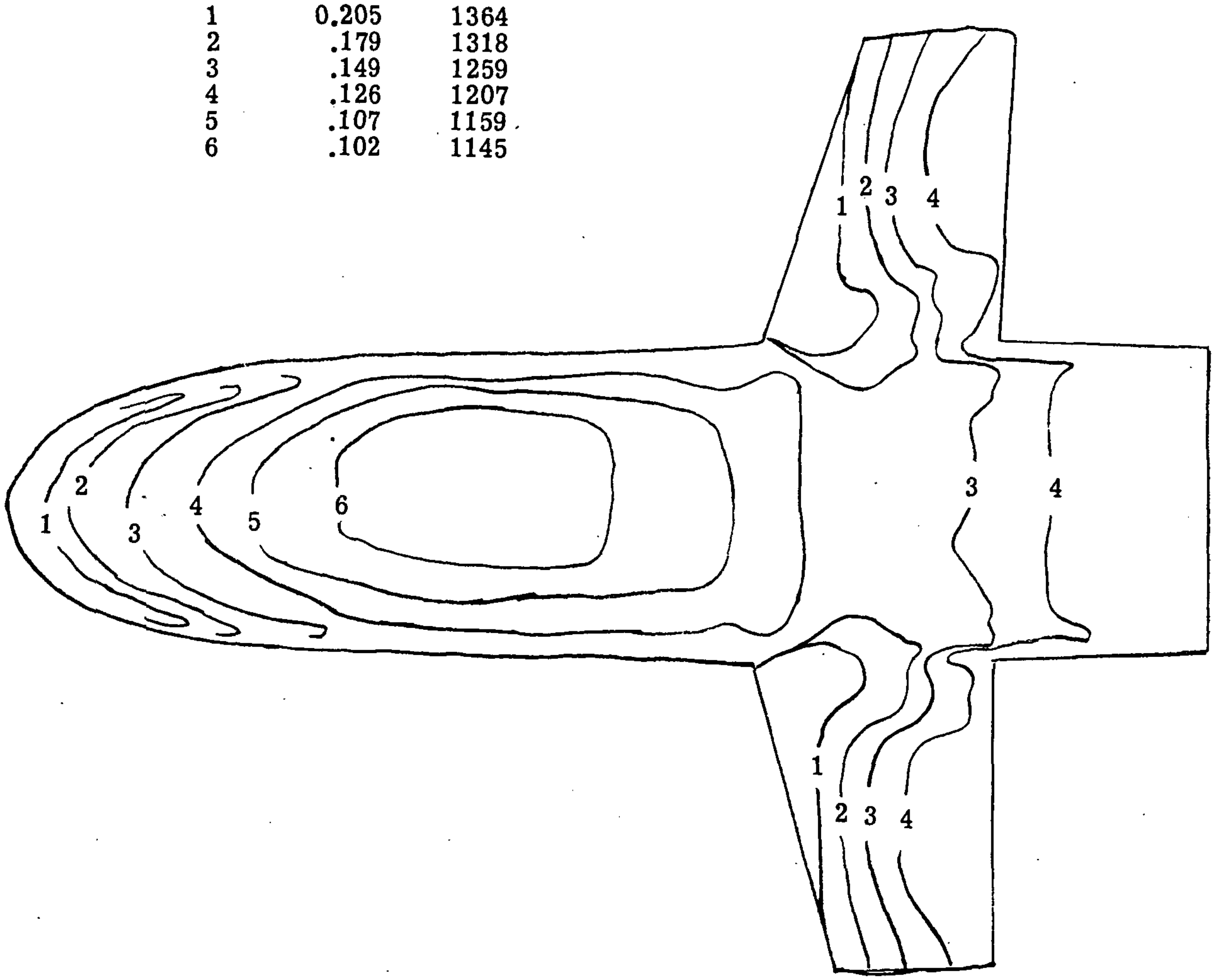

(b) $R_{\infty,l} = 2.9 \times 10^6$; $h_{ref} = 2.09 \times 10^3$ W/m^2-K; $\dot{Q}_{max} = 7.71 \times 10^5$ W/m^2.

Figure 35.- Concluded.

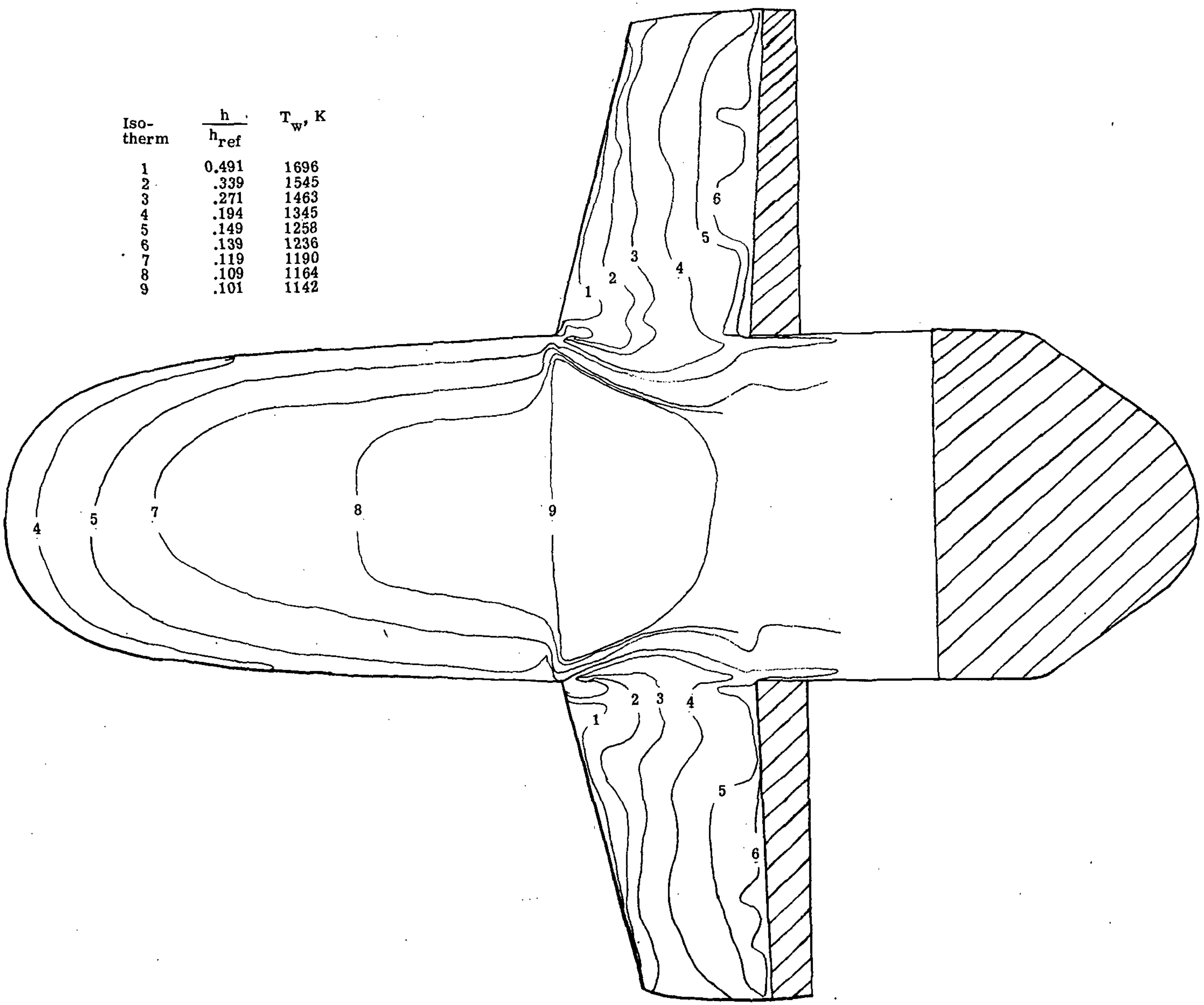

Isotherm	$\frac{h}{h_{ref}}$	T_w, K
1	0.491	1696
2	.339	1545
3	.271	1463
4	.194	1345
5	.149	1258
6	.139	1236
7	.119	1190
8	.109	1164
9	.101	1142

Figure 36.- Heat-transfer-coefficient and skin-temperature contours on 0.0093-scale model at $\alpha = 60^{o}$ and $M_1 = 10.3$. $R_{\infty,l} = 1.80 \times 10^6$; $h_{ref} = 7.05 \times 10^2$ W/m^2-K; $\dot{Q}_{max} = 7.71 \times 10^5$ W/m^2.

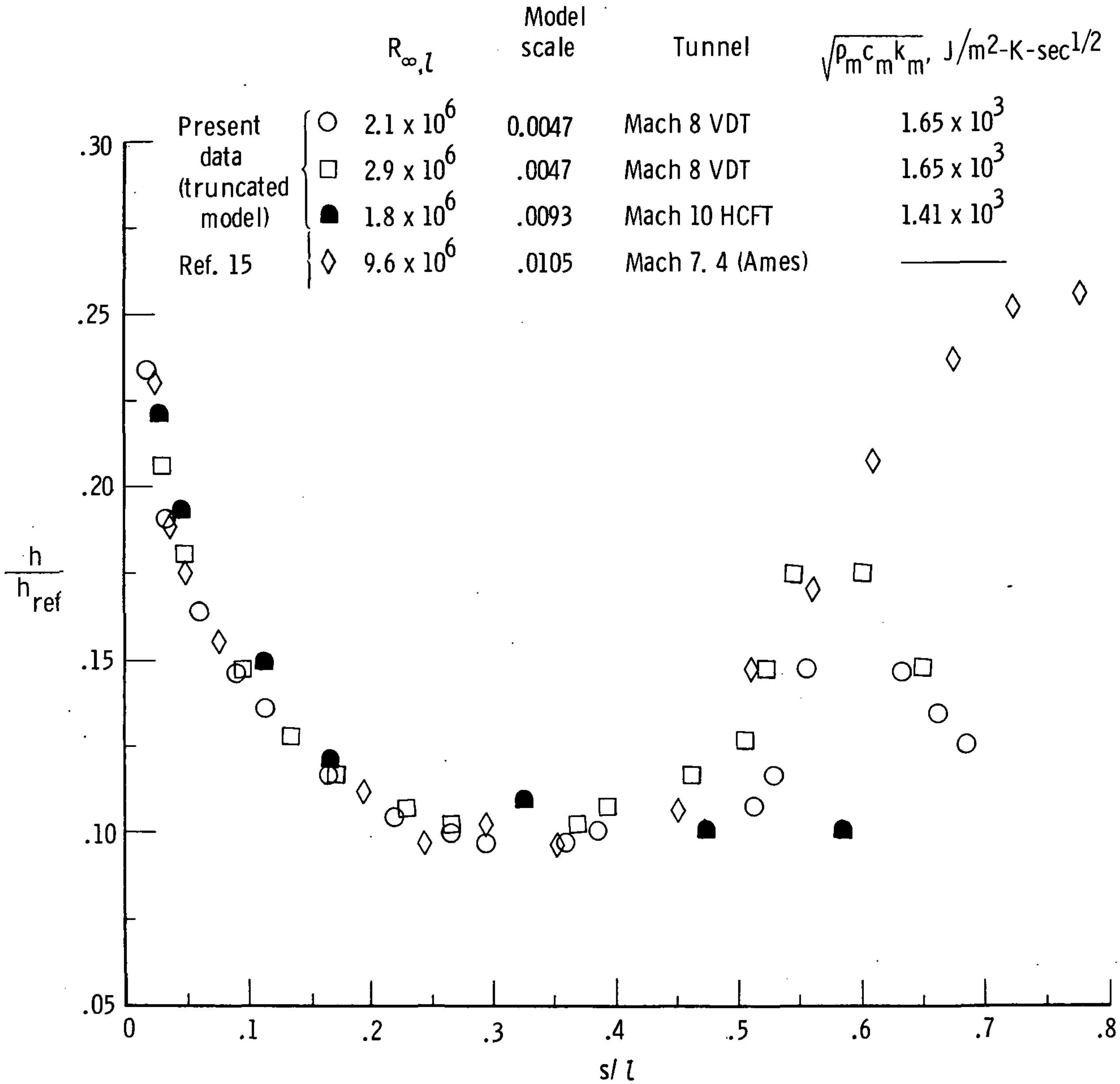

Figure 37.- Windward center-line heat-transfer-coefficient distributions at α = 60°.

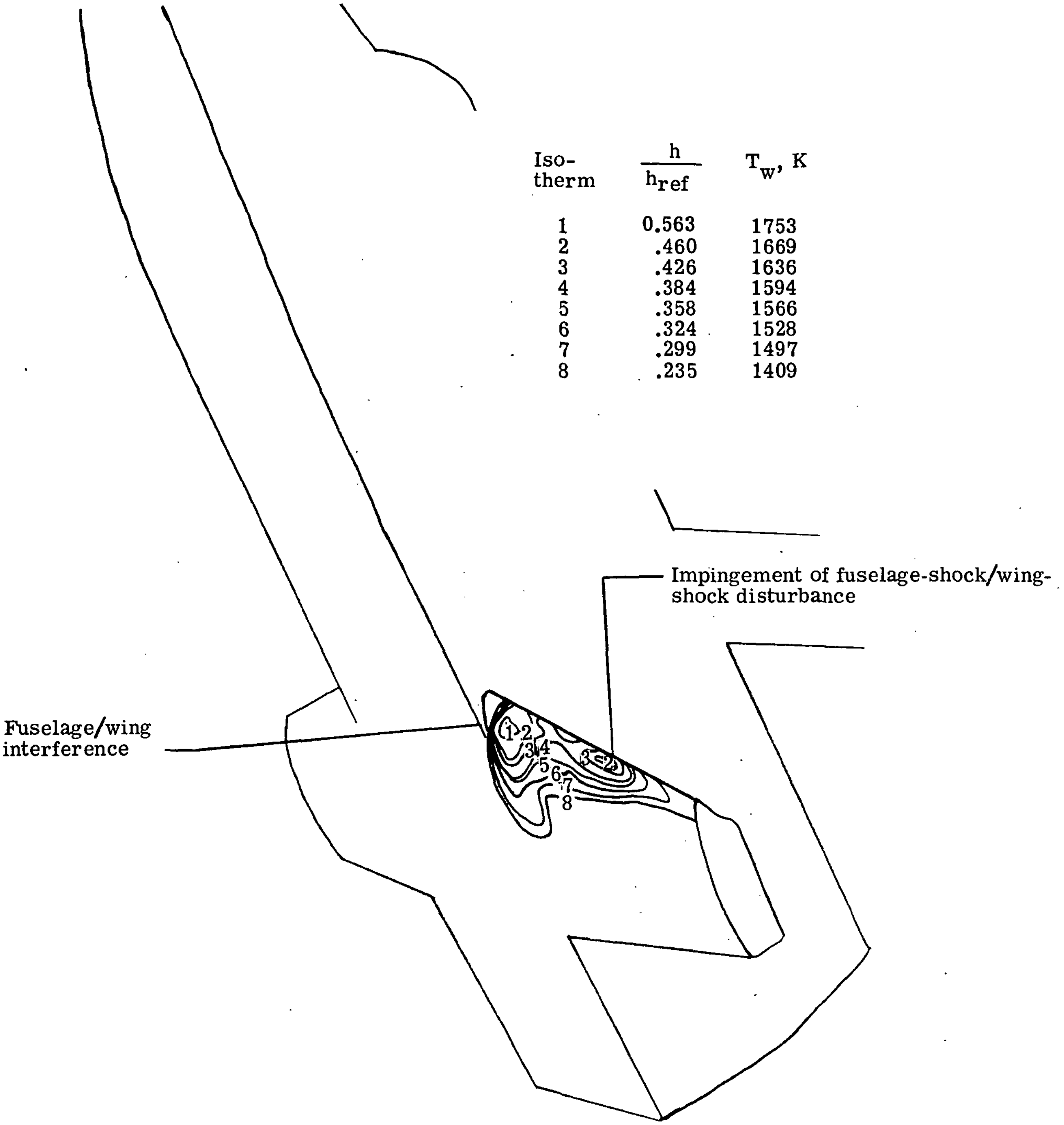

Isotherm	$\frac{h}{h_{ref}}$	T_w, K
1	0.563	1753
2	.460	1669
3	.426	1636
4	.384	1594
5	.358	1566
6	.324	1528
7	.299	1497
8	.235	1409

Figure 38.- Heat-transfer-coefficient contours on wing of 0.0047-scale model at $\alpha = 60^{\circ}$ and $M_1 \approx 8$. $R_{\infty,l} = 2.1 \times 10^6$; $h_{ref} = 1.71 \times 10^3$ W/m^2-K; $\dot{Q}_{max} = 7.71 \times 10^5$ W/m^2.

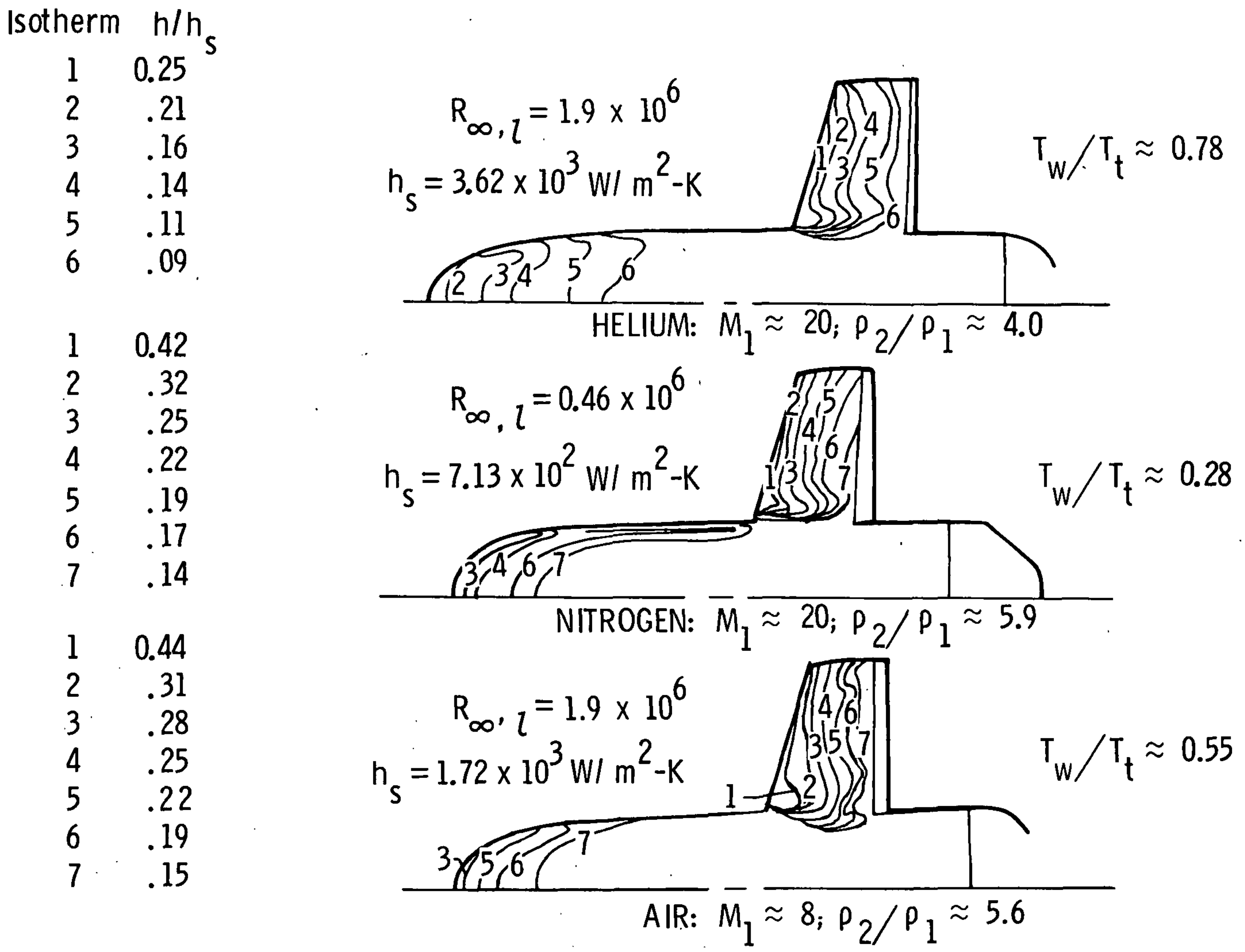

Isotherm	h/h_s
1	0.25
2	.21
3	.16
4	.14
5	.11
6	.09
1	0.42
2	.32
3	.25
4	.22
5	.19
6	.17
7	.14
1	0.44
2	.31
3	.28
4	.25
5	.22
6	.19
7	.15

Figure 39.- Heat-transfer-coefficient contours at $\alpha = 60^o$.

Iso-therm	$\frac{h}{h_{ref}}$	T_w, K
1	0.178	1343
2	.159	1308
3	.142	1270
4	.128	1236
5	.111	1193

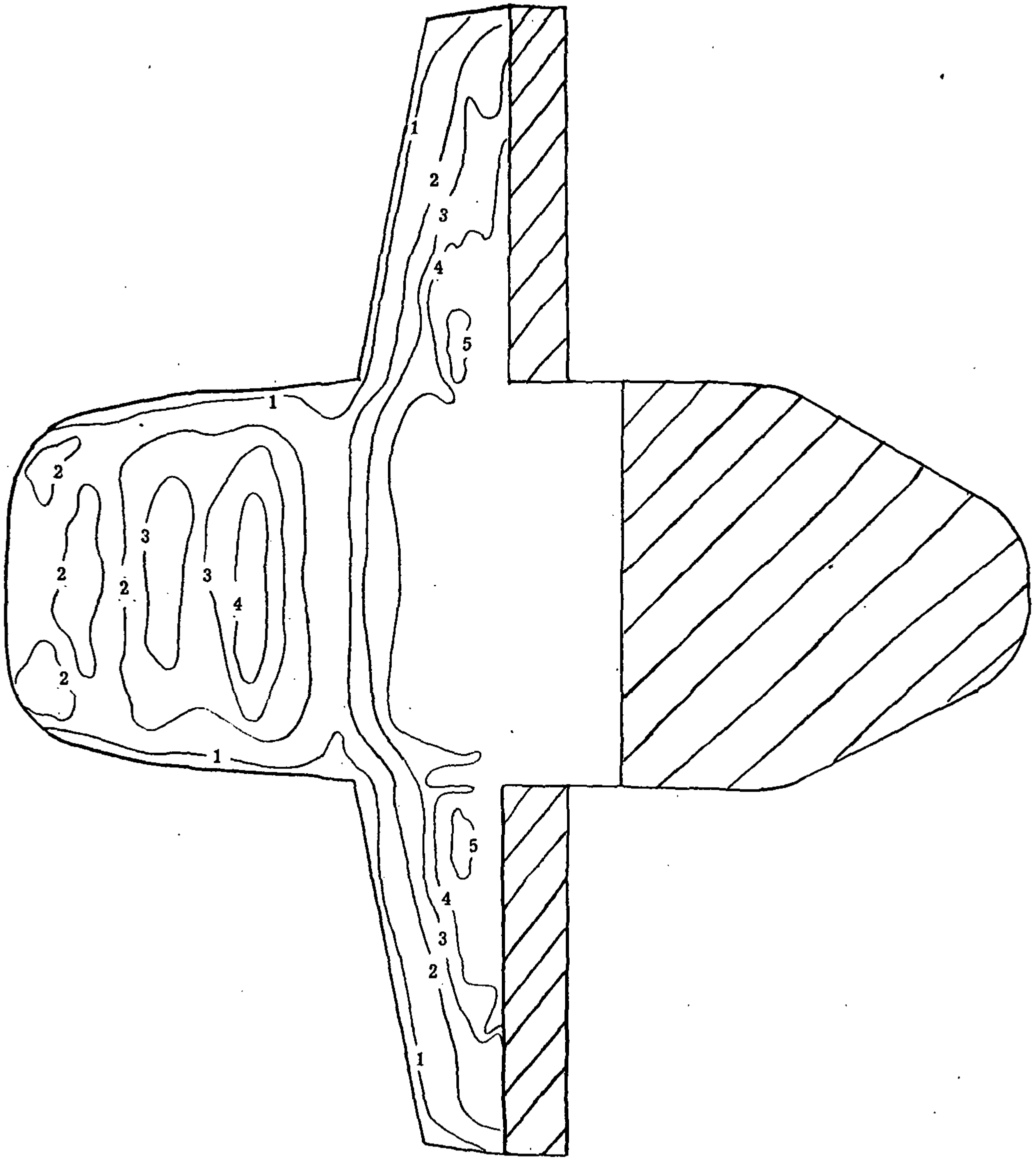

Figure 40.- Heat-transfer-coefficient and skin-temperature contours on 0.0093-scale model at $\alpha = 80^\circ$ and $M_1 = 10.3$. $R_{\infty,l} = 1.80 \times 10^6$; $h_{ref} = 7.13 \times 10^2$ W/m^2-K; $\dot{Q}_{max} = 8.39 \times 10^5$ W/m^2.

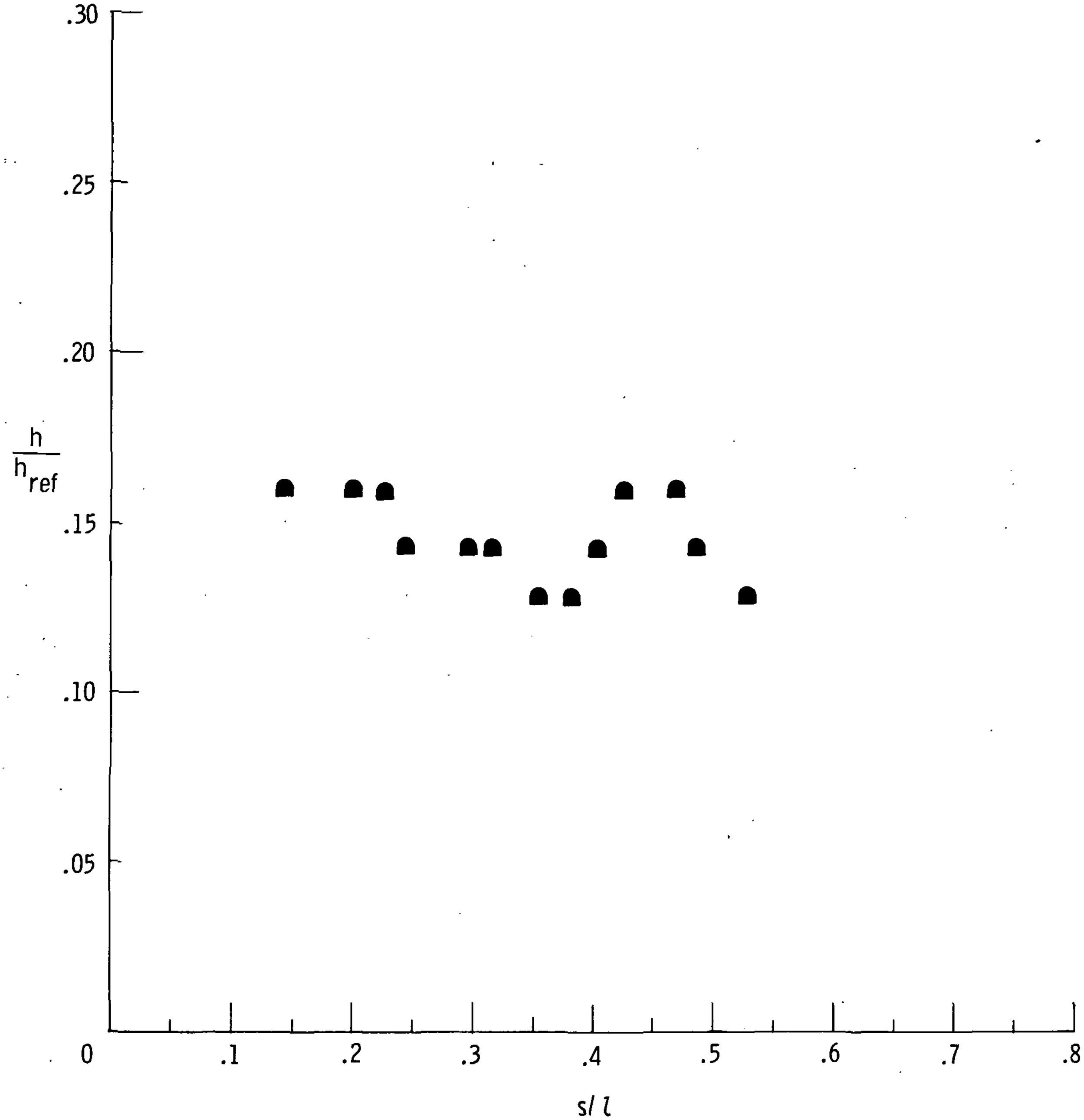

Figure 41.- Windward center-line heat-transfer-coefficient distribution on 0.0093-scale model at $\alpha = 80^{\circ}$. $M_1 = 10.3$; $R_{\infty,l} = 1.80 \times 10^6$.

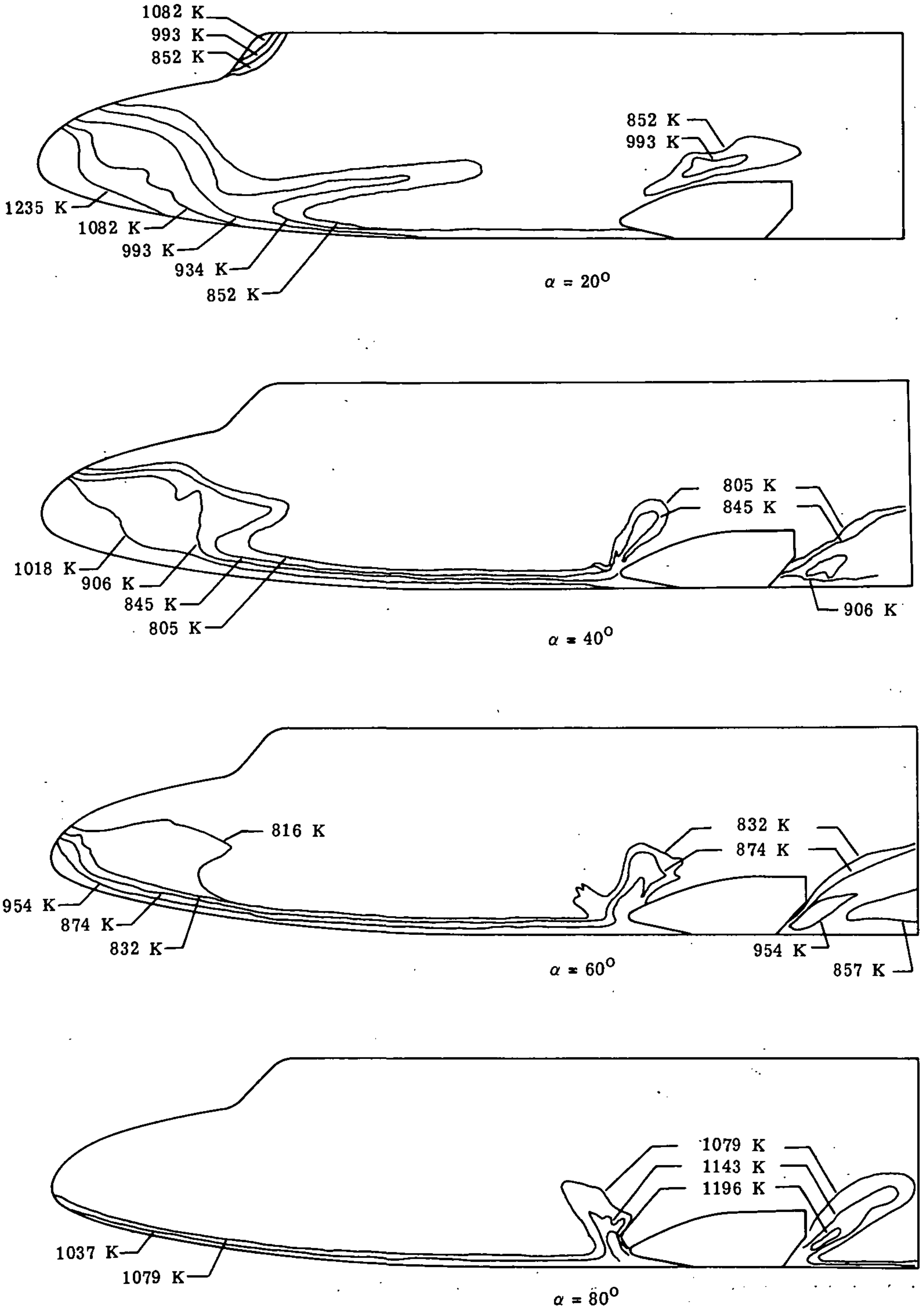

Figure 42.- Skin temperature on side panel. $M_1 = 10.3$; $R_{\infty,l} = 1.80 \times 10^6$.

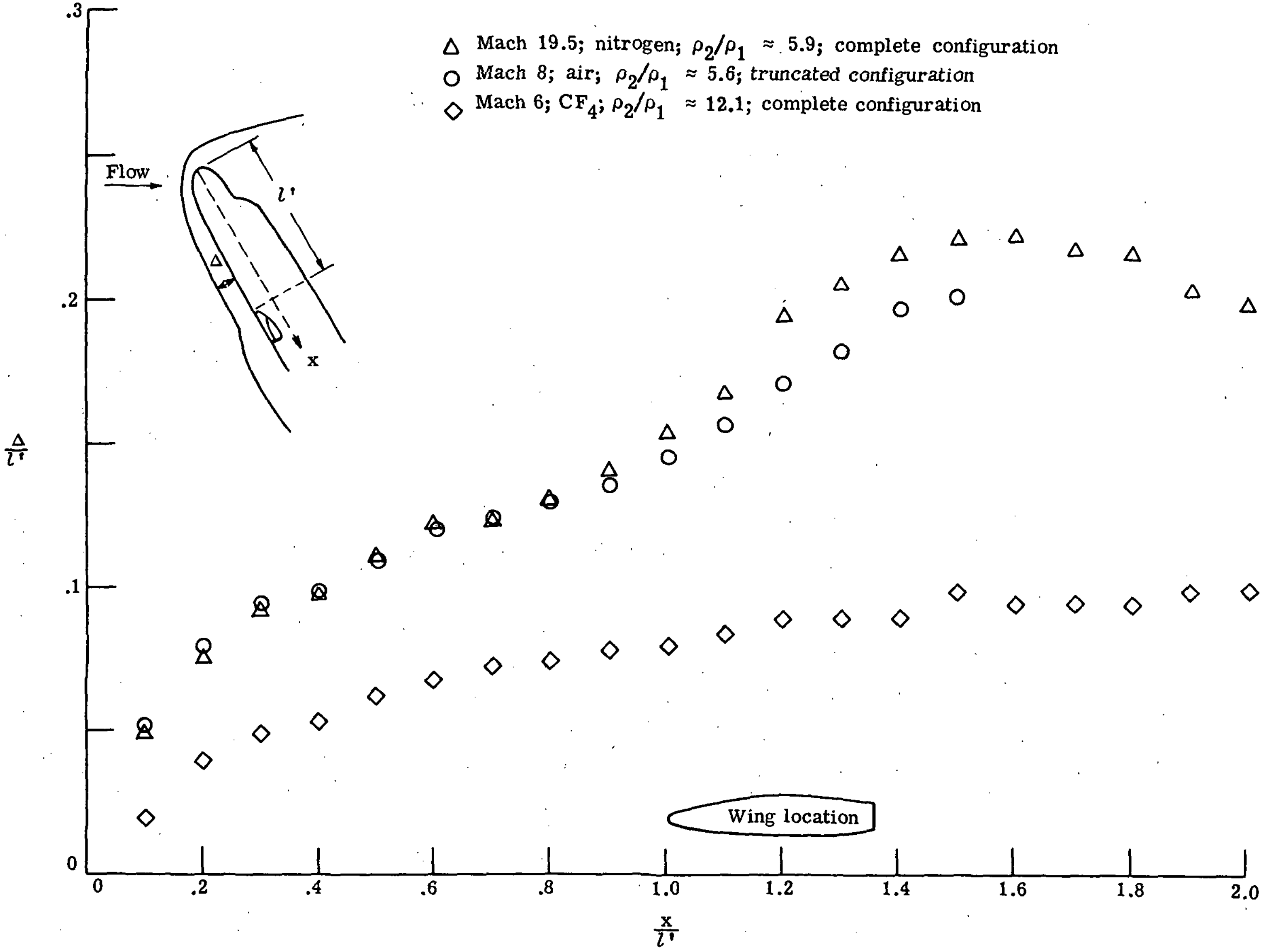

Figure 43.- Shock-standoff-distance distributions on straight-wing orbiter at $\alpha = 60^{\circ}$.

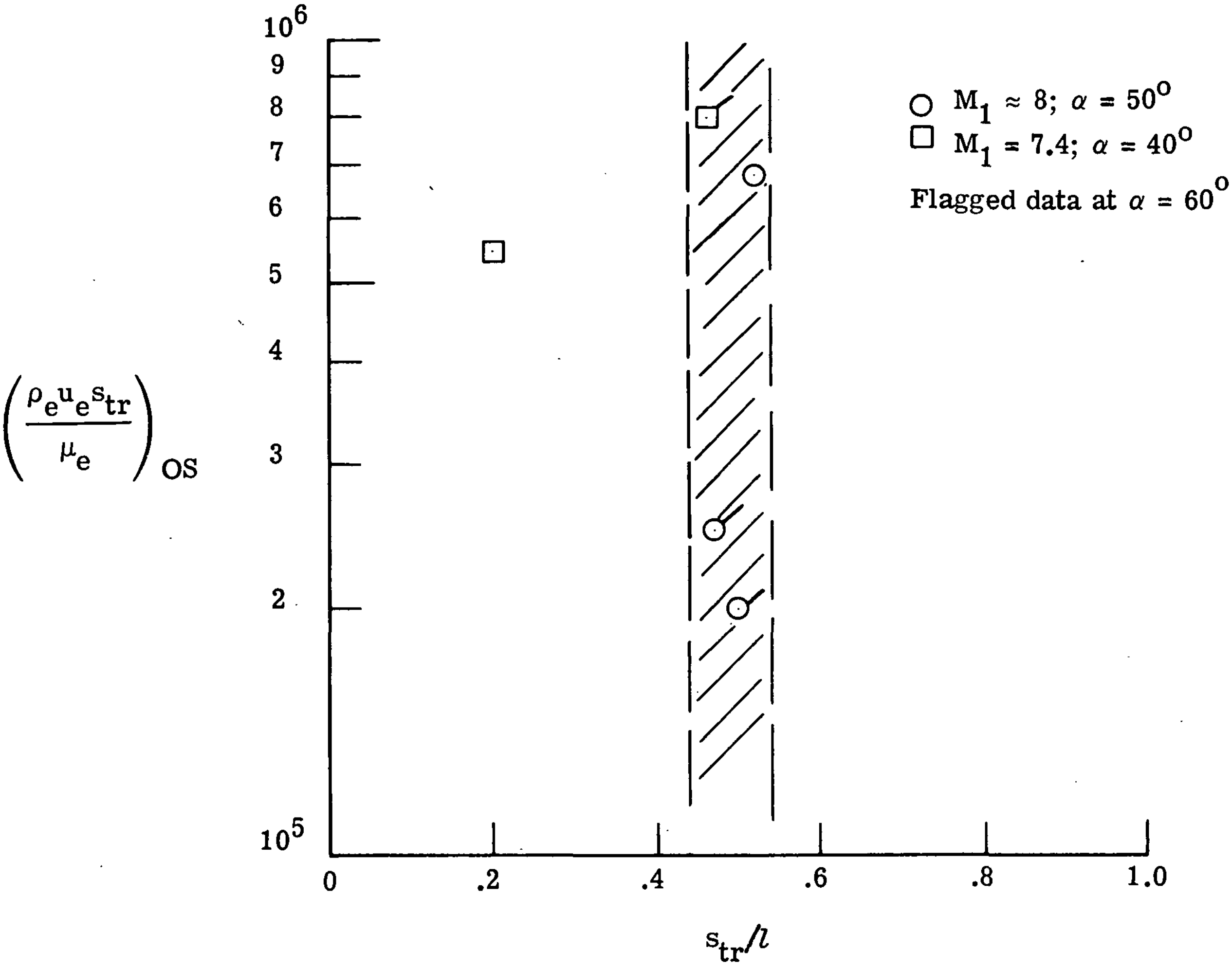

Figure 44.- Variation of transition Reynolds number with transition position.

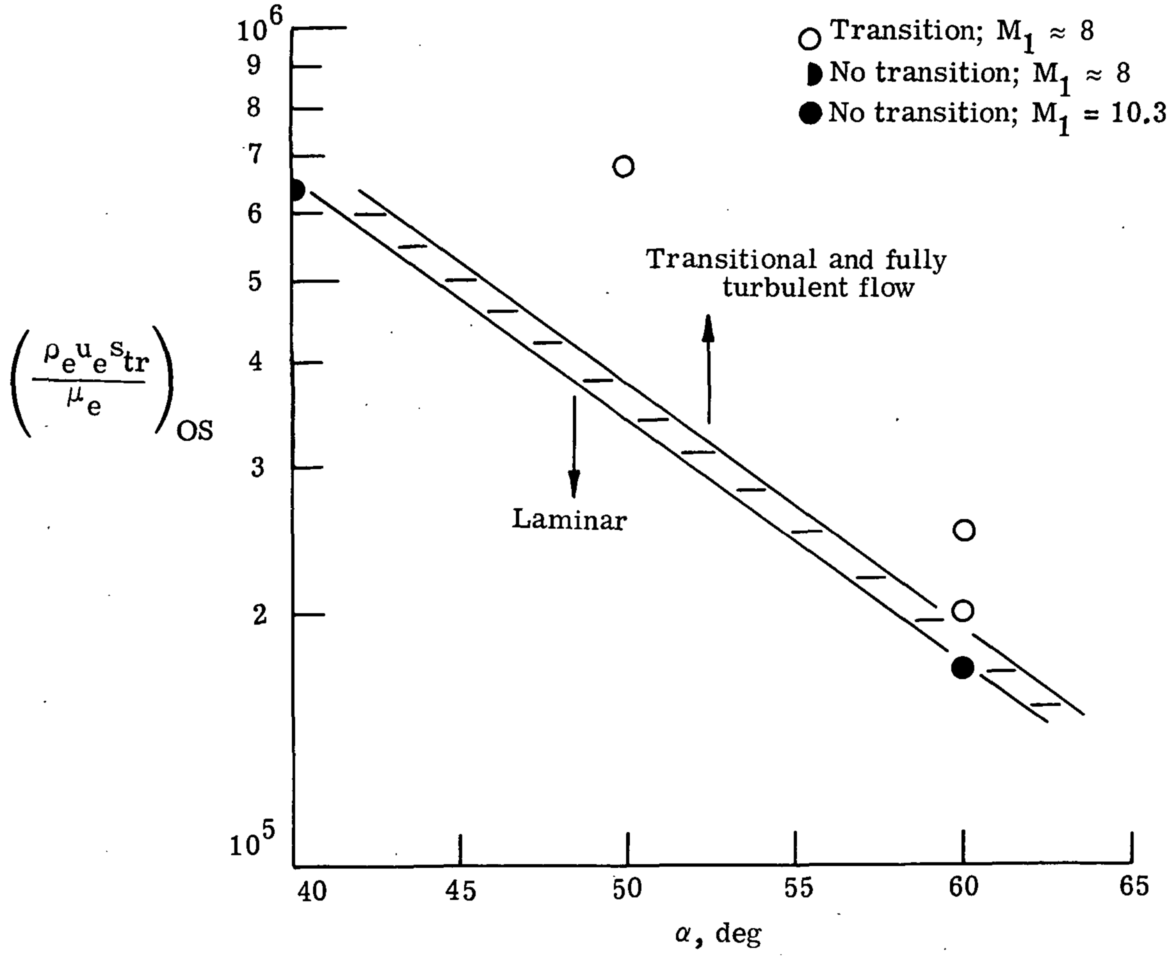

Figure 45.- Variation of transition Reynolds number with angle of attack.

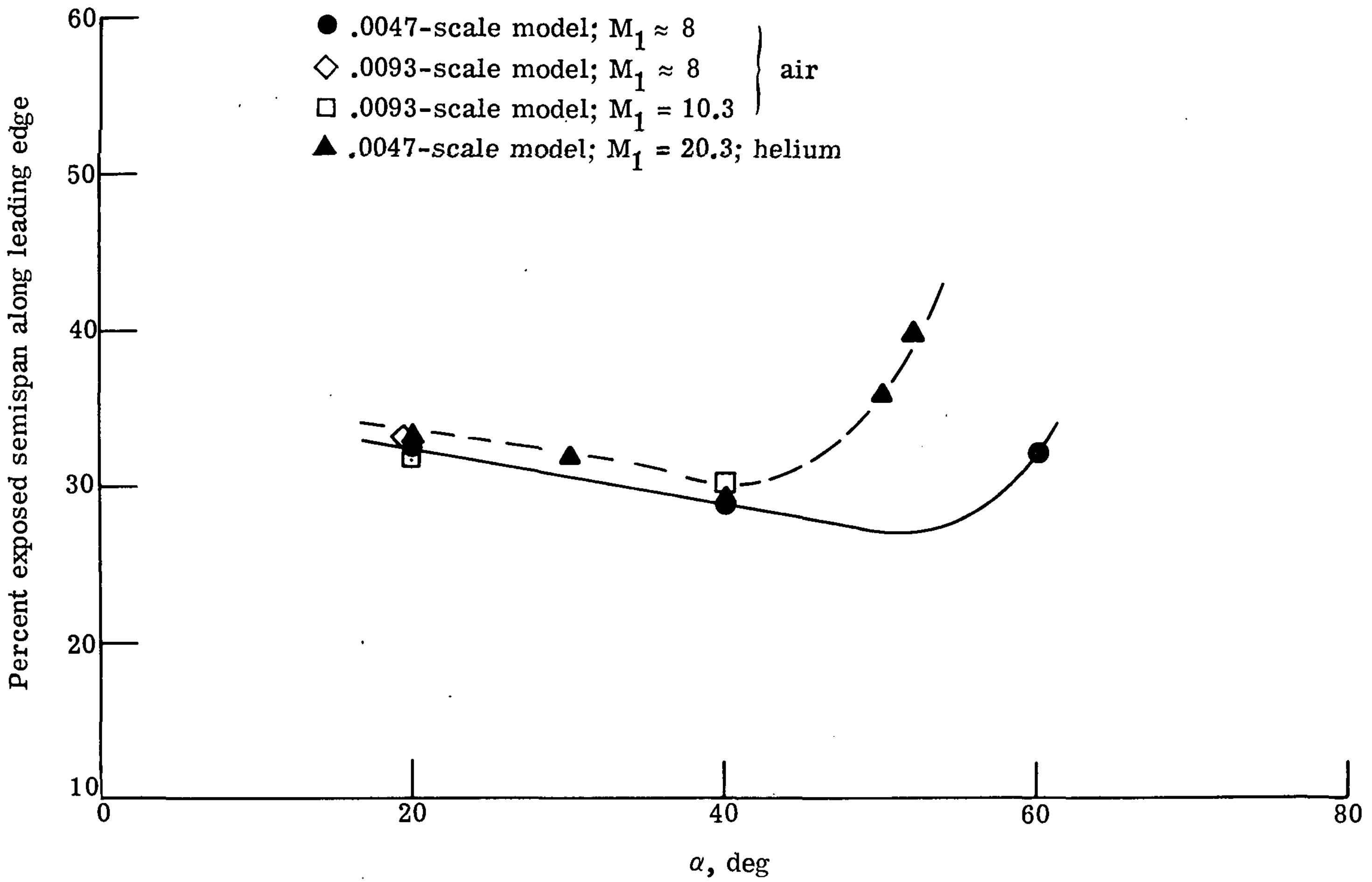

Figure 46.- Variation of impingement position of shock-interaction disturbance on wing leading edge with angle of attack.

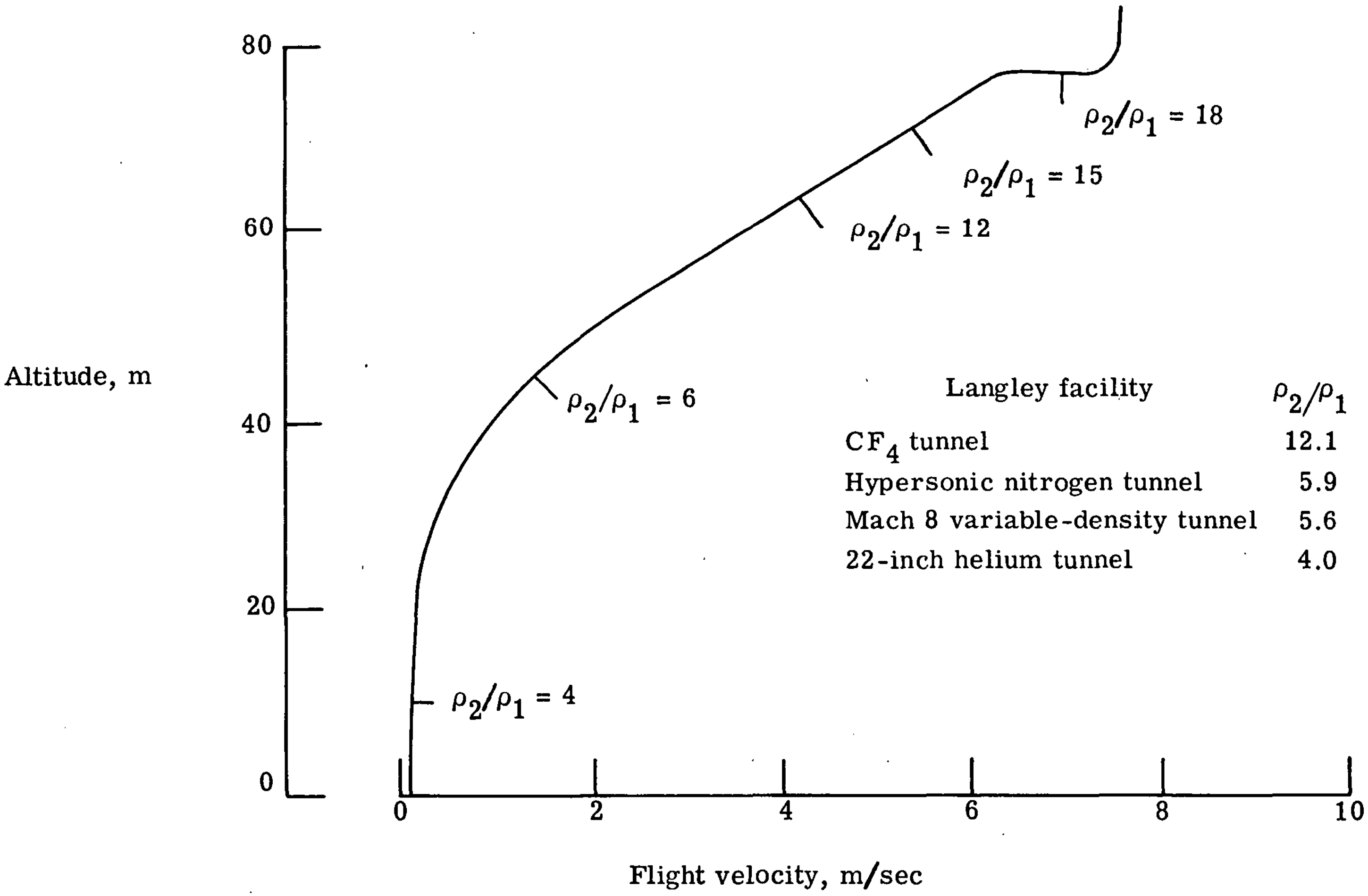

Figure 47.- Density ratio across normal shock along straight-wing-orbiter trajectory. $\alpha = 60^{\circ}$.

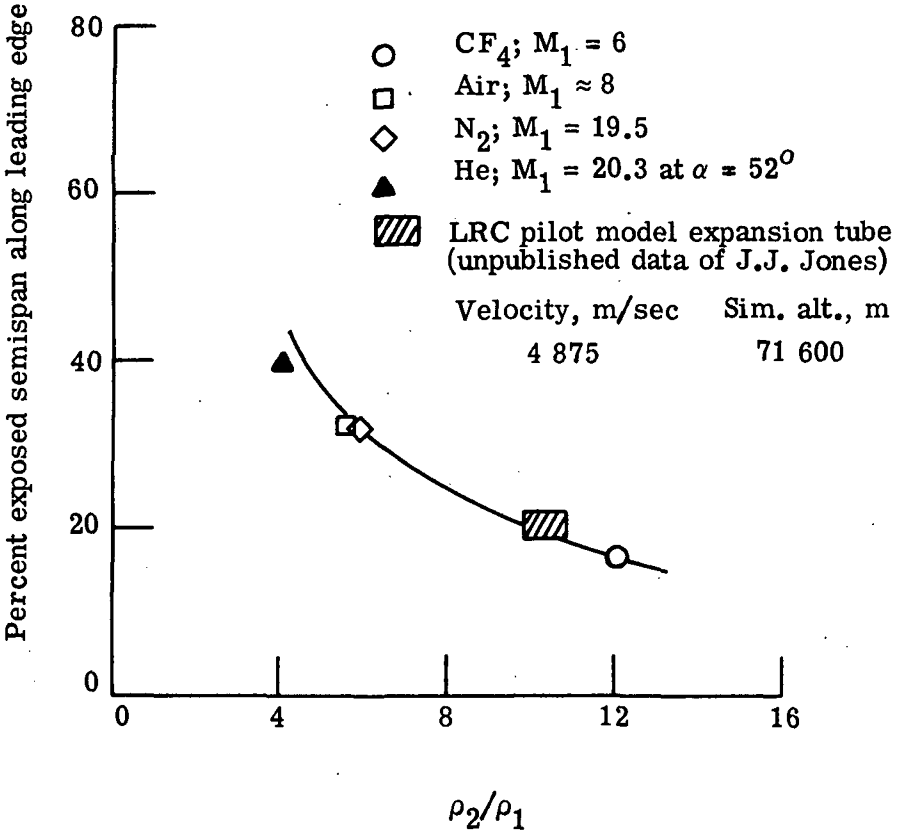

Figure 48.- Variation of shock impingement position with density ratio for straight-wing orbiter at $\alpha = 60^o$.

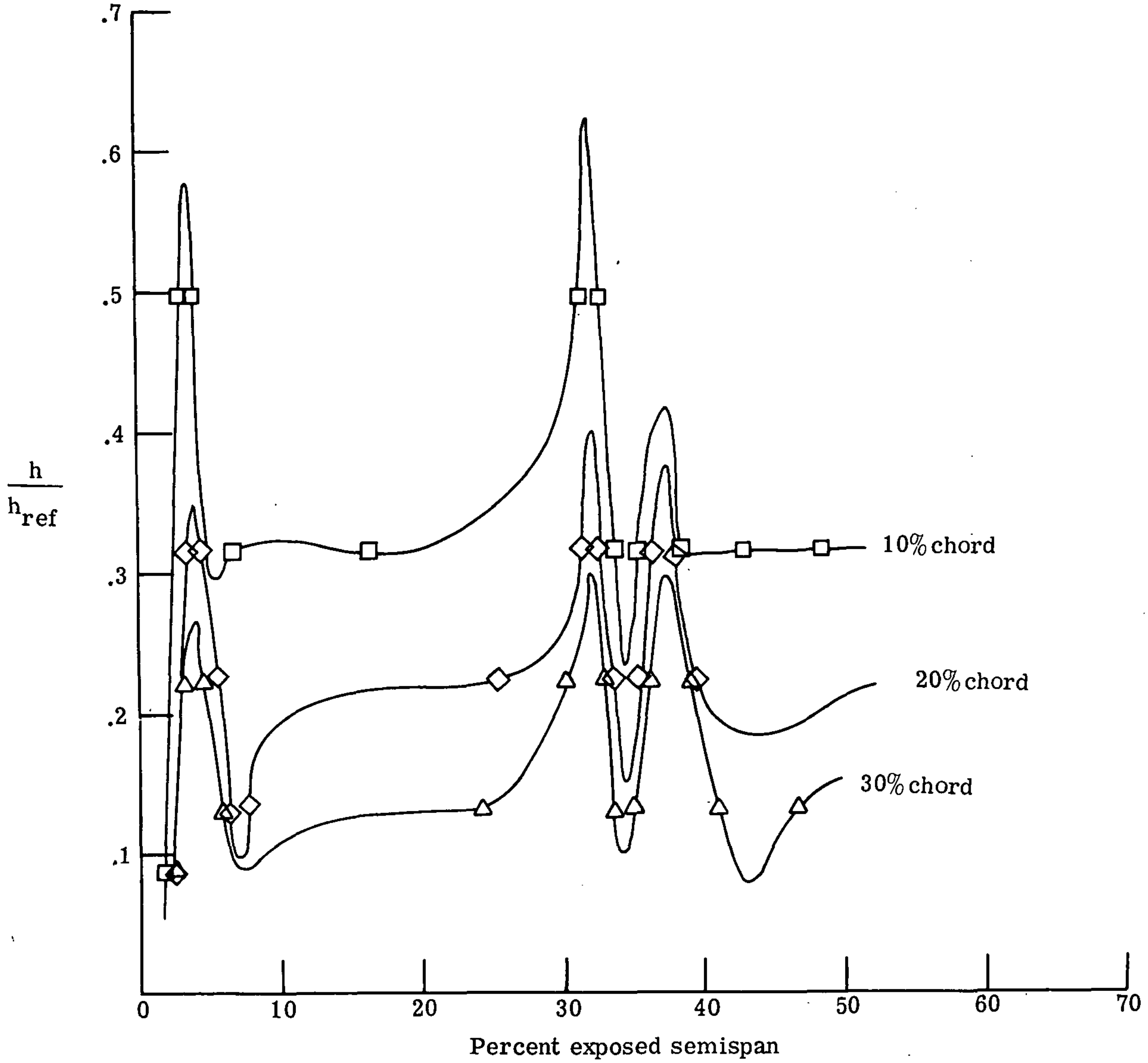

(a) $M_1 \approx 8$; 0.0093-scale model; $R_{\infty,l} = 3.39 \times 10^6$.

Figure 49.- Heat-transfer-coefficient distribution on truncated wing at $\alpha = 20^\circ$.

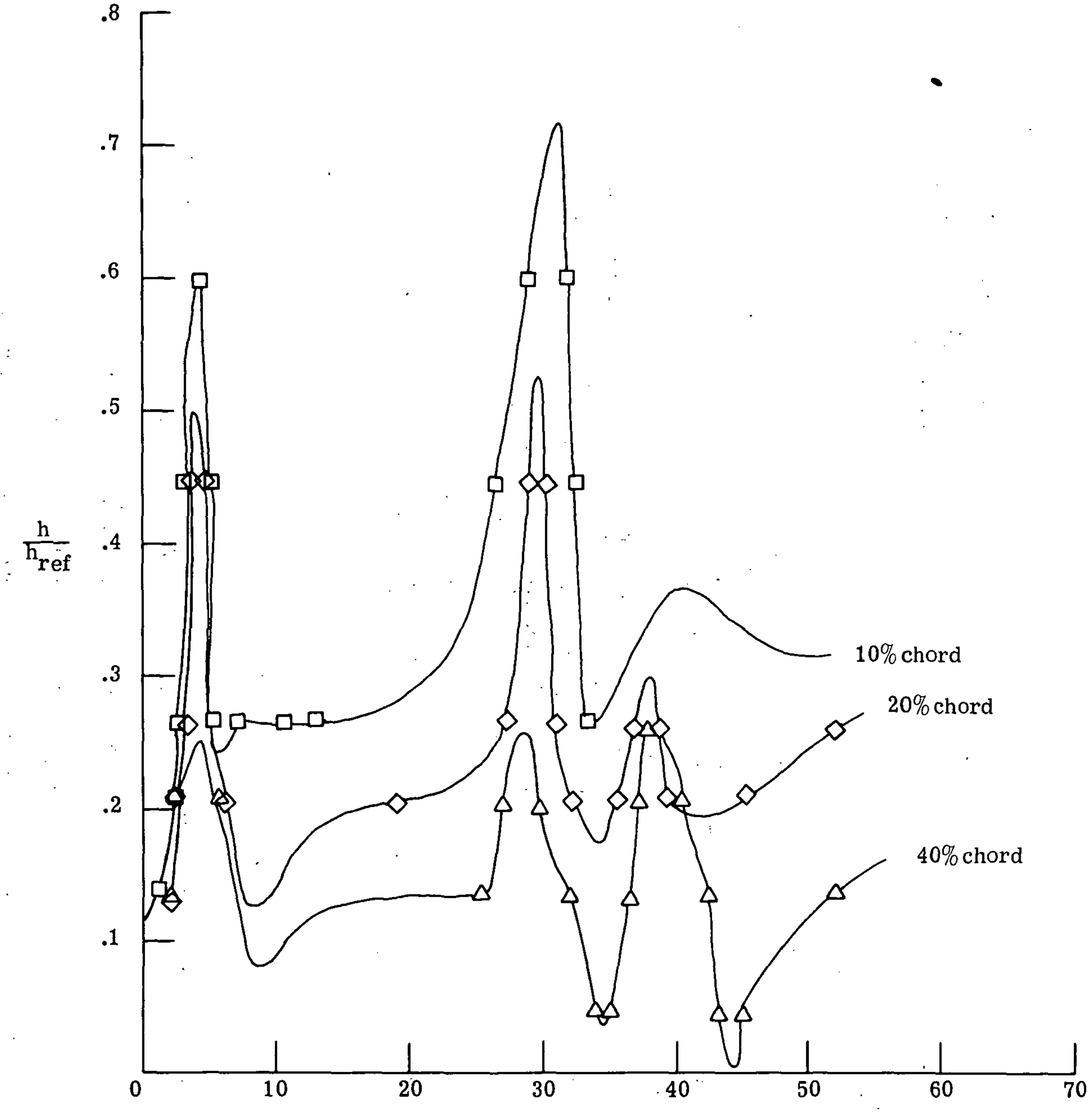

(b) $M_1 = 10.3$; 0.0093-scale model; $R_{\infty,l} = 1.80 \times 10^6$.

Figure 49.- Concluded.

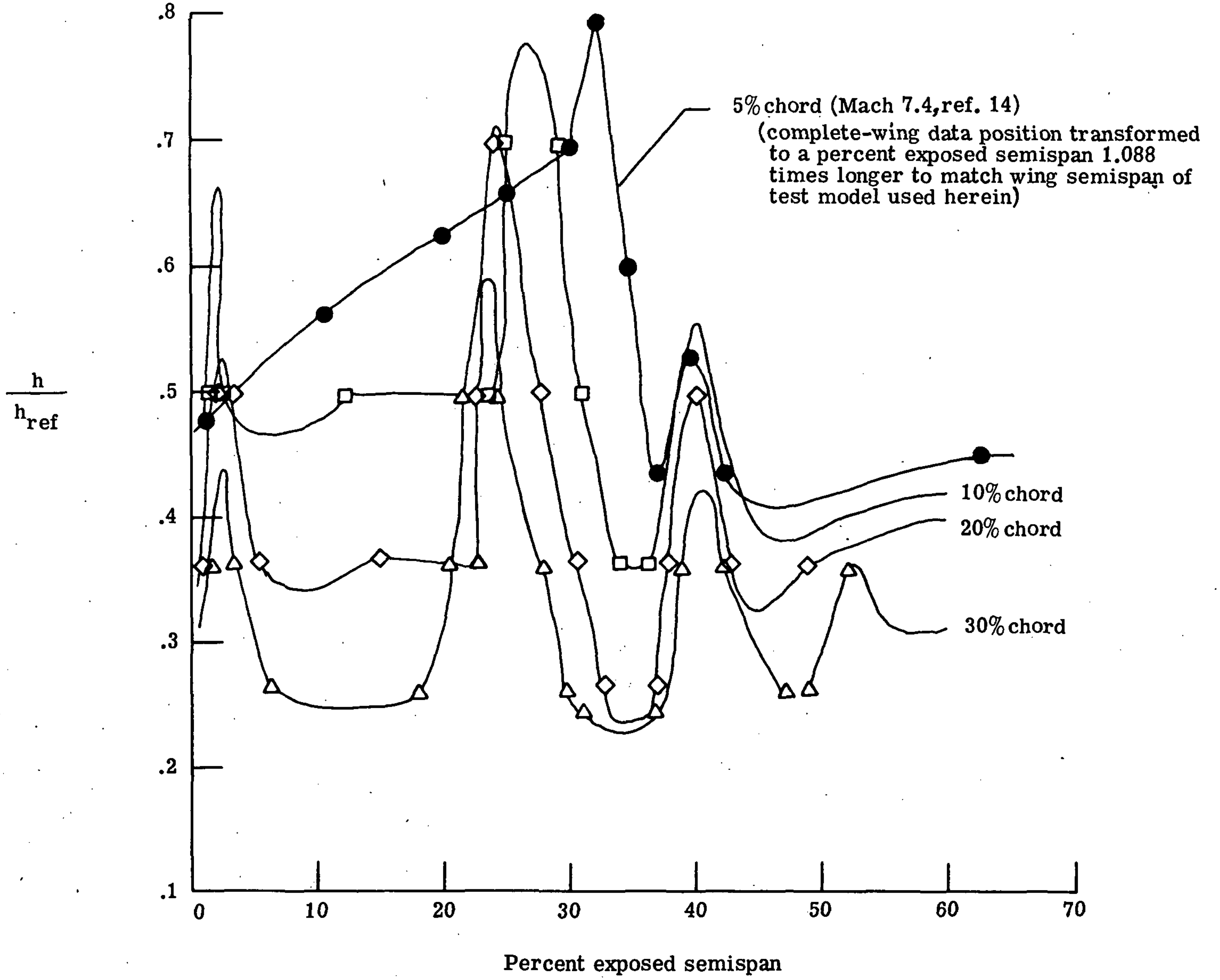

(a) $M_1 \approx 8$; 0.0047-scale model; $R_{\infty,l} = 1.99 \times 10^6$.

Figure 50.- Heat-transfer-coefficient distribution on truncated wing at $\alpha = 40^{\circ}$.

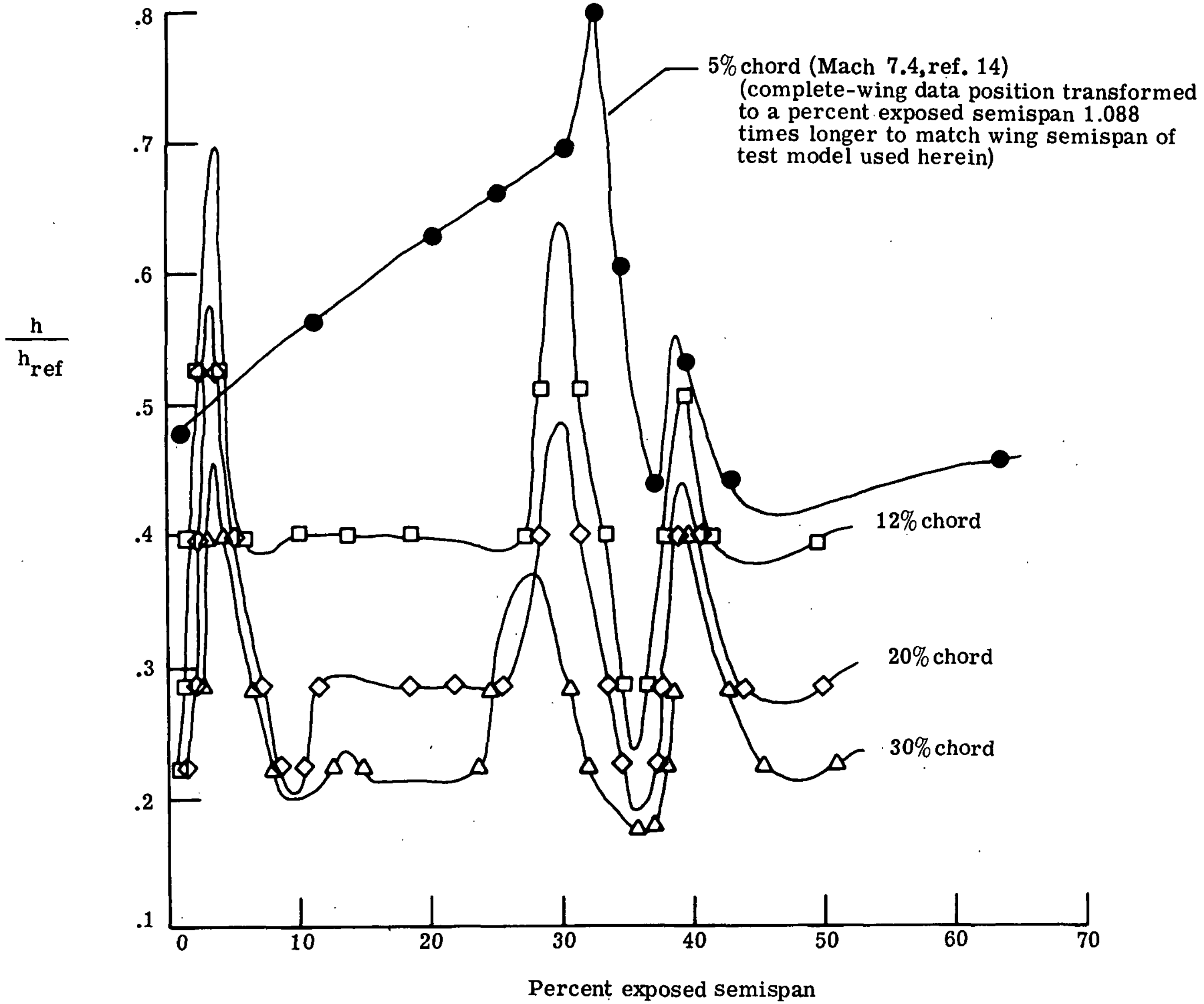

(b) $M_1 = 10.3$; 0.0093-scale model; $R_{\infty,l} = 1.80 \times 10^6$.

Figure 50.- Concluded.

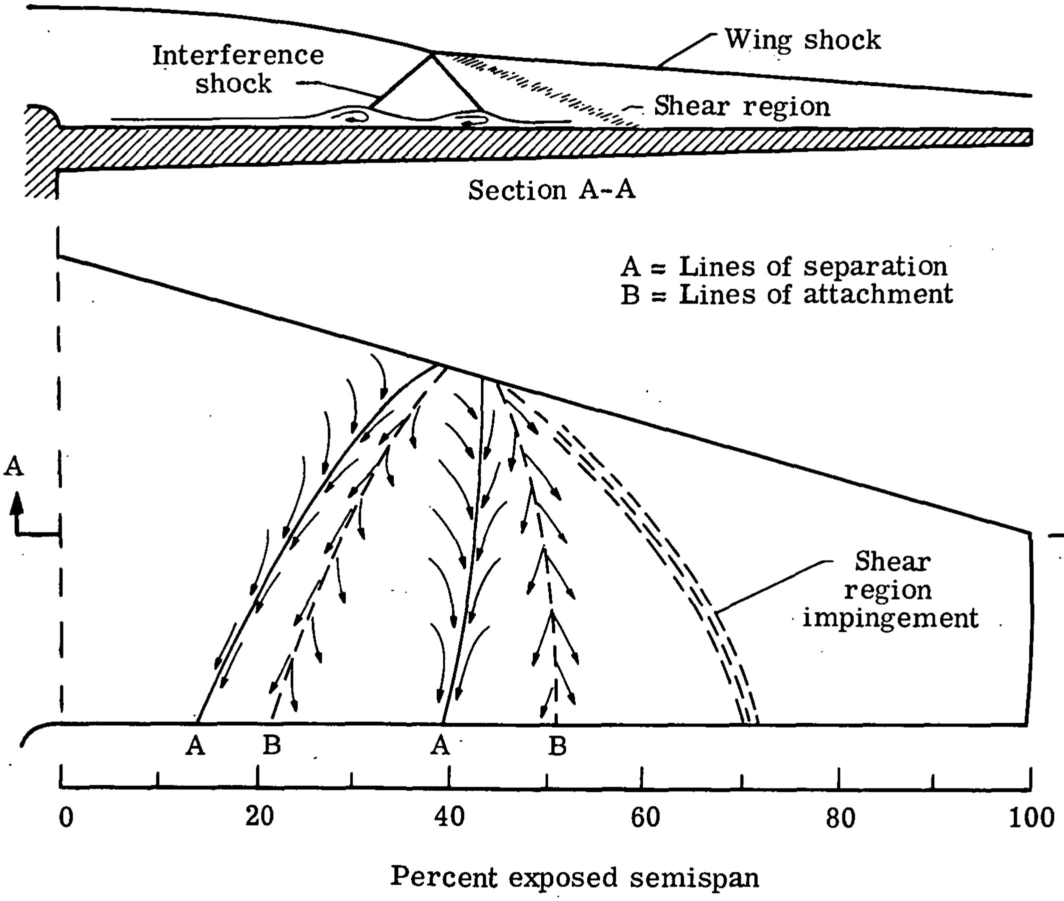

Figure 51.- Proposed flow model (ref. 14). $\alpha = 40^{\circ}$; $M_1 = 7.4$; $R_{\infty,l} = 1.0 \times 10^6$.

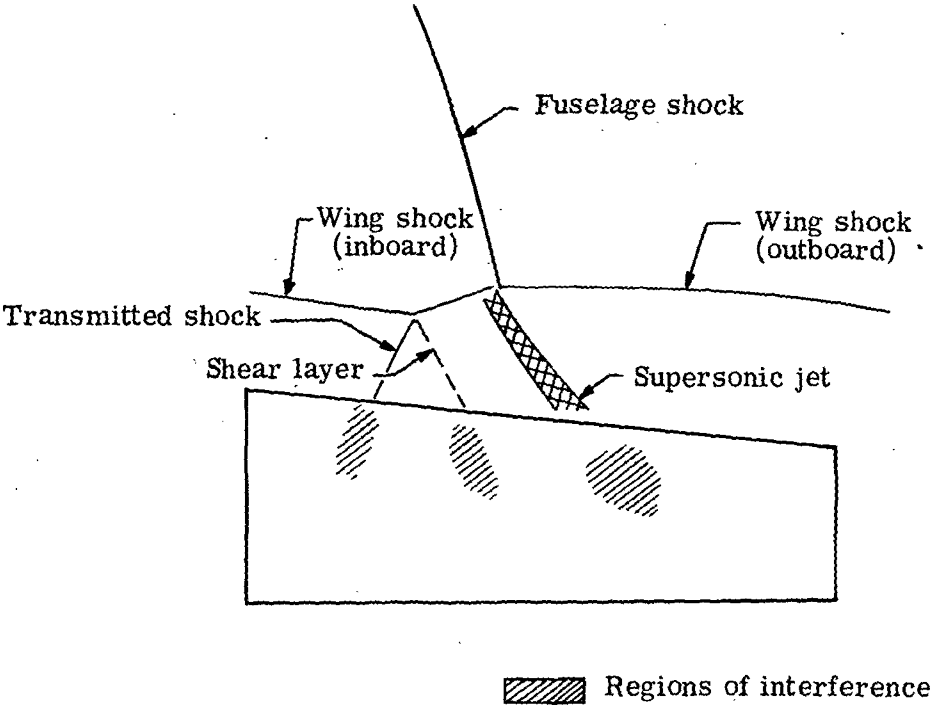

Figure 52.- Schematic of Edney's type V interaction with resulting impingement regions. (Proposed flow model, ref. 19.)

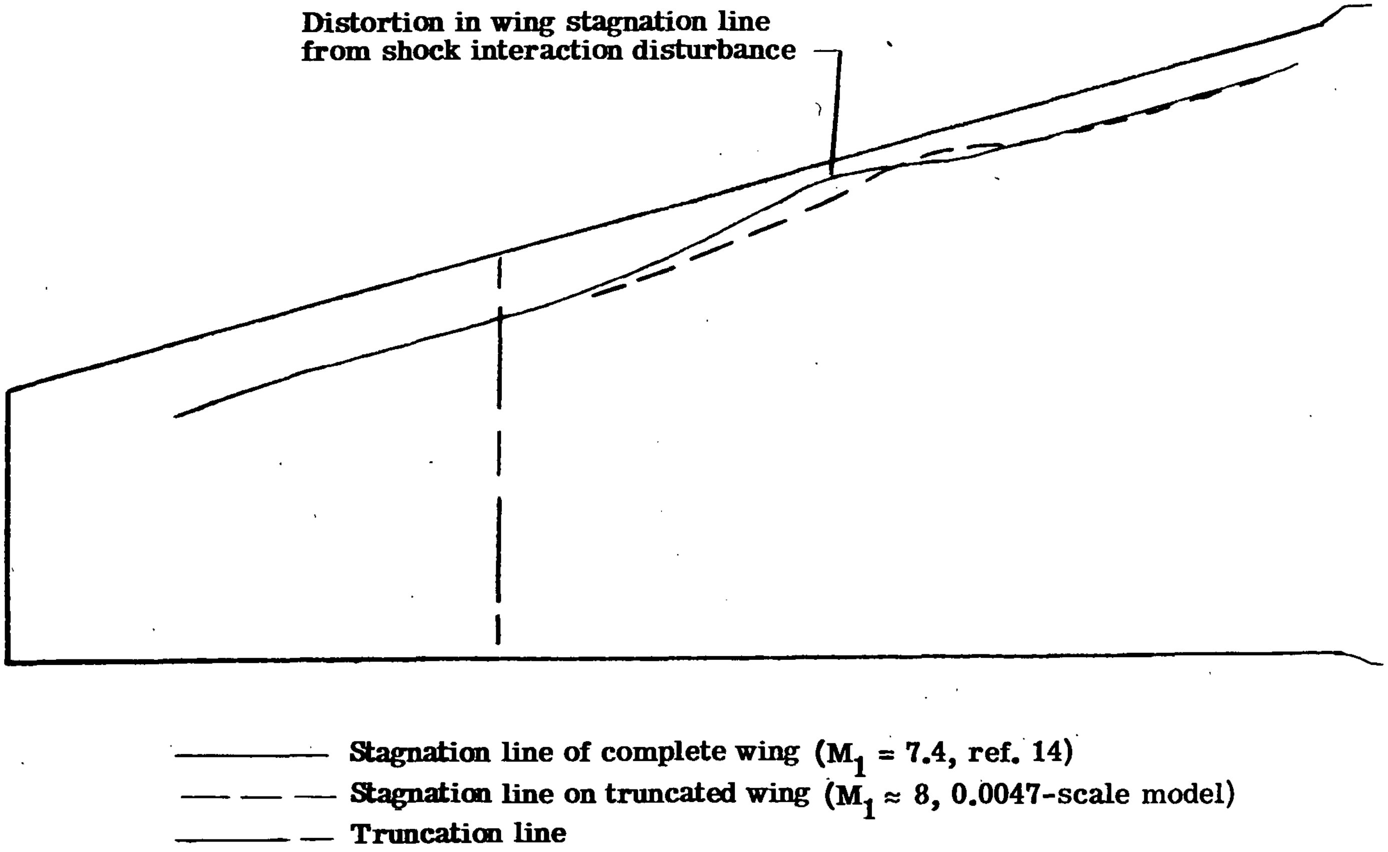

Figure 53.- Stagnation lines on complete and truncated wings at $\alpha = 60^{\circ}$.

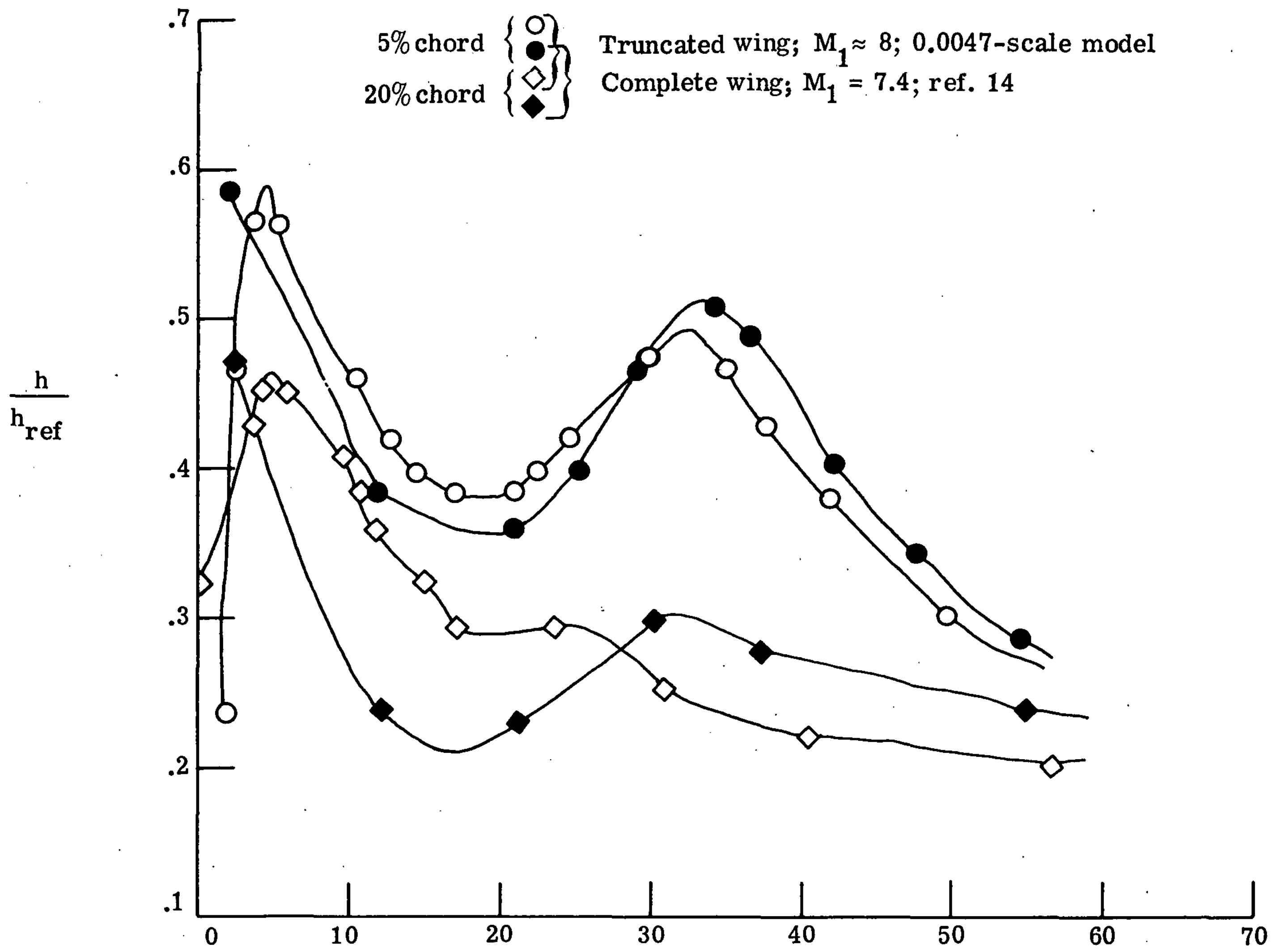

Figure 54.- Heat-transfer-coefficient distribution on wing at $\alpha = 60^{\circ}$.

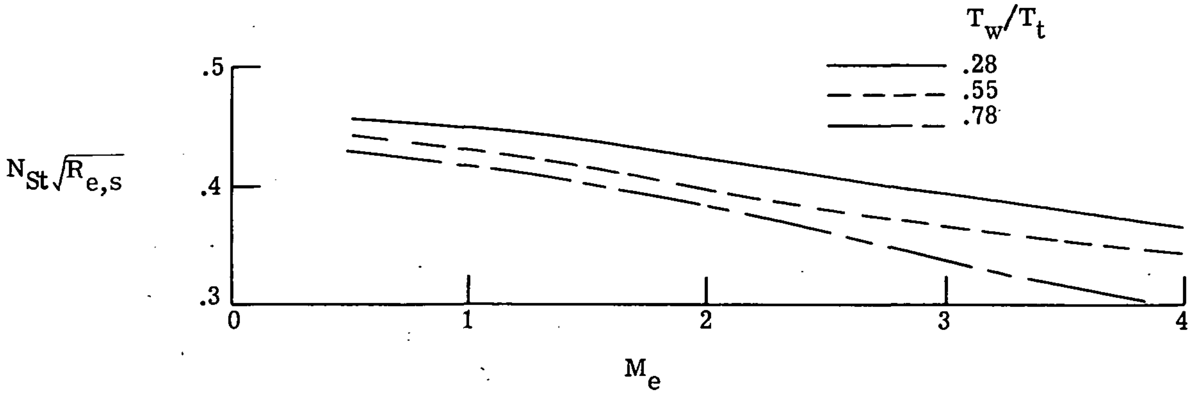

(a) Helium; T_t = 467 K.

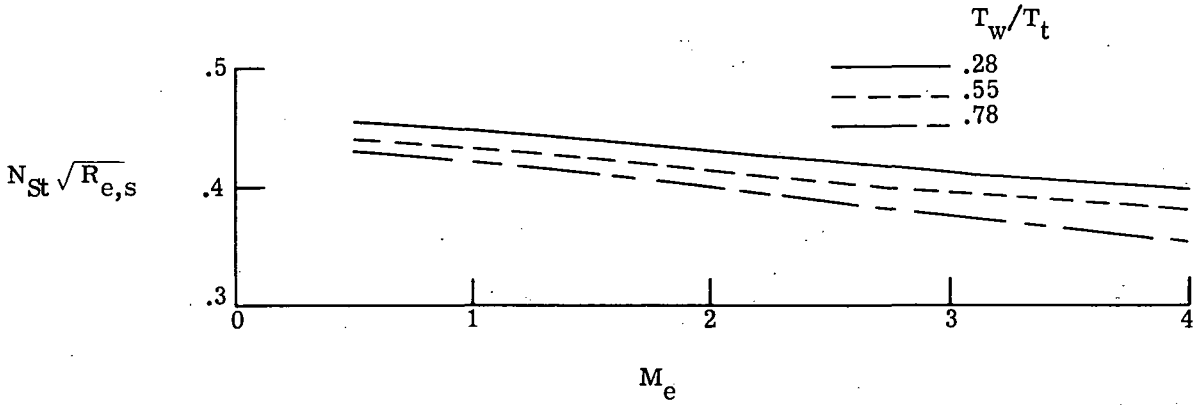

(b) Air; T_t = 810 K.

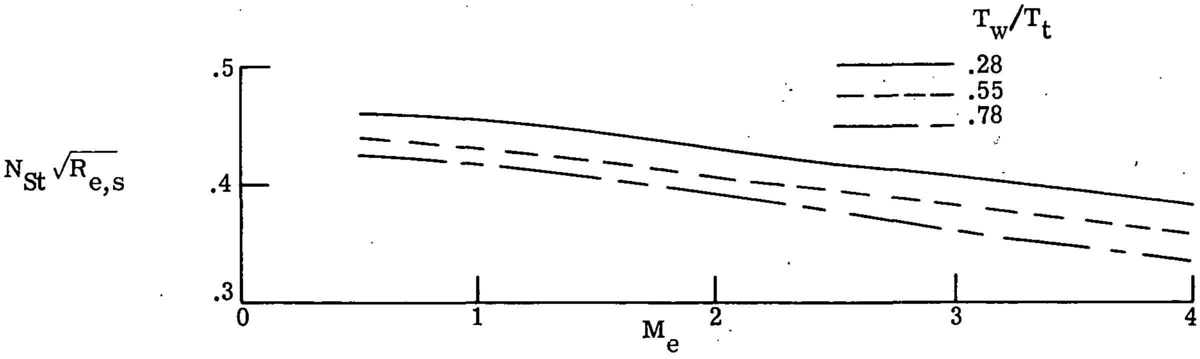

(c) Air; T_t = 1644 K (representative of nitrogen tests).

Figure 55.- Effect of wall temperature on the heat transfer to a flat plate (similar solutions).

NASA-Langley, 1973 —— 1 L-7946

NATIONAL AERONAUTICS AND SPACE ADMINISTRATION
WASHINGTON, D.C. 20546

OFFICIAL BUSINESS
PENALTY FOR PRIVATE USE $300

SPECIAL FOURTH-CLASS RATE
BOOK

POSTAGE AND FEES PAID
NATIONAL AERONAUTICS AND
SPACE ADMINISTRATION
451

U.S.MAIL

POSTMASTER: If Undeliverable (Section 158 Postal Manual) Do Not Return

> *"The aeronautical and space activities of the United States shall be conducted so as to contribute . . . to the expansion of human knowledge of phenomena in the atmosphere and space. The Administration shall provide for the widest practicable and appropriate dissemination of information concerning its activities and the results thereof."*
>
> —NATIONAL AERONAUTICS AND SPACE ACT OF 1958

NASA SCIENTIFIC AND TECHNICAL PUBLICATIONS

TECHNICAL REPORTS: Scientific and technical information considered important, complete, and a lasting contribution to existing knowledge.

TECHNICAL NOTES: Information less broad in scope but nevertheless of importance as a contribution to existing knowledge.

TECHNICAL MEMORANDUMS: Information receiving limited distribution because of preliminary data, security classification, or other reasons. Also includes conference proceedings with either limited or unlimited distribution.

CONTRACTOR REPORTS: Scientific and technical information generated under a NASA contract or grant and considered an important contribution to existing knowledge.

TECHNICAL TRANSLATIONS: Information published in a foreign language considered to merit NASA distribution in English.

SPECIAL PUBLICATIONS: Information derived from or of value to NASA activities. Publications include final reports of major projects, monographs, data compilations, handbooks, sourcebooks, and special bibliographies.

TECHNOLOGY UTILIZATION PUBLICATIONS: Information on technology used by NASA that may be of particular interest in commercial and other non-aerospace applications. Publications include Tech Briefs, Technology Utilization Reports and Technology Surveys.

Details on the availability of these publications may be obtained from:

SCIENTIFIC AND TECHNICAL INFORMATION OFFICE
NATIONAL AERONAUTICS AND SPACE ADMINISTRATION
Washington, D.C. 20546